# STOCHASTIC MODEL FOR SURFACE DIFFUSION OF ORGANIC MOLECULES

by

Patrick Shea

Submitted in partial fulfillment of the
requirements for the degree of
Doctor of Philosophy

at

Dalhousie University
Halifax, Nova Scotia
March 2015

# Table of Contents

# List of Tables

# List of Figures

# Abstract

A theoretical model for the diffusion of large molecules adsorbed on surfaces is developed. Starting from the classical equations of motion, a generalized non-Markovian Langevin equation for the center of mass diffusive motion of an adsorbed molecule is derived. In this model, the influence of the background on the molecule is separated into an adiabatic force, and a rapidly fluctuating stochastic force with a corresponding frictional damping term. The model accounts for energy exchange between the center of mass motion and vibrational degrees of freedom of the molecule, and expressions for the friction coefficient in terms of vibrational properties of the molecule and substrate are derived.

This stochastic model is first applied to a harmonically bound dimer diffusing in one dimension. This simple model system allows for a systematic test of how the diffusive motion of a molecule is affected by its vibrational degrees of freedom, and specifically how important memory effects are in determining the diffusion coefficient. It is found that coupling to molecular vibrations leads to increased frictional damping and slower diffusion, and that memory effects are typically not important for small molecules, but could be significant in large molecules.

The model is then used to study the diffusion of dithioanthracene on a Cu(111) surface. Density functional theory is employed to calculate the adiabatic force and vibrational properties, allowing for a first principles determination of all required quantities in the stochastic model. The diffusion coefficient is calculated and compared to scanning tunnelling microscopy measurements. Reasonable agreement with experiment is obtained, and it is seen that the stochastic model gives an estimate of the diffusion prefactor much closer to the measured value compared to standard transition state theory.

# List of Abbreviations and Symbols Used

| | |
|---|---|
| $a$ | surface lattice constant |
| $C_{ij,kl}$ | expansion coefficients for probability density |
| $D_c$ | collective diffusion coefficient |
| DFT | density functional theory |
| $D_t$ | tracer diffusion coefficient |
| DTA | dithioanthracene |
| $\Delta V$ | diffusion energy barrier |
| $\vec{f}$ | fluctuating stochastic force |
| $\vec{F}$ | average force |
| FIM | field ion microscope |
| FPE | Fokker-Planck equation |
| $\phi$ | derivative of potential $(\partial V/\partial s)\|_{s=s_0}$ |
| $\gamma$ | friction coefficient |
| $\Gamma$ | memory function |
| GGA | generalized gradient approximation |
| GLE | generalized Langevin equation |
| HA | harmonic approximation |
| $\eta$ | reduced friction coefficient $\gamma_{ss}/\mu$ |
| $k$ | Boltzmann constant |
| $\kappa$ | diffusion jump rate |
| $L$ | Fokker-Planck operator |
| $L_{ij,kl}$ | matrix elements of Fokker-Planck operator |
| $\ell$ | equilibrium dimer length |
| $m$ | mass of adsorbed atom |
| $m_s$ | mass of substrate atom |
| $M$ | total mass of adsorbed molecule |
| $\mu$ | reduced mass of dimer |
| MA | Markov approximation |

| | |
|---|---|
| MD | molecular dynamics |
| $\rho$ | probability density |
| PBE | Perdew-Burke-Erhzhof functional |
| $q_k$ | normal mode vibration coordinates |
| $\vec{r}$ | position of adsorbed atom |
| $r$ | center of mass coordinate of dimer |
| $s$ | relative coordinate of dimer |
| $s_R$ | empirical scaling parameter for cutoff radii |
| STM | scanning tunnelling microscope |
| $t$ | time |
| $T$ | temperature |
| TPyP | tetra-pyridal porphyrin |
| TST | transition state theory |
| $\vec{u}_i$ | displacement of surface atoms |
| $v$ | velocity |
| $V$ | potential energy of adsorbed atoms |
| $V_a$ | adiabatic potential |
| vdW | van der Waals |
| $\omega$ | molecular vibration frequency |
| $\omega_D$ | Debye frequency |
| $\Omega$ | effective frequency of damped oscillator |
| $x$ | center of mass of adsorbed molecule |
| $Z_{\text{vib}}$ | vibrational partition function |

# Chapter 1

# Introduction

The thermal migration of atoms and molecules adsorbed at surfaces is an essential process in any kind of surface reaction, such as crystal growth, desorption, and catalysis. The direct experimental observation of the diffusion of individual atoms across surfaces was first made possible by the invention of the field ion microscope (FIM) in the 1950s [1]. The FIM allowed surface diffusion of metal atoms on metal surfaces to be viewed in real time, and with atomic resolution. Since these early studies, the development of the scanning tunnelling microscope (STM) has vastly extended the range of systems for which surface diffusion can be observed. In particular, STM experiments have provided powerful insights into the behaviour of organic molecules adsorbed on metal surfaces in recent years. These systems are of interest for many potential commercial applications, such as solar cells, organic light-emitting diodes, and molecular electronics [2].

The STM can produce images of metal surfaces with atomic resolution, allowing for a determination of molecular orientation with respect to the surface, and even revealing conformational changes of molecules upon adsorption [3]. Such high resolution images have revealed a variety of interesting behaviour in organic molecules on metal surfaces, such as the formation supramolecular structures coordinated by metal adatoms [4]. By taking a series of STM images and putting them together into an "STM movie", the diffusion of individual adsorbed molecules can be tracked on clean surfaces over length scales of nanometers. Several unique phenomena related to the surface diffusion of organic molecules have been revealed in this way, including unidirectional migration of molecules along their molecular axis [5,6], and a so called "lock and key" effect, where a diffusing molecule is immobilized by changing its orientation on the surface via manipulation with the STM tip [7]. These complex and varied phenomena originate from a sensitive interplay between the molecular structure and surface geometry. The aim of this thesis is to develop a consistent theoretical framework for the study of diffusion in these systems from first principles.

## 1.1 Surface Diffusion Theory

At a coarse-grained level, surface diffusion can be seen as a series of jumps between stable adsorption sites on the surface. For a clean crystalline surface, such as those typically employed in STM experiments, these sites will be arranged in a periodic lattice. If the energy barrier $\Delta V$ between sites is large compared to the thermal energy, $\Delta V \gg kT$, the jumps will be separated by long periods of oscillatory motion at the stable sites. In this case, the migration of adsorbed molecules in characterized by a jump rate $\kappa$ that has the Arrhenius form [8],

$$\kappa = \kappa_0 e^{-\Delta V/kT}, \tag{1.1}$$

where the prefactor $\kappa_0$ is roughly temperature independent.

Surface diffusion at finite coverage can then be described by a lattice gas model [8–10], in which the surface is represented by a lattice of sites that can be occupied by an adsorbate. The microstate of the system is then described by a vector of occupancies $\vec{n}$, 0 or 1 for each site. The probability $P(\vec{n}, t)$ then obeys the following master equation

$$\frac{dP(\vec{n}, t)}{dt} = \sum_{\vec{n}'} [P(\vec{n}', t)W(\vec{n}' \to \vec{n}) - P(\vec{n}, t)W(\vec{n} \to \vec{n}')], \tag{1.2}$$

where $W(\vec{n} \to \vec{n}')$ is the transition rate from state $\vec{n}$ to $\vec{n}'$. These transition rates are determined by the site-to-site jump rate $\kappa$, although the master equation (1.2) also allows different rates $\kappa_i$ for jumps spanning multiple sites, and depending on adsorbate-adsorbate interactions.

At a more coarse-grained level, the system can be described by an adsorbate density $\rho(\vec{r}, t)$. In the limit of long-wavelength fluctuations in the density, the above master equation leads to Fick's law for diffusion [9, 11]

$$\frac{\partial \rho}{\partial t} = \nabla \cdot (D_c \nabla \rho), \tag{1.3}$$

where $D_c$ is the collective diffusion coefficient, which can be determined from the transition rates $W(\vec{n} \to \vec{n}')$.

The dynamics of surface diffusion at both low and high coverage is therefore fundamentally determined by the site-to-site jump rate $\kappa$. The focus of this thesis is the development of a method to calculate jump rates for adsorbed organic molecules, accounting for the dynamics of internal molecular degrees of freedom.

## 1.2 Rate Calculations

There exist many approaches for calculating rates of thermally activated processes described phenomenologically by the Arrhenius law (1.1) (see Ref. [12] for a review). The simplest approach is transition state theory (TST), in which the jump rate is calculated from equilibrium statistical mechanics considerations [12]. To find the escape rate of an adsorbed particle from its adsorption site in TST, it is assumed that the particle is in local thermal equilibrium so that the probability density is given by the equilibrium distribution $\rho(\vec{r},\vec{v}) \propto e^{-V(\vec{r})/kT} e^{-mv^2/2kT}$, where $V(\vec{r})$ is a potential energy describing the particle's interaction with the surface. The rate is then calculated as the flux of particles passing through some barrier region (usually taken to be the saddle point on the potential energy surface connecting two neighboring potential wells), normalized to the probability density in the potential well, i.e.

$$\kappa_{\mathrm{TST}} = \frac{\#\text{ of particles at barrier with } v > 0}{\#\text{ of particles at minimum}}, \tag{1.4}$$

where $v > 0$ means that the particle has a velocity pointing in the forward direction across the barrier.

To illustrate the calculation of the TST jump rate, consider the simple model system consisting of a particle diffusing in a one dimensional periodic potential $V(x)$, as shown in Fig. 1.1. Eq. (1.4) then leads to [12]

$$\kappa_{\mathrm{TST}} = \frac{e^{-\Delta V/kT} \int_0^\infty dv v e^{-mv^2/2kT}}{\int_0^a dx e^{-V(x)/kT} \int_{-\infty}^\infty dv e^{-mv^2/2kT}} = \frac{kT}{h} \frac{1}{Z_{\mathrm{vib}}} e^{-\Delta V/kT}, \tag{1.5}$$

where $Z_{\mathrm{vib}}$ is the vibrational partition function at the minimum of the potential well, and $h$ is Planck's constant. In the harmonic approximation, $Z_{\mathrm{vib}} = 2\pi kT/h\omega$ (where $\omega$ is the harmonic vibration frequency at the minimum), and the jump rate becomes

$$\kappa_{\mathrm{TST}} = \frac{\omega}{2\pi} e^{-\Delta V/kT}. \tag{1.6}$$

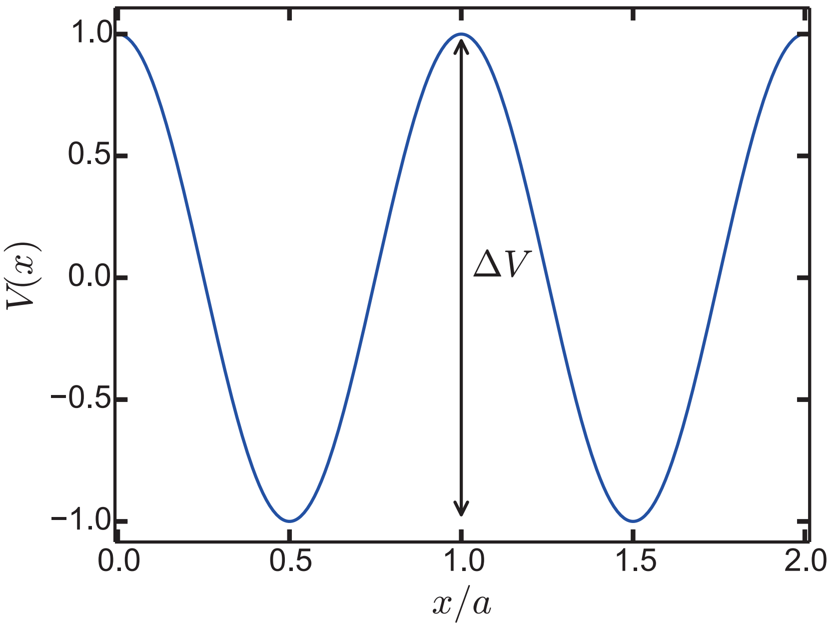

Figure 1.1: One dimensional periodic potential $V(x)$ for an adsorbed atom, with energy barrier of height $\Delta V$, and potential wells separated by length $a$.

The TST rate has the Arrhenius form of Eq. (1.1), i.e. a Boltzmann factor representing the probability to find the particle at the barrier, times a prefactor which can be interpreted as an attempt frequency. In the harmonic approximation, the attempt frequency is simply the vibration frequency at the minimum. For an $N$-dimensional system, the rate generalizes in a straightforward way to [12]

$$\kappa_{\text{TST}} = \frac{kT}{h}\frac{Z_{\text{vib}}^{(b)}}{Z_{\text{vib}}^{(m)}}e^{-\Delta V/kT} \approx \frac{1}{2\pi}\frac{\prod_{i=1}^{N}\omega_i^{(m)}}{\prod_{i=1}^{N-1}\omega_i^{(b)}}e^{-\Delta V/kT}, \tag{1.7}$$

where the labels $(m)$ and $(b)$ refer to the minimum and barrier regions, respectively. Note that there is one less frequency $\omega_i^{(b)}$ at the barrier region, since motion in the unstable direction is excluded.

TST provides a simple way to estimate the rate prefactor from properties of the potential energy surface, however it is not always accurate. The prefactor estimated from Eq. (1.7) is usually on the order of a typical vibration frequency for the diffusing molecule, but measured prefactors can differ from this by several orders of magnitude. For example, tetra-pyridal porphyrin molecules (TPyP) diffusing on a Cu(111) surface were measured to have a rate prefactor of approximately $10^{12}$Hz [6]. When two TPyP molecules came together on the surface to form a stable dimer, the prefactor was seen to increase by two orders of magnitude to $10^{14}$Hz. This is the opposite of what one would naively expect from a TST estimation, since the vibration frequencies for the dimer are expected to be lowered compared to the monomer (due to both its higher mass, and the weaker inter-molecular force holding the dimer together).

TST relies on two main assumptions, the first of which is that once a particle crosses the barrier, it is immediately captured by the neighboring well, i.e. that there is no re-crossing of the barrier. This assumption is valid if energy exchange with the surface is slow compared to the time scale for adsorbate motion, so that a particle moving across the barrier will continue in the same direction until it leaves the barrier region, without being turned around via interactions with the surface. Accounting for the effects of such re-crossings will tend to lower the effective jump rate. The second assumption is that the velocity distribution at the barrier is given by the equilibrium thermal distribution. This assumption is valid if energy exchange with the surface is fast compared to the time scale for adsorbate motion, so that the adsorbed particle rapidly thermalizes at each site before making a jump. If this is not the case, the jump rate can be affected in the following way. When the particle escapes over a barrier it will be in an activated state with an unusually high energy; if the energy exchange with the surface is not fast enough, it may escape over a second barrier before it has time to relax back to a typical equilibrium state, resulting in several jumps in rapid succession (which may be thought of as long jumps spanning multiple lattice sites). This phenomenon has been observed in the surface diffusion of large molecules on metal surfaces [13].

Due to the conflicting requirements for the assumptions made by TST, it can only be valid in an intermediate regime, where energy exchange with the surface is not too fast and not too slow. It is only in this regime that the dynamics of adsorbate motion become unimportant and the escape rate can be calculated from equilibrium considerations. Relaxing these assumptions, and accounting for effects such as long jumps requires a more detailed consideration of the dynamics.

In a classical mechanical model (appropriate for the large molecules considered in this thesis), the most detailed description of the dynamics is obtained by solving the Newtonian equations of motion for the system consisting of the surface and adsorbed

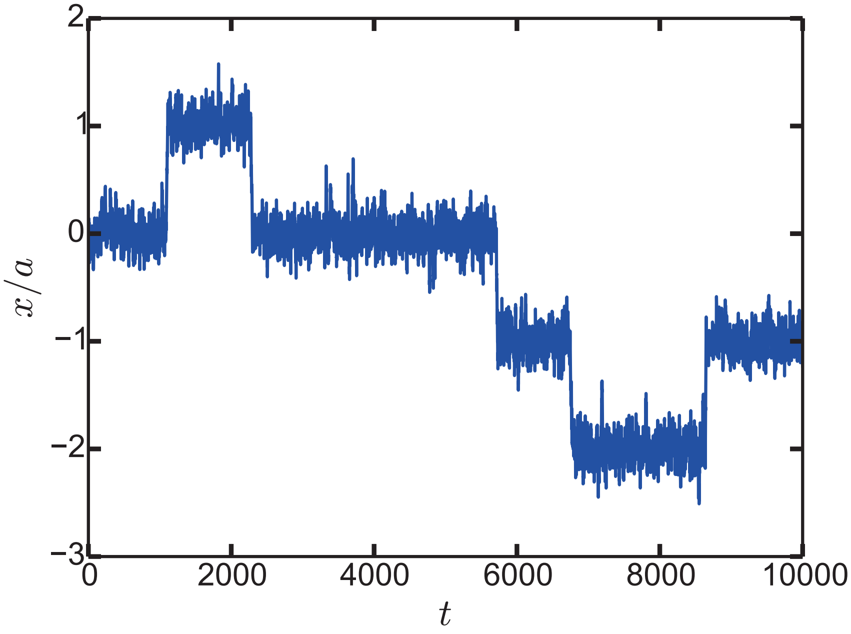

Figure 1.2: Displacement of an atom moving in the potential shown Fig. 1.1. The trajectory is a solution of a one dimensional Langevin equation of the form (1.8) with $F(x) = \sin(2\pi x/a)$ and $\gamma = 1$.

molecule, i.e. molecular dynamics (MD) simulations. For diffusion at low temperatures, however, MD simulations are not feasible due to the large difference in the timescales for vibrational and diffusive motion. The time step in an MD simulation must be chosen according to the shortest timescale in the system, which for surface diffusion is typically the vibrations of the surface atoms. This frequency is many orders of magnitude faster than the jump rate, making a direct simulation of surface diffusion at low temperatures unfeasible.

Fig. 1.2 shows a typical trajectory followed by a particle diffusing along a surface in one dimension, in which case the average force on the particle is described by a periodic potential such as that shown in Fig. 1.1. The motion consists of rapid oscillations around the minimum of the potential wells, punctuated by occasional jumps between neighboring wells, with the jumps occurring on a time scale much longer than the oscillations. For studies of surface diffusion, this short-time vibrational motion of the adsorbed particle is not of interest, nor is the vibrational motion of the atoms making up the surface. A simplified description of the motion can therefore be obtained by replacing the microscopic force on the adsorbed particle with an effective force which reproduces the statistics of the jumps between wells.

In such a stochastic approach, the equation of motion for a single adsorbed atom takes the form of a Langevin equation [14,15],

$$m\ddot{\vec{r}} = \vec{F}(\vec{r}) - \gamma\dot{\vec{r}} + \vec{f}(t), \tag{1.8}$$

where $\vec{F}$ is the average force on the diffusing atom, i.e. the force on the atom with the surface atoms at their equilibrium positions. The friction term and stochastic force $\vec{f}(t)$ account for the exchange of energy between the adsorbed atom and surface, via surface phonons. The two terms are related through the fluctuation-dissipation theorem [14,15],

$$\langle f(t)f(t')\rangle = 2\gamma kT\delta(t-t'), \tag{1.9}$$

ensuring the approach of a system described by Eq. (1.8) to thermal equilibrium. The instantaneous decay of the correlations in the stochastic force $\vec{f}(t)$ is an approximation (the Markov approximation) valid for systems where the motion of the substrate atoms is fast compared to that of the adsorbed atoms. If the surface is treated as an elastic continuum, a simple expression for the friction coefficient $\gamma$ can be derived from the microscopic equations of motion [15,16],

$$\gamma = \frac{3\pi}{2m_s\omega_D^3}\left(\frac{d^2V}{dx^2}\right)^2, \tag{1.10}$$

where $m_s$ is the mass of the surface atoms, and $\omega_D$ is the Debye frequency of the surface, and $V(x)$ is the potential energy of the adsorbed atom. Models based on the Langevin equation (1.8) [14,15,17,18], and equivalent approaches based on the Fokker-Planck equation [16,19,20], or projection operaters [21,22] have been widely used to describe the surface diffusion of adsorbed atoms. These models can successfully describe many aspects of surface diffusion, including those not accounted for in a simple transition state theory (TST) approach, such as long jumps spanning multiple lattice site, and non-Arrhenius behavior at high temperatures.

Applying this approach directly to an adsorbed molecule made up of $N$ atoms would result in $N$ coupled Langevin equations of the type shown in Eq. (1.8). For a large molecule, it becomes impractical to solve such a large set of coupled equations, particularly for the Fokker-Planck equation-based method described in Chapter 2, for which only one or two-dimensional systems are tractable. For the purposes of describing surface diffusion, however, only overall center of mass motion of the molecule is of interest. The internal molecular degrees of freedom (including both vibrations and rotations) can therefore be treated as "background" degrees of freedom on the same footing as the positions of the surface atoms, and will give rise to an additional contribution to the friction coefficient and stochastic force in Eq. (1.8).

Large molecules may also have soft vibrational degrees of freedom that occur on the same timescale as the center of mass motion. These can be either hindered rotations and translations (as we will see in Chapter 5), or long wavelength bending modes. In this case, the Markovian approximation employed in Eq. (1.8) is unrealistic, and the equation of motion takes the more general form [14, 15]

$$m\ddot{\vec{R}} = \vec{F}(\vec{R}) - \int_0^t dt' \Gamma(t-t')\dot{\vec{R}}(t') + \vec{f}(t), \tag{1.11}$$

where $\vec{R}$ is the center of mass coordinate of the diffusing molecule. The stochastic force $f(t)$ has a finite correlation time, and is related to the memory function $\Gamma(t-t')$ by [14, 15]

$$\langle f(t)f(t')\rangle = kT\Gamma(t-t'). \tag{1.12}$$

We employ this stochastic model as the basis of our treatment of molecular surface diffusion.

The connection between this picture of continuous adsorbate diffusion and the discreet jump model described above is provided by the tracer diffusion coefficient. In the long-time limit, the mean squared displacement of a particle undergoing random thermal motion will increase linearly with time; the tracer diffusion coefficient is defined as the proportionality constant,

$$D_t = \lim_{t\to\infty} \frac{\langle|\vec{r}(t)-\vec{r}(0)|^2\rangle}{4t}. \tag{1.13}$$

For a particle undergoing a random walk of discreet jumps, the mean square displacement will also increase linearly with time, proportional to the number of steps $N = t\kappa$, i.e. $\langle|\vec{r}(t)-\vec{r}(0)|^2\rangle = t\kappa\,\langle l^2\rangle$, where $\langle l^2\rangle$ is the mean square length of each jump (determined by the lattice constant). The tracer diffusion coefficient and jump rate are then related by

$$D_t = \frac{1}{4}\kappa \left\langle l^2 \right\rangle . \tag{1.14}$$

A transport equation analogous to Fick's law (1.3) can also be obtained for a diffusing particle described by the Langevin equations (1.8) and (1.11). Though the particle density $\rho(\vec{r})$ is not a meaningful quantity for an isolated particle, one can consider the probability density $\rho(\vec{r}, \vec{v}, t)$ for the particle to have position $\vec{r}$ and velocity $\vec{v}$. In the overdamped limit, the Markovian Langevin equation (1.8) leads to the following equation for the marginal distribution $\bar{\rho}(\vec{r}, t) = \int d\vec{v}\rho(\vec{r}, \vec{v})$ [23, 24]

$$\frac{\partial \bar{\rho}}{\partial t} = \nabla \cdot (D_0 \nabla - \vec{F}(\vec{r})/kT)\bar{\rho}, \tag{1.15}$$

where $D_0 = kT/\gamma$ is the tracer diffusion coefficient in the corresponding homogeneous system (i.e. $\vec{F} = 0$). $D_t$ can then be calculated from Eq. (1.13) using the solution to Eq. (1.15) in the long time limit. For general damping, the equation takes the form of a Fokker-Planck equation for the distribution $\rho(\vec{r}, \vec{v}, t)$ [23, 24].

The layout of the remainder of this thesis is as follows. In Chapter 2 we derive the Langevin equations for adsorbed atoms that are the basis of our stochastic model from the microscopic equations of motion for a system of atoms adsorbed on a surface. We then show how to derive the Fokker-Planck equation corresponding to Langevin dynamics, and give details of the numerical solution we employ to calculate the diffusion coefficient $D_t$.

In Chapter 3 we derive an expression for the contribution of the internal degrees of freedom of a diffusing molecule to the memory function $\Gamma(t - t')$ in Eq. (1.11), and the resulting effective friction in the Markov limit. We apply this model to the simplest molecular system, a dimer diffusing in one dimension, in order to elucidate the qualitative effect the internal degrees of freedom can have on the diffusive motion.

In Chapters 4 and 5 we apply our stochastic model of surface diffusion to a system of experimental interest, dithioanthracene diffusing on a Cu(111) surface. In Chapter 4 we perform density functional theory calculations to obtain the necessary potential energy and vibration frequencies for the stochastic model, and discuss some issues with the accuracy of density functional theory calculations for surface adsorption problems. In Chapter 5 we then make use of the stochastic model to study the diffusion of dithioanthracene, comparing our results with experimental measurements of the jump rate.

Finally, in Chapter 6 we give some concluding remarks as well as an outlook for future studies.

# Chapter 2

# Theoretical Background

In this chapter we outline the necessary theoretical background for the stochastic model of molecular surface diffusion developed in Chapter 3. The starting point for this model is the Langevin equations (LE) for adsorbed atoms, introduced in Eq. (1.8), and we begin with a derivation of the LE from the microscopic equations of motion for the adsorbate-surface system in section 2.1. This derivation can be accomplished with several different methods; here we use a method introduced by Zwanzig [14] for a system where the background particles are treated in the harmonic approximation. A more general method for obtaining Langevin equations is the use of projection operators, and we briefly discuss this method in section 2.2.3.

As discussed in Chapter 1, an advantage of the stochastic approach is that the fast vibrational motion of the surface atoms is eliminated. However, when solving the LE for diffusion at low temperatures, one is still faced with the problem that the timescale for jumps between neighboring potential wells is many orders of magnitude longer than the timescale for vibrational motion within a well. For example, for dithioanthracene diffusing on a Cu(111) surface (a system to be considered in the next chapters) the vibrational frequencies are on the order of $10^{12}$Hz, while the jump frequencies are on the order of $10^{-3} \sim 10^{-1}$Hz. Direct integration of the LE therefore becomes impractical for such systems.

Since the LE is stochastic in nature, its solution generates an ensemble of trajectories rather than a single trajectory. Physical quantities of interest must then be averaged over this ensemble. The diffusion coefficient, for example, can be calculated from the position correlation function [25]

$$D = \lim_{t \to \infty} \frac{\langle (x(t) - x(0))^2 \rangle}{2t}, \tag{2.1}$$

or equivalently in terms of the velocity correlation function, from the Green-Kubo relation [25]

$$D = \int_0^\infty dt \, \langle v(t)v(0) \rangle \, . \tag{2.2}$$

The averages in Eqs. (2.1) and (2.2) can be calculated by averaging over many trajectories obtained by solving the LE. One can also consider the probability density for the ensemble generated by solutions of the LE. The averages can then be calculated as moments of this distribution, e.g.

$$\langle v(t)v(0) \rangle = \int dx \int dv \int dx_0 \int dv_0 \rho(x, v, t; x_0, v_0) v v_0, \tag{2.3}$$

where $\rho(x, v, t; x_0, v_0)$ is the joint probability for the particle to have position $x$ and velocity $v$ at time $t$, and initial position $x_0$ and velocity $v_0$. Rather than solving the LE directly, an equation for the probability density $\rho$ can be derived. In the case of Markovian friction, this equation takes the form of a Fokker-Planck equation (FPE) [23, 24],

$$\frac{\partial \rho}{\partial t} = L\rho, \tag{2.4}$$

where $L$ is a second order differential operator in the position and velocity variables. This FPE can be solved efficiently by the matrix continued fraction (MCF) method of Risken [24], thus avoiding the problem of separation of time scales in the LE at low temperatures.

In section 2.2, we will derive the FPE corresponding to the LE of Eq. (1.8), and give the equation corresponding to the general non-Markovian LE of Eq.(1.11). We will then outline, in section 2.3, the use of the MCF method to calculate the diffusion coefficient in a periodic potential, appropriate for the treatment of surface diffusion.

## 2.1 Langevin Equation

Consider a system of adsorbed atoms with masses $m_i$ and positions $\vec{r}_i$. The atoms of the solid have mass $m_s$, and we denote their positions by $\vec{R}_i$. To account for the vibrations of the substrate atoms, we write

$$\vec{R}_i = \vec{R}_i^{(0)} + \vec{u}_i, \tag{2.5}$$

where $\vec{u}_i$ is the deviation from the equilibrium position $\vec{R}_i^{(0)}$. The interactions between the atoms are described by a potential energy $V(\{\vec{r}_i\},\{\vec{u}_i\})$. The Newtonian equations of motion for the system are

$$\begin{aligned} m_i\ddot{\vec{r}}_i &= -\nabla_{r_i}V(\{\vec{r}_i\},\{\vec{u}_i\}) \\ m_s\ddot{\vec{u}}_i &= -\nabla_{u_i}V(\{\vec{r}_i\},\{\vec{u}_i\}) \end{aligned}. \tag{2.6}$$

Expanding the potential to second order in the displacements $\vec{u}_i$ gives

$$V(\{\vec{r}_i\},\{\vec{u}_i\}) = V_0(\{\vec{r}_i\}) + \sum_i \vec{g}_i\cdot\vec{u}_i + \frac{1}{2}\sum_{i,j}\vec{u}_i^T\cdot\mathbf{K}_{ij}\cdot\vec{u}_j, \tag{2.7}$$

where $\vec{g}_i = \nabla_{u_i}V|_{\{\vec{u}_i=0\}}$, and $\mathbf{K}_{ij} = \nabla_{u_i}\nabla_{u_j}V|_{\{\vec{u}_i=0\}}$ . In the derivation that is to follow, the second derivatives $\mathbf{K}_{ij}$ must be assumed to be constant, while the $\vec{g}_i$'s can depend on the adatom positions $\vec{r}_i$ (i.e. a linear coupling between the adsorbed atoms and the surface atoms is assumed). Now consider the normal mode coordinates $q_k$ for the substrate vibrations, with corresponding vibration frequencies $\omega_i$ and eigenvectors $\hat{q}_k$. The potential then becomes

$$V(\{\vec{r}_n\},\{q_k\}) = V_0(\{\vec{r}_n\}) + \sum_k \phi_k q_k + \frac{1}{2}\sum_k \omega_k^2|q_k|^2, \tag{2.8}$$

where $\phi_k = \frac{\partial V}{\partial q_k}\Big|_{\{q_k\}=0}$. The equations of motion then become

$$m_i\ddot{\vec{r}}_i + \nabla_{r_i}V_0 + \sum_k q_k\nabla_{r_i}\phi_k = 0 \tag{2.9}$$

$$\ddot{q}_k + \omega_k^2 q_k + \phi_k^* = 0, \tag{2.10}$$

where $\phi_k^*$ denotes the complex conjugate of $\phi_k$.

The equations for $q_k$ are simply uncoupled driven harmonic oscillators, which can be solved analytically. By substituting the solutions into Eq. (2.9) we will obtain a set of Langevin equations for the adatom positions $\vec{r}_i$. Eqs. (2.10) have the solutions

$$q_k(t) = q_k(0)\cos(\omega_k t) + \frac{1}{\omega_k}\dot{q}_k(0)\sin(\omega_k t) - \frac{1}{\omega_k}\int_0^t \sin[\omega_k(t-t')]\phi_k^*(\{\vec{r}_n(t')\})dt'. \tag{2.11}$$

To make Eq. (2.9) take the form of a Langevin equation, we must rewrite (2.11) using integration by parts,

$$q_k(t) = \left[q_k(0) + \frac{1}{\omega_k}\phi_k^*(\{\vec{r}_n(0)\})\right]\cos(\omega_k t) + \frac{1}{\omega_k}\dot{q}_k(0)\sin(\omega_k t) - \frac{1}{\omega_k^2}\phi_k^*(\{\vec{r}_n(t)\})$$
$$+ \frac{1}{\omega_k^2}\int_0^t \cos[\omega_k(t-t')]\sum_j \nabla_{r_j}\phi_k^*(\{\vec{r}_n(t')\})\cdot\dot{\vec{r}}_j(t')dt'. \tag{2.12}$$

Making use of these solutions, Eq. (2.9) becomes

$$m_i\ddot{\vec{r}}_i = -\nabla_{r_i}V_a - \sum_j\int_0^t \mathbf{\Gamma}_{ij}\cdot\dot{\vec{r}}_j(t')dt' + \vec{f}_i, \tag{2.13}$$

where

$$\mathbf{\Gamma}_{ij}[\{\vec{r}_n(t)\},\{\vec{r}_n(t')\},t-t'] = \sum_k \frac{\cos[\omega_k(t-t')]}{\omega_k^2} \times \nabla_{r_i}\phi_k(\{\vec{r}_n(t)\})\nabla_{r_j}\phi_k^*(\{\vec{r}_n(t')\}), \tag{2.14}$$

$$V_a = V_0 - \frac{1}{2}\sum_k\frac{|\phi_k|^2}{\omega_k^2}, \tag{2.15}$$

$$\vec{f}_i(\{\vec{r}_n(t)\},t) = -\sum_k\left[\left(q_k(0) + \frac{\phi_k^*(\{\vec{r}_n(0)\})}{\omega_k^2}\right)\cos(\omega_k t) + \frac{\dot{q}_k(0)}{\omega_k}\sin(\omega_k t)\right] \times \nabla_{r_i}\phi_k(\{\vec{r}_n(t)\}). \tag{2.16}$$

Eq. (2.13) has the form of a generalized Langevin equation (GLE) for the $i$th adatom, with memory function $\mathbf{\Gamma}_{ij}$ and stochastic force $\vec{f}_i$. The stochastic nature of $\vec{f}_i$ comes from its dependence on the initial conditions $q_k(0), \dot{q}_k(0)$, which we denote collectively by $X$. Assuming the system is initially in thermal equilibrium the probability of a set of initial conditions is given by

$$\rho(X) = \frac{1}{Z}e^{-E_X/k_BT}, \tag{2.17}$$

where $E_X = \sum_k(|\dot{q}_k(0)|^2/2 + \omega_k^2|q_k(0)|^2/2)$, and $Z = \int dXe^{-E_X/k_BT}$ is the partition function. The average of a quantity $A(X)$ is then given by

$$\langle A\rangle = \frac{1}{Z}\int dXA(X)\rho(X). \tag{2.18}$$

Using this averaging procedure, it is easy to show that the average force is zero,

$$\langle\vec{f}_i(\{\vec{r}_n\},t)\rangle = 0, \tag{2.19}$$

as expected for a Langevin force [23, 24].

The memory term and random force both arise from interaction of the adsorbed atoms with the phonons, and they are related by the fluctuation-dissipation theorem [23, 24]

$$\langle \vec{f}_i(\{\vec{r}_n(t)\},t)\vec{f}_j(\{\vec{r}_n(t')\},t')\rangle = k_B T \mathbf{\Gamma}_{ij}[\{\vec{r}_n(t)\},\{\vec{r}_n(t')\},t-t'], \tag{2.20}$$

which can be verified by making use of Eqs. (2.16) and (2.14). The memory term therefore arises from the finite time correlations of the random force. If these correlations decay quickly compared to the timescale of interest, the random force can be treated as being uncorrelated in time, $\langle \vec{f}(t)\vec{f}(t')\rangle \sim \delta(t-t')$. The integral in the memory term in Eq. (2.13) then disappears, and a simple friction term is recovered, leading to the LE

$$m_i \ddot{\vec{r}}_i = -\nabla_{r_i} V_a - \sum_j \boldsymbol{\gamma}_{ij} \cdot \dot{\vec{r}}_j + \vec{f}_i. \tag{2.21}$$

This is termed the Markov approximation (a Markov process is one in which the state of the system at time $t + dt$ depends only on the state of the system at time $t$ [23]), and the stochastic force $\vec{f}_i(t)$ is called white noise. The statistical properties of the stochastic forces in this approximation are

$$\left\langle \vec{f}_i(t) \right\rangle = 0 \qquad\qquad \left\langle \vec{f}_i(t)\vec{f}_i(t') \right\rangle = 2kT\boldsymbol{\gamma}_{ij}\delta(t-t'). \tag{2.22}$$

If the surface vibrations are described within the Debye model, it can be shown that the Markov approximation is valid in the limit that the Debye frequency $\omega_D$ is fast compared to the time scale of interest [15], and the friction coefficients are given by the expression

$$\boldsymbol{\gamma}_{ij} = \frac{3\pi}{2m_s\omega_D^3}\nabla_{r_i}V_a\nabla_{r_j}V_a. \tag{2.23}$$

This condition is usually satisfied for surface diffusion on metal surfaces, where typical Debye frequencies are on the order of $10^{13}$Hz, while typical vibration frequencies for adsorbates are on the order of $10^{12}$Hz.

The potential energy appearing in the LE (2.21) and GLE (2.13) is called the adiabatic potential. In general, $V_a$ is defined by an average over the positions of the substrate atoms in the following way

$$e^{-V_a(\vec{r})/kT} = \int d\vec{q} e^{-V(\vec{r},\vec{q})/kT}/Z. \tag{2.24}$$

The adiabatic potential defined in this way is the potential of mean force for the adsorbed atoms,

$$\langle \nabla_{r_i} V(\{\vec{r}_n\}, \{q_k\}\rangle = \nabla_{r_i} V_a(\{\vec{r}_n\}), \tag{2.25}$$

where the average is performed over the substrate degrees of freedom as in Eq. (2.18). The expression for $V_a$ given in Eq. (2.15) is simply this average calculated using the harmonic approximation to the potential, Eq. (2.8). Effects beyond the harmonic approximation in the background degrees of freedom (including thermal expansion of the surface) can therefore be incorporated into the GLE (2.13) by evaluating the adiabatic potential using Eq. (2.24) rather than Eq. (2.15). This point is discussed further in section 2.2 and later in Chapter 3.

## 2.2 Fokker-Planck Equation

In this section we consider the FPE for the probability density $\rho(\vec{r}, \vec{v}, t)$ for a system described by the LE's derived in the previous section. This provides an alternative, mathematically equivalent description of the system which is sometimes more convenient to work with. For surface diffusion, the FPE description allows for a much more efficient calculation of the diffusion coefficient, by avoiding the problem of separation of time scales in the vibrational and diffusive motion.

### 2.2.1 Markovian Langevin Equation

We first consider the one-dimensional LE with Markovian friction,

$$m\dot{v} = F(r) - \gamma v + f(t), \tag{2.26}$$

where the stochastic force $f(t)$ is Gaussian white noise, and satisfies

$$\begin{aligned} \langle f(t) \rangle &= 0 \\ \langle f(t) f(t') \rangle &= 2kT\gamma\delta(t - t'). \end{aligned} \tag{2.27}$$

Following Ref. [26], an equation for the probability density can be obtained by considering the equation of motion for an arbitrary function of the position and velocity $y = g(r, v)$. Applying this transformation of variables to the above LE, and using the rules of Ito calculus [26] (for an equation of the form (2.26) where the stochastic force has no velocity dependence, there is no difference between the Ito and Stratonovich pictures [23]) gives

$$\dot{y} = \frac{\partial g}{\partial r} v + \frac{\partial g}{\partial v}(F - \gamma v + f)/m + \frac{\partial^2 g}{\partial v^2}\frac{kT\gamma}{m^2}. \tag{2.28}$$

Upon taking the average of both sides, the term involving the stochastic force $f(t)$ will vanish, giving

$$\frac{\partial \langle y \rangle}{\partial t} = \left\langle \frac{\partial g}{\partial r} v \right\rangle + \left\langle \frac{\partial g}{\partial v}(F - \gamma v)/m \right\rangle + \left\langle \frac{\partial^2 g}{\partial v^2} \right\rangle \frac{kT\gamma}{m^2}. \tag{2.29}$$

This can be written in terms of the probability density $\rho(r, v, t)$ as

$$\begin{aligned} \frac{\partial \langle y \rangle}{\partial t} &= \int dr \int dv \left[\frac{\partial g}{\partial r} v + \frac{\partial g}{\partial v}(F - \gamma v)/m + \frac{\partial^2 g}{\partial v^2}\frac{kT\gamma}{m^2}\right] \rho(r, v, t) \\ &= \int dr \int dv \left[-v\frac{\partial \rho}{\partial r} - (F/m)\frac{\partial \rho}{\partial v} + \frac{\gamma}{m}\frac{\partial}{\partial v}\left(v + \frac{kT}{m}\frac{\partial}{\partial v}\right)\rho\right] g(r, v), \end{aligned} \tag{2.30}$$

where integration by parts has been used in the second line. Since the left hand side can be written as $\frac{\partial \langle y \rangle}{\partial t} = \int dr \int dv g(r, v) \frac{\partial \rho}{\partial t}$, and Eq. (2.30) must be true for any function $g(x, v)$, the following equation for the probability density must hold

$$\frac{\partial \rho}{\partial t} = -v\frac{\partial \rho}{\partial r} - (F/m)\frac{\partial \rho}{\partial v} + \frac{\gamma}{m}\frac{\partial}{\partial v}\left(v + \frac{kT}{m}\frac{\partial}{\partial v}\right)\rho. \tag{2.31}$$

This is the FPE for the probability density corresponding to the Langevin equation (2.26).

For an $N$-dimensional system of Langevin equations,

$$M \cdot \dot{\vec{v}} = \vec{F}(\vec{r}) - \gamma \cdot \vec{v} + \vec{f}(t), \qquad \begin{array}{c} \left\langle \vec{f}(t) \right\rangle = 0 \\ \left\langle \vec{f}(t)\vec{f}(t') \right\rangle = 2kT\gamma\delta(t - t') \end{array}, \tag{2.32}$$

similar arguments lead to the following FPE

$$\frac{\partial \rho}{\partial t} = -\vec{v} \cdot \nabla_{\vec{r}}\rho - \vec{F}(\vec{r}) \cdot M^{-1} \cdot \nabla_{\vec{v}}\rho + \nabla_{\vec{v}} \cdot M^{-1} \cdot \gamma \cdot \left(\vec{v} + kTM^{-1} \cdot \nabla_{\vec{v}}\right)\rho. \tag{2.33}$$

Here $M$ is a matrix with the particle masses on the diagonal, and $\gamma$ is a matrix of friction coefficients.

### 2.2.2 Generalized Langevin Equation

Consider now the GLE with memory,

$$M \cdot \dot{\vec{v}} = \vec{F}(\vec{r}) - \int_0^t dt' \Gamma(\vec{r}(t), \vec{r}(t'), t-t')\vec{v}(t') + \vec{f}(t), \tag{2.34}$$

where the stochastic force $\vec{f}(t)$ is Gaussian, but with a finite correlation time, satisfying

$$\left\langle \vec{f} \right\rangle = 0, \qquad\qquad \left\langle \vec{f}(t)\vec{f}(t') \right\rangle = kT\Gamma(\vec{r}(t), \vec{r}(t'), |t-t'|). \tag{2.35}$$

The equation for the probability density in this case is considerably more complicated than the FPE,

$$\begin{aligned} \frac{\partial \rho}{\partial t} &= -\vec{v} \cdot \nabla_{\vec{r}} \rho - \vec{F}(\vec{r}) \cdot M^{-1} \cdot \nabla_{\vec{v}} \rho \\ &\quad + \int_0^t dt' \int d\vec{r'} \int d\vec{v'} \nabla_{\vec{v}} \cdot M^{-1} \cdot \Theta(\vec{r}, \vec{r'}, t-t') \cdot \left( \vec{v'} + kTM^{-1} \cdot \nabla_{\vec{v'}} \right) \rho(\vec{r'}, \vec{v'}, t'), \end{aligned} \tag{2.36}$$

where $\Theta(\vec{r}, \vec{r'}, t-t') = \Gamma(\vec{r}, \vec{r'}, t-t')\rho(\vec{r}, \vec{v}, t-t'|\vec{r'}, \vec{v'})$. This generalized FPE is non-local in time, as well as the position and velocity variables. The presence of the probability density $\rho(\vec{r}, \vec{v}, t-t'|\vec{r'}, \vec{v'})$ in the memory function $\Theta$ also makes the equation non-linear, greatly complicating its solution.

The need to work with a non-Markovian FPE such as Eq. (2.36) can sometimes be avoided by explicitly including more degrees of freedom in the equations of motion. The source of the memory term in a non-Markovian equation is degrees of freedom whose motion occurs on the same time scale as, or slower than, the degrees of freedom of interest. For an adsorbed molecule, this could include vibrational or rotational degrees of freedom that occur on the same time scale as center of mass motion, while surface vibrations are fast compared to center of mass motion. Explicitly including these slow degrees of freedom in the equations of motion will then result in a Markovian LE (or FPE) of higher dimensionality. In Chapter 3, we will take advantage of this approach when studying a dimer in one dimension by working with the two-variable Markovian FPE including both molecular degrees of freedom, rather than the generalized FPE including only the center of mass coordinate.

In Chapter 5, where diffusion of a molecule with many vibrational degrees of freedom is studied, this approach is no longer feasible. We will therefore consider an approximate solution for the jump rate in a system described by Eq. (2.36) in order to estimate the importance of memory effects for diffusion. This approximation, the Grote-Hynes theory [27], is valid when the energy barrier is large compared to $kT$, and the friction is not too small compared to typical vibration frequencies (both assumptions are found to be valid for the system studied in Chapter 5). In the Grote-Hynes approximation, the jump rate is given by

$$\kappa = \frac{\lambda}{\omega_b} \frac{\omega_m}{2\pi} e^{-\Delta V/kT}, \tag{2.37}$$

where $\omega_m$ and $\omega_b$ are the harmonic vibration frequencies at the minimum and barrier regions, and $\lambda$ is determined by the following equation

$$\lambda = \frac{\omega_b^2}{\lambda + \hat{\Gamma}(\lambda)/M}, \tag{2.38}$$

where $\hat{\Gamma}(\lambda)$ is the Laplace transform of the memory function, and $M$ is the total mass of the molecule.

### 2.2.3 Projection Operator Methods

Generalized Langevin equations, and their corresponding generalized FPE's, can also be derived from the microscopic equations of motion using the projection operator technique of Mori [28]. The basic idea of the Mori projection operator technique is to derive an equation of motion for the "slow" variables $X_i$ of the system of interest by operating on the basic equations of motion with a projection operator that averages out the effect of the "fast" variables (in the case of surface diffusion, the coordinates and momenta of the vibrating atoms of the surface). The projection operator $\hat{P}_i$ onto the variable $X_i$ is defined such that for some function of the microscopic variables $A$,

$$\hat{P}_i A = X_i \chi_{ij}^{-1} \left\langle X_j A \right\rangle, \tag{2.39}$$

where here, and for the rest of this section Einstein summation notation is used for the repeated indices. $\langle X \rangle$ denotes the average of $X$ over an equilibrium ensemble, and $\chi$ is the susceptibility matrix, defined as

$$\chi_{ij} = \left\langle X_i X_j \right\rangle. \tag{2.40}$$

The following equations of motion for the $X_i$ can then be derived [28]

$$\frac{dX_i}{dt}(t) = \Omega_{ij}X_j(t) - \int_0^t dt'\Gamma_{ij}(t-t')X_j(t') + f_i(t). \tag{2.41}$$

The "adiabatic" or average force is given by the first term, while the effects of the fast motion of the background particles are contained in the random forces $f_i$ and the memory functions $\Gamma_{ij}$. The various terms in Eq. (2.41) are given by

$$\begin{aligned} \Omega_{ij} &= \left\langle \dot{X}_i X_k \right\rangle \chi_{kj}^{-1} \\ f_i(t) &= e^{i\hat{Q}\mathcal{L}\hat{Q}t}\hat{Q}\dot{X}_i \\ \Gamma_{ij}(t-t') &= \left\langle \hat{Q}\dot{X}_i e^{i\hat{Q}\mathcal{L}\hat{Q}(t-t')}\hat{Q}\dot{X}_k \right\rangle \chi_{kj}^{-1}, \end{aligned} \tag{2.42}$$

where $\hat{Q} = 1 - \sum_i \hat{P}_i$ can be thought of as projecting into a subspace orthogonal to the variables $X_i$, in the sense that it is uncorrelated with all the $X_i$, i.e. $\left\langle X_i(\hat{Q}A) \right\rangle = 0$ for any quantity $A$. The operator $\mathcal{L}$ is the Liouville operator, defined so that the microscopic equations of motion for the variables are given by

$$\dot{X}_i = i\mathcal{L}X_i. \tag{2.43}$$

In analogy to Eq. (2.20) for the random force of the usual GLE for surface diffusion, the random forces here satisfy

$$\langle f_i(t)X_j \rangle = 0 \tag{2.44}$$

$$\langle f_i(t)f_j(t') \rangle = \Gamma_{ik}\chi_{kj}. \tag{2.45}$$

For a diffusing particle with position and velocity $\vec{r}$ and $\vec{v}$, if one takes as the variables $X_i$ a set of functions complete in $\vec{r}$ and $\vec{v}$, the projection operator method gives a generalized Langevin equation of the type shown in Eq. (2.32), but with a memory term that in general depends non-linearly on the velocity. The same method can also be used to derive equations of motion for correlation functions of the variables $X_i$. A generalized FPE corresponding to the Langevin equation can be derived in this way, since the probability density can be thought of as the correlation function

$$\rho(\vec{x},\vec{u},t) = \langle \delta(\vec{x} - \vec{r}(t))\delta(\vec{u} - \vec{v}(t)) \rangle, \tag{2.46}$$

resulting in an equation of the form shown in Eq. (2.36). This approach has been used by Ying *et al.* to study the surface diffusion of adatoms [21, 29]. Rather than working with the generalized FPE directly, they use the projection operator formalism to derive equations of motion for correlation functions of interest.

The force appearing in the Langevin and Fokker-Planck equations obtained in the projection operator method is exactly the adiabatic force defined in Eq. (2.24), which can be shown from the expression for the force in Eq. (2.42). This provides a firm justification for the approach mentioned above in section 2.1, where the effective force in the Langevin equation obtained in the harmonic approximation is replaced with the adiabatic force as defined in Eq. (2.24). It may seem questionable to combine an equation of motion derived in the harmonic approximation with a force term derived from a different model. However, using the projection operator method, an equation of motion with a force term that is exactly the adiabatic force and with the same form as the GLE derived in section 2.1 can be derived rigorously from the microscopic equations of motion. The difference between the two equations lies in the memory and stochastic force terms.

In the method of section 2.1, the memory term and stochastic force are given by Eqs. (2.14) and (2.16), while in the projection operator method, they must be evaluated using Eq. (2.42). The generalized Langevin equation Eq. (2.41) is a formally exact equation of motion for the variables $X_i$ (no approximations have been made in deriving it). An exact evaluation of the random force and memory function would therefore amount to a solution of the full N-body problem of the system of interest plus the background particles, and so it is generally not possible. In order to make use of this GLE, approximations for these terms must therefore be made. The formal expressions in Eq. (2.42) are, however, difficult to deal with due to the presence of the projection operators. The method given in section 2.1 for deriving the GLE can then be viewed as a convenient approximation scheme for the memory and stochastic force terms appearing in the GLE (2.41). This approximation is physically intuitive and simple to apply, and allows one to avoid working directly with the expressions in Eq. (2.42), which require an approximation to the complicated operator $e^{i\hat{Q}\mathcal{L}\hat{Q}t}$. The approach of section 2.1 will be used later in Chapter 3 to account for differences in vibrational entropy as a adsorbed dimer moves across the surface.

## 2.3 Numerical Solution of Fokker-Planck Equation

To solve Eq. (2.33), the probability density is expanded in a complete set of functions for each variable. For example, in one dimension, $\rho(r, v, t)$ is written as

$$\rho(r, v, t) = \sum_{n,\nu} C_{n\nu}(t)\phi_n(r)\psi_\nu(v). \tag{2.47}$$

Provided an orthonormal set of functions $\phi_n$ for the position variable, and $\psi_\nu$ for the velocity variable are chosen, the coefficients $C_{n\nu}$ are related to the probability density by

$$C_{n\nu}(t) = \big[\phi_n\psi_\nu, \rho(t)\big], \tag{2.48}$$

where $\big[A, B\big]$ is the inner product of $A$ and $B$, defined by the integral

$$\big[A, B\big] = \int dr \int dv A(r, v)B(r, v). \tag{2.49}$$

The FPE then becomes a matrix equation,

$$\frac{\partial}{\partial t} C_{m\mu}(t) = L_{m\mu,n\nu}C_{n\nu}(t), \tag{2.50}$$

where $L_{m\mu,n\nu}$ are the matrix elements of the Fokker-Planck (FP) operator in the chosen basis,

$$L_{m\mu,n\nu} = \big[\phi_m\psi_\mu, L\phi_n\psi_\nu\big]. \tag{2.51}$$

The FPE in this form is solved by taking the Laplace transform of the equation, giving

$$(z - L_{m\mu,n\nu})\hat{C}_{n\nu}(z) = C_{m\mu}(0), \tag{2.52}$$

where $\hat{C}_{n\nu}(z)$ is the Laplace transform of $C_{n\nu}(t)$, defined as

$$\hat{C}(z) = \mathbf{L}[C(t)](z) \equiv \int_0^\infty dte^{-zt}C(t). \tag{2.53}$$

The matrix $z - L$ can then be inverted to give the Laplace transform $\hat{C}(z)$.

To calculate correlation functions we will need to consider the conditional probability distribution $\rho(r, v, t|r_0, v_0)$, the probability for the particle to have position and velocity $r, v$ at time $t$ given initial position and velocity $r_0, v_0$. This conditional distribution is the Green's function of the FPE, i.e. the solution with initial condition

$$\rho(r, v, t = 0) = \delta(r - r_0)\delta(v - v_0). \tag{2.54}$$

$\rho(r, v, t|r_0, v_0)$ can be expanded in both sets of variables $r, v$ and $r_0, v_0$, with coefficients

$$C_{m\mu,n\nu} = \big[\phi_m(r)\psi_\mu(v)\phi_n(r_0)\psi_\nu(v_0), \rho(r, v, t|r_0, v_0)\big], \tag{2.55}$$

and the FPE (2.52) becomes

$$(z - L_{m\mu,a\alpha})\hat{C}_{a\alpha,n\nu}(z) = C_{m\mu,n\nu}(0) = \delta_{m,n}\delta_{\mu,\nu}. \tag{2.56}$$

The problem can be made more numerically tractable by choosing a favourable set of basis functions for the expansion. For the velocity variables, Hermite functions are the optimal choice, since the FP operator becomes tridiagonal in the indices corresponding to these functions. That is, the elements of the matrix $L_{m\mu,n\nu}$ are zero if $\nu > \mu + 1$ or $\nu < \mu - 1$. This allows the use of the efficient tridiagonal matrix algorithm to solve the system (2.56). For the position variables, a Fourier series can be used for coordinates where the force is periodic, or Hermite functions can again be used for coordinates which the force confines to a finite region (such as for vibrational coordinates).

This method is known as the matrix continued fraction method, since an application of the tridiagonal matrix algorithm to the transformed FPE (2.56) gives the solution to $\hat{C}_{m\mu,n\nu}(z)$ in terms of a continued fraction of matrices derived from the FP operator. See Ref. [24] for a detailed account of the MCF method, and e.g. Ref. [19] for an application of the MCF method to diffusion in a periodic system.

### 2.3.1 Matrix Elements of the Fokker-Planck Operator

Use of the MCF method to solve the FPE requires a calculation of the matrix elements of the FP operator. To calculate these matrix elements, it is convenient to introduce the following scaled variables

$$\bar{r} = \frac{2\pi}{a}r \quad \bar{t} = \frac{2\pi}{a}\sqrt{\frac{kT}{m}}t \quad \bar{v} = \sqrt{\frac{m}{kT}}v \quad \bar{\gamma} = \frac{a}{2\pi}\sqrt{\frac{1}{mkT}}\gamma \quad \bar{F} = \frac{a}{2\pi kT}F. \tag{2.57}$$

It will also be helpful to apply the following transformation to the FPE

$$L' = e^{V(r)/2+v^2/4} L e^{-V(r)/2-v^2/4} \qquad \rho' = e^{-V(r_0)/2-v_0^2/4} e^{V(r)/2+v^2/4}\rho. \tag{2.58}$$

This transformation leaves the form of the FPE unchanged, so that $\dot{\rho}' = L'\rho'$. The transformed FP operator then becomes

$$L' = -(bD + b^\dagger \hat{D} + \gamma b^\dagger b), \tag{2.59}$$

in terms of the following differential operators,

$$\begin{aligned} b &= \frac{\partial}{\partial \bar{v}} + \frac{1}{2}\bar{v} & b^\dagger &= -\frac{\partial}{\partial \bar{v}} + \frac{1}{2}\bar{v} \\ D &= \frac{\partial}{\partial \bar{r}} + \frac{1}{2}\bar{F}(\bar{r}) & \hat{D} &= \frac{\partial}{\partial \bar{r}} - \frac{1}{2}\bar{F}(\bar{r}). \end{aligned} \tag{2.60}$$

To solve the FPE, we must find the matrix elements of the operators $b, b^\dagger, D, \hat{D}$ in the chosen basis.

The $b$ and $\hat{b}$ operators can be recognized as the creation and annihilation operators for the Hermite functions,

$$b\psi_n(\bar{v}) = \sqrt{n}\psi_{n-1}(\bar{v}) \qquad b^\dagger\psi_n(\bar{v}) = \sqrt{n+1}\psi_{n+1}(\bar{v}). \tag{2.61}$$

where the $\psi_n$'s are defined as

$$\psi_n(v) = \sqrt{\frac{n!}{2^n\sqrt{2\pi}}} H_n(v/\sqrt{2}) e^{-v^2/4}, \tag{2.62}$$

and $H_n$ are the Hermite polynomials. Looking at Eq. (2.58) for the FP operator, the benefit of using Hermite functions as the basis for the velocity variable is now clear. With this choice of basis, the matrix elements of $b$ and $b^\dagger$ can easily be found from the properties given in Eqs. (2.61), and the matrix elements for the three terms in $L'$ take the following tridiagonal form

$$[bD]_{m\mu,n\nu} = \sqrt{\nu}\delta_{\mu,\nu-1}D_{mn} \tag{2.63}$$

$$[b^\dagger \hat{D}]_{m\mu,n\nu} = \sqrt{\nu+1}\delta_{\mu,\nu+1}\hat{D}_{mn} \tag{2.64}$$

$$[\gamma b^\dagger b]_{m\mu,n\nu} = \gamma\mu\delta_{m,n}\delta_{\mu,\nu}. \tag{2.65}$$

The matrix elements $D_{mn}$ and $\hat{D}_{mn}$ depend on the choice of basis for the position variable, and in general must be evaluated numerically. However, for the 1D dimer studied Chapter 3, they can be calculated analytically, and we give the resulting matrix elements in Appendix A.

### 2.3.2 Calculation of Diffusion Coefficient

Physical quantities of interest can be calculated in terms of correlation functions in the position and velocity variables. The quantity of most direct experimental relevance for surface diffusion at low coverage is the tracer diffusion coefficient, which is related to the jump rate as explained in Chapter 1. The simplest way to calculate the diffusion coefficient from the FPE is to use the relationship

$$D_t = \int_0^\infty dt\, \langle v(t)v(0)\rangle = \lim_{z\to 0} \mathbf{L}[\langle v(t)v(0)\rangle](z), \tag{2.66}$$

where $\mathbf{L}[\langle v(t)v(0)\rangle](z)$ is the Laplace transform of the correlation function.

The velocity autocorrelation function needed to calculate $D_t$ is related to the conditional probability distribution $\rho(r, v, t|r_0, v_0)$ through

$$\langle v(t)v(0)\rangle = \int dr \int dv \int dr_0 \int dv_0 \rho(r, v, t|r_0, v_0)\rho_0(r_0, v_0)vv_0, \tag{2.67}$$

where $\rho_0(r_0, v_0)$ is the initial probability distribution. To calculate the velocity autocorrelation function, and then $D_t$, by solving the FPE, we wish to relate these quantities to the coefficients $C_{m\mu,n\nu}(z)$. The Hermite function $\psi_\mu(v)$ with $\mu = 1$ is linear in the velocity,

$$\psi_1(v) = ve^{-v^2/4}. \tag{2.68}$$

The velocity correlation function can therefore be related to the $C_{m1,n1}(z)$ coefficients, given by

$$C_{i1,k1}(z) = \int_0^\infty dte^{-zt} \int dr \int dv \int dr_0 \int dv_0 \rho'(r, v, t|r_0, v_0)\phi_i(r)\phi_k(r_0)vv_0e^{-v^2/4}e^{-v_0^2/4}. \tag{2.69}$$

The integrand, written here in terms of the scaled probability $\rho'$, can be rewritten as

$$\begin{aligned}\rho(r, v, t|r_0, v_0)\phi_i(r)\phi_k(r_0)e^{-v_0^2/2}e^{-V(r_0)/2}e^{V(r)/2}vv_0 \\ = \rho(r, v, t|r_0, v_0)\rho_{\text{eq}}(r_0, v_0)Ne^{V(r_0)/2}e^{V(r)/2}\phi_i(r)\phi_k(r_0)vv_0,\end{aligned}$$

where $\rho_{\text{eq}}(r_0, v_0) = e^{-V(r_0)}e^{-v_0^2/2}/N$ is the equilibrium probability density, with the normalization factor

$$N = \sqrt{2\pi} \int dre^{-V(r)}. \tag{2.70}$$

The velocity autocorrelation function can be recovered by making use of the expansions of $e^{-V(r)/2}$ and $e^{-V(r_0)/2}$ in terms of the basis functions $\phi_m(r)$, $\phi_n(r_0)$, so that, e.g.,

$$e^{-V(r)/2} = \sum_m P_m \phi_m(r), \tag{2.71}$$

with $P_m = \left[\phi_m, e^{-V/2}\right]$. We then have

$$\mathbf{L}[\langle v(t)v(0)\rangle](z) = \sum_{m,n} P_m C_{m1,n1}(z) P_n / N. \tag{2.72}$$

With this expression, the coefficients $C_{m1,n1}(z)$ obtained from a solution of the FPE (2.56) can be used to calculate the diffusion coefficient.

## 2.4 Summary

The LE derived in section 2.1, its corresponding FPE derived in section 2.2, and the solution method outlined in 2.3 form the basic theoretical framework used for the remainder of this thesis. In Chapter 3 we will extend the method of section 2.1 to derive a GLE for molecular surface diffusion, and use it to study diffusion in a simple model system. In the later chapters we will use the same method to study surface diffusion in a system of experimental interest, dithioanthracene on Cu(111).

# Chapter 3

## Stochastic Model for Surface Diffusion of Molecules

In this chapter we extend the method outlined in the previous chapter to obtain an equation for the center of mass motion of an adsorbed molecule. Following an approach similar to the one used in section 2.1, we derive a GLE for the center of mass coordinate of a molecule, its internal (vibrational and rotational) degrees of freedom giving rise to a memory term and stochastic force. The memory function (or friction coefficient in the Markov approximation) in this GLE has two contributions: one from the surface phonons, and one from molecular degrees of freedom. Although the contribution from the phonons can usually be treated in the Markov approximation, due to the typically shorter time-scale for surface vibrations compared to the motion of adsorbates, internal molecular motion may occur on a time-scale that is not fast compared to center of mass motion. Memory effects can then become important, and we test the accuracy of the Markov approximation below.

After deriving the GLE for center of mass molecular motion, we apply it to study the diffusion of a dimer in one dimension (1D). This simple model is a logical starting point for an application of our stochastic model since it is the simplest possible molecular system, having only one internal degree of freedom. Although simplistic, the 1D dimer model qualitatively captures all of the relevant physics for molecular surface diffusion, namely the coupling of center of mass motion to internal molecular degrees of freedom which may occur on the same time scale as, or slower than, center of mass motion. Physically, the 1D dimer could represent, for example, the diffusion of dimers of W and Re atoms along channels on the W(211) surface [30,31], or could be a simplified model for the diffusion of dimers of larger molecules, such as the dimers of porphyrin molecules observed to diffuse unidirectionally on the Cu(111) surface [6].

An advantage of the simplicity of the 1D dimer model is that the full equations of motion for the molecule (i.e. with the center of mass and vibrational motion both solved for explicitly) can be solved directly, due the low dimensionality of the system. This allows for a systematic test of the accuracy of the stochastic treatment of the internal molecular degrees of freedom, as well as the accuracy of the Markov approximation. Studying diffusion in the 1D dimer will allow us to make some wide-reaching qualitative statements about how internal degrees of freedom can affect surface diffusion in molecules.

## 3.1 Model

To make the derivation of the GLE for molecules simple and transparent we first consider the 1D dimer, and later extend the treatment to an arbitrary molecule. The starting point for our derivation is the set of Markovian Langevin equations for the adsorbed atoms, as derived in Chapter 2. For a dimer consisting of atoms of mass $m_1$, $m_2$ with coordinates $x_1$, $x_2$, the set of Langevin equations (2.21) becomes

$$\begin{aligned} m_1\ddot{x}_1 &= \frac{\partial V}{\partial x_1} - \gamma_{11}\dot{x}_1 - \gamma_{12}\dot{x}_2 + f_1(t) \\ m_2\ddot{x}_2 &= \frac{\partial V}{\partial x_2} - \gamma_{21}\dot{x}_1 - \gamma_{22}\dot{x}_2 + f_2(t). \end{aligned} \tag{3.1}$$

As discussed in Chapter 2, the potential energy $V(x_1, x_2)$ represents the average interaction between the dimer and the surface, while the friction coefficients $\gamma_{ij}$ and stochastic forces $f_i(t)$ account for the phonon-mediated energy exchange with the surface. The stochastic forces $f_1(t), f_2(t)$ have the properties shown in Eq. (2.22),

$$\begin{aligned} \langle f_i(t)\rangle &= 0 \\ \langle f_i(t)f_j(t')\rangle &= 2kT\gamma_{ij}\delta(t-t'). \end{aligned} \tag{3.2}$$

Rewriting Eqs. (3.1) in terms of the center of mass coordinate $r = (m_1x_1 + m_2x_2)/M$ and the relative coordinate $s = x_1 - x_2 - \ell$ (where $\ell$ is the equilibrium dimer length) gives

$$\begin{aligned} M\ddot{r} &= -\frac{\partial V}{\partial r} - \gamma_{rr}\dot{r} - \gamma_{rs}\dot{s} + f_r(t) \\ \mu\ddot{s} &= -\frac{\partial V}{\partial s} - \gamma_{sr}\dot{r} - \gamma_{ss}\dot{s} + f_s(t), \end{aligned} \tag{3.3}$$

where $M = m_1 + m_2$, and $\mu = m_1m_2/(m_1 + m_2)$. The new friction coefficients are given by

$$\begin{aligned}\gamma_{rr} &= \gamma_{11} + \gamma_{12} + \gamma_{21} + \gamma_{22} \\ \gamma_{rs} &= \frac{m_2}{M}\gamma_{11} - \frac{m_1}{M}\gamma_{12} + \frac{m_2}{M}\gamma_{21} - \frac{m_1}{M}\gamma_{22} \\ \gamma_{sr} &= \frac{m_2}{M}\gamma_{11} + \frac{m_2}{M}\gamma_{12} - \frac{m_1}{M}\gamma_{21} - \frac{m_1}{M}\gamma_{22} \\ \gamma_{ss} &= \frac{m_2^2}{M^2}\gamma_{11} - \frac{m_1 m_2}{M^2}\gamma_{12} - \frac{m_1 m_2}{M^2}\gamma_{21} + \frac{m_1^2}{M^2}\gamma_{22}.\end{aligned} \tag{3.4}$$

Note that if the initial matrix of friction coefficients is symmetric, $\gamma_{12} = \gamma_{21}$, then so is the transformed matrix, $\gamma_{rs} = \gamma_{sr}$. We will assume this to be true in the following. The stochastic forces are given by

$$\begin{aligned}f_r(t) &= f_1(t) + f_2(t) \\ f_s(t) &= \frac{m_2}{M}f_1(t) - \frac{m_1}{M}f_2(t),\end{aligned} \tag{3.5}$$

and have the statistical properties given in Eqs. (3.2), now with $i, j \to r, s$.

For a dimer that does not deform strongly in the diffusion process, we can expand the potential $V(r, s)$ to quadratic order in the relative coordinate $s$, giving

$$V(r, s) = V_0(r) + \phi(r)s + \frac{1}{2}\mu\omega^2 s^2, \tag{3.6}$$

with $\phi(r) = \frac{\partial V}{\partial s}|_{s=0}$. The vibration frequency $\omega$ is here assumed to be constant along the diffusion path; in section 3.2.3 we show how a vibration frequency that changes with center of mass position, i.e. $\omega = \omega(r)$, can be accounted for approximately. With the approximation (3.6), the Langevin equations become

$$M\ddot{r} = -V_0'(r) - \gamma_{rr}\dot{r} - \gamma_{rs}\dot{s} - \phi'(r)s + f_r(t) \tag{3.7}$$

$$\mu\ddot{s} + \gamma_{ss}\dot{s} + \mu\omega^2 s = -\phi(r) - \gamma_{sr}\dot{r} + f_s(t), \tag{3.8}$$

where the primes denote differentiation with respect to $r$. We will refer to Eqs. (3.7),(3.8) as the harmonic approximation (HA).

Note that Eq. (3.8) is the equation of motion for a damped, driven harmonic oscillator, and the formal solution can be written as

$$\begin{aligned}s(t) = {}& e^{-\eta t/2}\left(s_0\cos(\Omega t) + \frac{\eta/2 s_0 + \dot{s}_0}{\Omega}\sin(\Omega t)\right) \\ &+ \int_0^t dt'[-\phi[r(t')] - \gamma_{rs}\dot{r}(t') + f_s(t')]e^{-\eta/2(t-t')}\frac{\sin(\Omega(t-t'))}{\Omega\mu},\end{aligned} \tag{3.9}$$

where $\eta = \gamma_{ss}/\mu$, $\Omega = \sqrt{\omega^2 - (\eta/2)^2}$, and $s_0, \dot{s}_0$ are the initial conditions for the relative coordinate. The term involving $\phi[r(t')]$ can be rewritten using integration by parts to give

$$\begin{aligned} s(t) = &-\frac{\phi[r(t)]}{\mu\omega^2} + e^{-\eta t/2}\left([s_0 + \frac{\phi_0}{\mu\omega^2}]\cos(\Omega t) + \frac{\eta/2[s_0 + \frac{\phi_0}{\mu\omega^2}] + \dot{s}_0}{\Omega}\sin(\Omega t)\right) \\ &+ \int_0^t dt'\phi'[r(t')]\frac{e^{-\eta/2(t-t')}}{\mu\omega^2}\left(\cos(\Omega(t-t')) + \frac{\eta}{2\Omega}\sin(\Omega(t-t'))\right)\dot{r}(t') \\ &+ \int_0^t dt'[-\gamma_{rs}\dot{r}(t') + f_s(t')]e^{-\eta/2(t-t')}\frac{\sin(\Omega(t-t'))}{\Omega\mu}. \end{aligned} \tag{3.10}$$

The solution for $\dot{s}(t)$ can be obtained by differentiation, and upon substitution into Eq. (3.7) one obtains a generalized Langevin equation of the form

$$M\ddot{r} = -\frac{dU}{dr} - \int_0^t dt'\Gamma[r(t), r(t'), t-t']\dot{r}(t') + F(t). \tag{3.11}$$

The effective potential $U(r)$ is given by

$$U(r) = V_0(r) - \frac{\phi(r)^2}{2\mu\omega^2}, \tag{3.12}$$

and the memory function and stochastic force have the form $\Gamma = 2\gamma_{rr}\delta(t-t') + \Gamma_{\text{vib}}$ and $F(t) = f_r(t) + F_{\text{vib}}(t)$. The contributions to the memory function and stochastic force from the molecular vibrations are given by

$$\begin{aligned} \Gamma_{\text{vib}}[r(t), r(t'), t-t'] = &\ \phi'[r(t)]\phi'[r(t')]a(t-t') \\ &+ \gamma_{rs}(\phi'[r(t)] + \phi'[r(t')])\dot{a}(t-t') + \gamma_{rs}^2\ddot{a}(t-t') \end{aligned} \tag{3.13}$$

$$\begin{aligned} F_{\text{vib}}(t) = &-(\phi'[r(t)]a(t) + \gamma_{rs}\dot{a}(t))\mu\omega^2\left(s_0 + \frac{\phi_0}{\mu\omega^2}\right) \\ &+ (\phi'[r(t)]\dot{a}(t) + \gamma_{rs}\ddot{a}(t))\mu\dot{s}_0 \qquad , \\ &+ \int_0^t dt'(\phi'[r(t)]\dot{a}(t-t') + \gamma_{rs}\ddot{a}(t-t'))f_s(t') \end{aligned} \tag{3.14}$$

where

$$a(t) = \frac{e^{-\eta t/2}}{\mu\omega^2}[\cos(\Omega t) + \eta/(2\Omega)\sin(\Omega t)], \tag{3.15}$$

and $\dot{a}$ and $\ddot{a}$ are time derivatives of $a$.

Note that the effective potential $U(r)$ is simply the potential energy $V(r,s)$ of Eq. (3.6) evaluated at the dimer length $s$ that minimizes the potential at a given $r$,

$U(r) = V(r, s_0(r))$, where $s_0(r) = -\phi(r)/\omega^2$. Similarly, the memory function can be written in terms of $s_0'(r) = -\phi'(r)/\omega^2$, the slope of the minimum energy path. The vibrational memory function $\Gamma_{\text{vib}}$ will therefore be more significant for systems that follow a curved path through the coordinate space as diffusion proceeds.

The stochastic nature of $F_{\text{vib}}(t)$ comes from the dependence on the initial conditions $s_0$, $\dot{s}_0$, and averages are calculated as averages over these initial conditions with the equilibrium probability density

$$\begin{aligned}\rho(s_0, \dot{s}_0) &= \frac{e^{-E(r_0,s_0,\dot{r}_0,\dot{s}_0)/kT}}{\int ds_0 \int d\dot{s}_0 e^{-E(r_0,s_0,\dot{r}_0,\dot{s}_0)/kT}} \\ &= \frac{\mu\omega}{2\pi kT} e^{-\left(\frac{1}{2}\mu\dot{s}_0^2 + \frac{1}{2}\mu\omega^2(s_0+\phi_0/\mu\omega^2)^2\right)/kT}.\end{aligned} \tag{3.16}$$

Using this probability density, the averages

$$\begin{aligned}\left\langle s_0 + \frac{\phi_0}{\mu\omega^2} \right\rangle &= \langle \dot{s}_0 \rangle = 0 \\ \left\langle \left( s_0 + \frac{\phi_0}{\mu\omega^2} \right)^2 \right\rangle &= \frac{kT}{\mu\omega^2} \\ \langle \dot{s}_0^2 \rangle &= \frac{kT}{\mu}\end{aligned} \tag{3.17}$$

can be used to show that the stochastic force $F(t)$ satisfies the fluctuation-dissipation theorem

$$\begin{aligned}\langle F(t) \rangle &= 0 \\ \langle F(t)F(t') \rangle &= kT\Gamma[r(t), r(t'), |t - t'|].\end{aligned} \tag{3.18}$$

When the memory function decays to zero on a time scale that is fast compared to the time scale for center of mass motion of the dimer, the Markov approximation (MA) for the memory function can be used. In this approximation, $\phi'[r(t')]$ may be replaced with $\phi'[r(t)]$, and the integral term in the generalized Langevin equation becomes

$$\int_0^t dt' \Gamma_{\text{vib}}[r, t-t']\dot{r}(t') \approx \left( \int_0^\infty dt' \Gamma_{\text{vib}}[r, t'] \right) \dot{r}(t) = \gamma_{ss} \left( \frac{1}{\mu\omega^2} \frac{d\phi}{dr} \right)^2 - 2\gamma_{rs} \frac{1}{\mu\omega^2} \frac{d\phi}{dr}. \tag{3.19}$$

The Langevin equation in the MA therefore reads

$$M\ddot{r} = -\frac{dU}{dr} - \gamma_{\text{eff}}\dot{r} + F(t), \tag{3.20}$$

where the effective friction coefficient is $\gamma_{\text{eff}} = \gamma_{rr} + \gamma_{\text{vib}}$, with

$$\gamma_{\text{vib}} = \gamma_{ss}\left(\frac{1}{\mu\omega^2}\frac{d\phi}{dr}\right)^2 - 2\gamma_{rs}\frac{1}{\mu\omega^2}\frac{d\phi}{dr}, \tag{3.21}$$

and the stochastic force satisfies

$$\begin{aligned} \langle F(t)\rangle &= 0 \\ \langle F(t)F(t')\rangle &= 2kT\gamma_{\text{eff}}\delta(t-t'). \end{aligned} \tag{3.22}$$

We now generalize the above approach to a large molecule of many atoms. For a molecule described by the center of mass coordinate $\vec{r}$ and normal mode vibrational coordinates $s_i$, the potential is expanded as in Eq. (3.6),

$$V(\vec{r}, s_i) = V_0(\vec{r}) + \sum_i \left(\phi_i(\vec{r})s_i + \frac{1}{2}\omega_i^2 s_i^2\right), \tag{3.23}$$

with $\phi_i = \frac{\partial V}{\partial s_i}|_{\vec{s}=0}$. Here $\omega_i$ are the normal mode vibration frequencies, calculated with the center of mass held fixed at some reference value. In analogy to Eqs. (3.3), the equations of motion for the molecule become

$$M\ddot{\vec{r}} = -\nabla_{\vec{r}}V_0 - \gamma_{rr}\cdot\dot{\vec{r}} - \sum_i \left(\vec{\gamma}_{ri}\dot{s}_i + \nabla_{\vec{r}}\phi_i(\vec{r})s_i\right) + \vec{f}_r(t) \tag{3.24}$$

$$\ddot{s}_i + \sum_j \gamma_{ij}\dot{s}_j + \omega_i^2 s_i = -\phi_i(\vec{r}) - \vec{\gamma}_{ri}\cdot\dot{\vec{r}} + f_i(t) \tag{3.25}$$

For the case where the off-diagonal damping coefficients $\gamma_{ij}$ vanish for $i \neq j$, the equations of motion for the normal modes decouple and the derivation proceeds exactly as above. The resulting GLE is

$$M\ddot{\vec{r}} = -\nabla_{\vec{r}}U - \int_0^t dt'\Gamma[\vec{r}(t), \vec{r}(t'), t-t']\cdot\dot{\vec{r}}(t') + \vec{F}(t), \tag{3.26}$$

where the effective potential and memory function are simply a sum over terms of the form in Eqs. (3.12) and (3.13), one for each normal mode, i.e. $U(r) = V_0(r) - \sum_i \phi_i(r)^2/2\omega_i^2$, and

$$\begin{aligned} \Gamma_{\text{vib}}[\vec{r}(t), \vec{r}(t'), t-t'] = \sum_i \Big(&\nabla_{\vec{r}}\phi_i[\vec{r}(t)]\nabla_{\vec{r}}\phi_i[\vec{r}(t')]a_i(t-t') + \\ &\left(\nabla_{\vec{r}}\phi_i[\vec{r}(t)]\vec{\gamma}_{ri} + \vec{\gamma}_{ri}\nabla_{\vec{r}}\phi_i[\vec{r}(t')]\right)a_i'(t-t') + \vec{\gamma}_{ri}\vec{\gamma}_{ri}a_i''(t-t')\Big) \end{aligned} \tag{3.27}$$

with a stochastic force $\vec{F}(t)$ that has the required statistical properties shown in Eqs. (3.18). In the MA, the effective friction becomes

$$\gamma_{\text{eff}} = \gamma_{rr} + \sum_i \left( \gamma_{ii} \frac{\nabla\phi_i}{\omega_i^2} \frac{\nabla\phi_i}{\omega_i^2} - \vec{\gamma}_{ri} \frac{\nabla\phi_i}{\omega_i^2} - \frac{\nabla\phi_i}{\omega_i^2} \vec{\gamma}_{ri} \right). \tag{3.28}$$

For general damping, the off-diagonal damping coefficients $\gamma_{ij}$ couple the normal modes together and the derivation of the GLE is more complicated. We carry out this derivation in Appendix B, and show that in the MA the effective friction has a similar form,

$$\gamma_{\text{eff}} = \gamma_{rr} + \sum_{i,j} \gamma_{ij} \frac{\nabla\phi_i}{\omega_i^2} \frac{\nabla\phi_j}{\omega_j^2} - \sum_i \left( \vec{\gamma}_{ri} \frac{\nabla\phi_i}{\omega_i^2} + \frac{\nabla\phi_i}{\omega_i^2} \vec{\gamma}_{ri} \right). \tag{3.29}$$

To calculate properties of a system described by a Langevin equation, one can make use of the corresponding Fokker-Planck equation (FPE) for the probability density $\rho(\vec{x}, \vec{v}, t)$, as discussed in Chapter 2. The FPE corresponding to Eqs. (3.1) is

$$\frac{\partial\rho}{\partial t} = -\vec{v} \cdot \nabla_{\vec{x}}\rho - \vec{F} \cdot M^{-1} \cdot \nabla_{\vec{v}}\rho + \nabla_{\vec{v}} \cdot M^{-1} \cdot \gamma \cdot \left( \vec{v} + kTM^{-1} \cdot \nabla_{\vec{v}} \right) \rho, \tag{3.30}$$

where $\nabla_{\vec{x}}$ and $\nabla_{\vec{v}}$ are gradients with respect to the positions $x_1$ and $x_2$ of the atoms, and their velocities $v_1$ and $v_2$. $\vec{F} = -\nabla_{\vec{x}}V$ is the force and $M$ and $\gamma$ are matrices of the masses and friction coefficients. The FPE (3.30) is mathematically equivalent to the Langevin equations (3.1) and sometimes provides a more convenient way to calculate properties of the system. This is especially true when considering the diffusion coefficient at low temperatures, where the molecule will oscillate around the minimum of the potential for a long time before escaping to a neighboring well. The Langevin equations (3.1) must then be integrated for a prohibitively large number of time steps to describe diffusion.

In the HA, the generalized Langevin equation (3.11) does not correspond to an FPE of the type (3.30), and one must use the FPE corresponding to the coupled equations of motion (3.7),(3.8). The HA therefore does not provide any reduction in computational complexity compared to the exact solution when solving the FPE. On the other hand, in the MA, the Langevin equation (3.20) corresponds to an FPE of the type (3.30) with the vibrational coordinates eliminated. The MA therefore greatly simplifies the calculation for large molecules.

The generalized Langevin equations (3.11),(3.26) along with the expressions for the memory function shown in Eqs. (3.13),(3.27) represent the central result of this chapter. In the next section, we will test the accuracy of this approach by comparing the numerical solution of Eq. (3.11) to that of the full equations of motion, Eqs. (3.1). We will also check the accuracy of the MA, Eq. (3.20), to determine the importance of memory effects.

### 3.2 Results

We now apply the model outlined above to study the diffusion of a dimer consisting of two identical atoms bound by a harmonic force of frequency $\omega$. For the potential we take a cosine with a barrier of height $V_b$. We then have the following parameters for Eqs. (3.1)

$$\begin{aligned}
&m_1 = m_2 = m, \\
&\gamma_{11} = \gamma_{22} = \gamma, \quad \gamma_{12} = \gamma_{21} = 0, \\
&V(x_1, x_2) = \tfrac{1}{2} V_b \cos(2\pi x_1/a) + \tfrac{1}{2} V_b \cos(2\pi x_2/a) + \tfrac{1}{2}\mu\omega^2(|x_1 - x_2| - \ell)^2,
\end{aligned} \tag{3.31}$$

which gives

$$\begin{aligned}
&M = 2m, \quad \mu = m/2 \\
&\gamma_{rr} = 2\gamma, \quad \gamma_{ss} = \gamma/2 \quad \gamma_{rs} = \gamma_{sr} = 0 \\
&V_0(r) = V_b \cos(\pi\ell/a)\cos(2\pi r/a), \quad \phi(r) = -\pi/a V_b \sin(\pi\ell/a)\cos(2\pi r/a).
\end{aligned} \tag{3.32}$$

To assess the accuracy of the stochastic treatment of the internal molecular vibrations derived in section 3.1, we will now compare three different solutions:

1. Eqs. (3.3), the two-dimensional equations of motion for the dimer.
2. Eq. (3.11), the one-dimensional generalized Langevin equation, with non-Markovian friction term arising from the influence of the vibrational motion of the dimer.
3. Eq. (3.20), the Markovian approximation to Eq. (3.11).

To compare the three solutions, we calculate the center of mass diffusion coefficient, defined as

$$D = \lim_{t\to\infty} \frac{\langle (r(t) - r(0))^2 \rangle}{2t}, \tag{3.33}$$

by making use of the appropriate FPE for each of the three cases. We solve the FPE by the matrix continued fraction method [24], and obtain $D$ by making use of its relationship to the velocity autocorrelation function

$$D = \int_0^\infty dt \, \langle \dot{r}(t)\dot{r}(0)\rangle \, . \tag{3.34}$$

In the calculations that follow, we scale all lengths by $\frac{a}{2\pi}$, masses by $m$ and times by $\frac{a}{2\pi}\sqrt{\frac{m}{V_b}}$. The results are presented in the following scaled variables

$$\bar{\ell} = \frac{2\pi}{a}\ell, \quad \bar{\omega} = \frac{a}{2\pi}\sqrt{\frac{m}{V_b}}\omega, \quad \bar{\gamma} = \frac{a}{2\pi}\frac{1}{\sqrt{mV_b}}\gamma, \quad \bar{D} = \frac{2\pi}{a}\sqrt{\frac{m}{V_b}}D, \quad \bar{V} = \frac{V}{V_b} \tag{3.35}$$

### 3.2.1 Harmonic Approximation

Figs. 3.1, 3.2, and 3.3 show the diffusion coefficient calculated in the low, moderate and high friction regimes for different values of the equilibrium dimer length $\bar{\ell}$. It can been seen from the three figures that both the HA and MA approach the exact calculation as the dimer vibration frequency $\bar{\omega}$ is increased. This is expected, since when the internal force in the dimer is strong compared to the interaction with the surface, the dimer will be held close to its equilibrium length, and the anharmonic contributions to the restoring force (due to the cosine term in the potential $V(r,s)$) will not be important. In this stiff dimer limit, the vibrational motion will also occur on a time scale much faster than the center of mass motion, so motion in the two coordinates should be mostly decoupled. In particular, the HA is expected to be accurate when $\bar{\omega}$ is large compared to the characteristic vibration frequency of the interaction potential, defined by

$$\bar{\omega}_0^2 = 2\left.\frac{\partial^2 \bar{V}}{\partial \bar{s}^2}\right|_{\bar{s}=0} = -\frac{1}{2}\cos(\bar{r})\cos(\bar{\ell}/2). \tag{3.36}$$

The frequency $\bar{\omega_0}$ is largest for a dimer that is commensurate with the lattice spacing of the surface, $\bar{\ell} = 2\pi$, where it has a maximum value of $\bar{\omega_0} = 1/\sqrt{2}$, and smallest for an incommensurate dimer, $\bar{\ell} = \pi$ where it goes to zero. Physically, this occurs because for a commensurate dimer the forces on the two atoms are equal, while for an incommensurate dimer, the forces point in opposite directions and therefore cancel each other and give no center of mass force. The HA should therefore be expected to be accurate to lower dimer frequency $\bar{\omega}$ for an incommensurate dimer. This can be seen in Fig. 3.1 for the incommensurate dimer, where the diffusion coefficient in the HA has the correct qualitative trend at low $\bar{\omega}$, while in Fig. 3.2 with the intermediate dimer length $\bar{\ell} = 1.6\pi$, the HA gives the wrong trend at low $\bar{\omega}$. For the exactly commensurate dimer shown in Fig. 3.3, the function $\phi(r)$ goes to zero, and the motion in the $r$ and $s$ coordinates is completely uncoupled in the HA. The diffusion coefficient is therefore independent of the frequency $\bar{\omega}$.

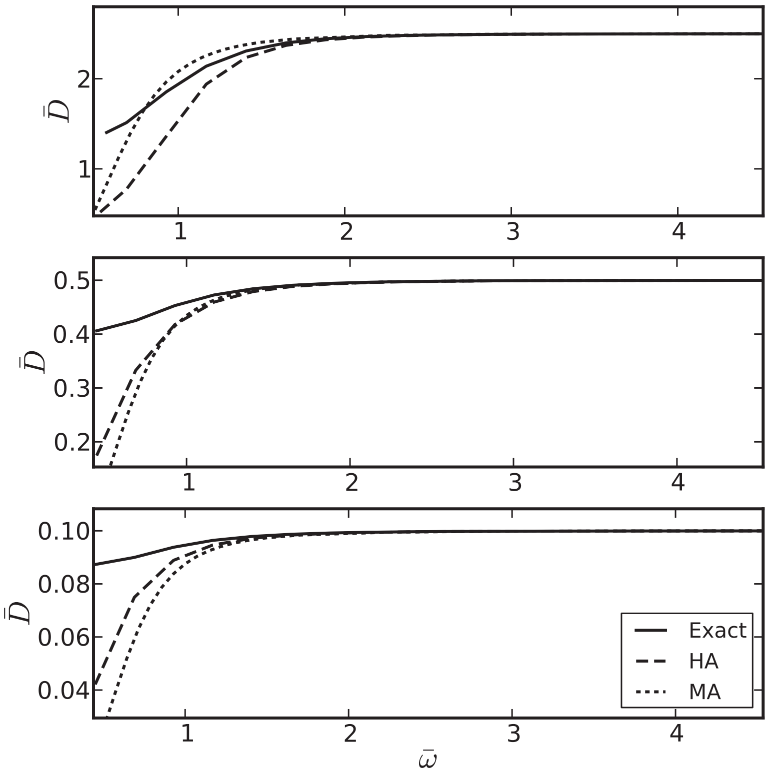

Figure 3.1: Comparison of the exact diffusion coefficient to the HA and MA as a function of dimer vibration frequency $\bar{\omega}$ for an incommensurate dimer ($\bar{\ell} = \pi$) at temperature $kT/V_b = 1.0$. The three panels, from top to bottom, are for low friction ($\bar{\gamma} = 0.2$), moderate friction ($\bar{\gamma} = 1.0$), and high friction ($\bar{\gamma} = 5.0$).

At the low temperatures that are experimentally relevant for surface diffusion, the diffusion coefficient has the Arrhenius form,

$$D = D_0 e^{-\Delta E/kT}, \tag{3.37}$$

where $\Delta E$ is the potential energy barrier over which the molecule must escape, and $D_0$

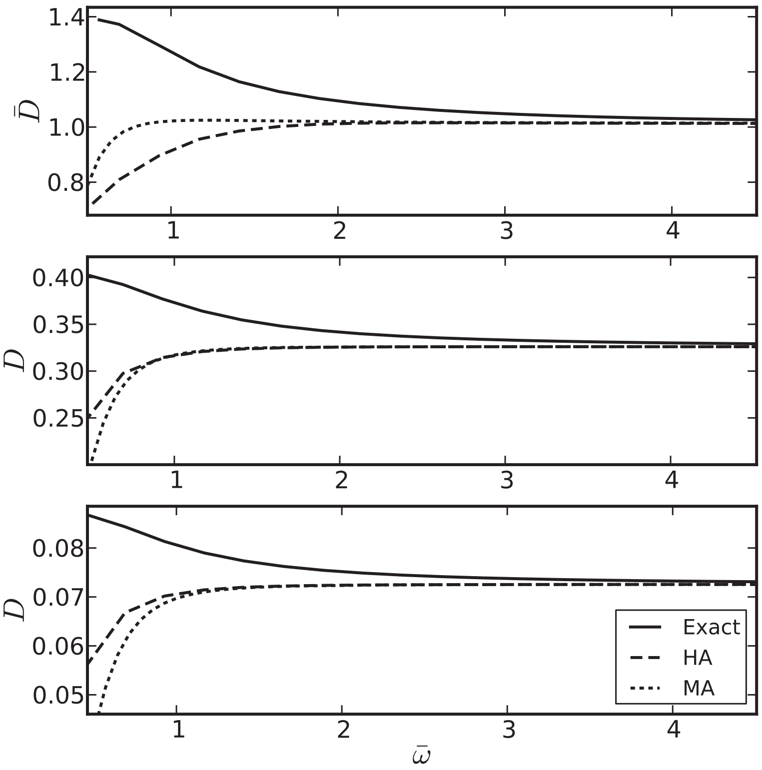

Figure 3.2: Same as Fig. 3.1, but for a dimer of intermediate length ($\bar{\ell} = 1.6\pi$).

is a prefactor that is independent of temperature. When comparing the diffusion of the dimer to that of a monomer, both the energy barrier and prefactor can be affected. For example, the energy barrier for a commensurate dimer will be approximately twice that for a monomer, while the barrier for an incommensurate dimer can be smaller than the monomer barrier. The prefactor for the dimer will depend on the detail of the dynamics of the molecular vibrations. In order to separate these effects, we will calculate the prefactor and barrier, comparing the exact solution to the HA and MA. First, though, we consider the accuracy of the MA compared to the HA in order to gauge the importance of the memory effects in the generalized Langevin equation (3.11).

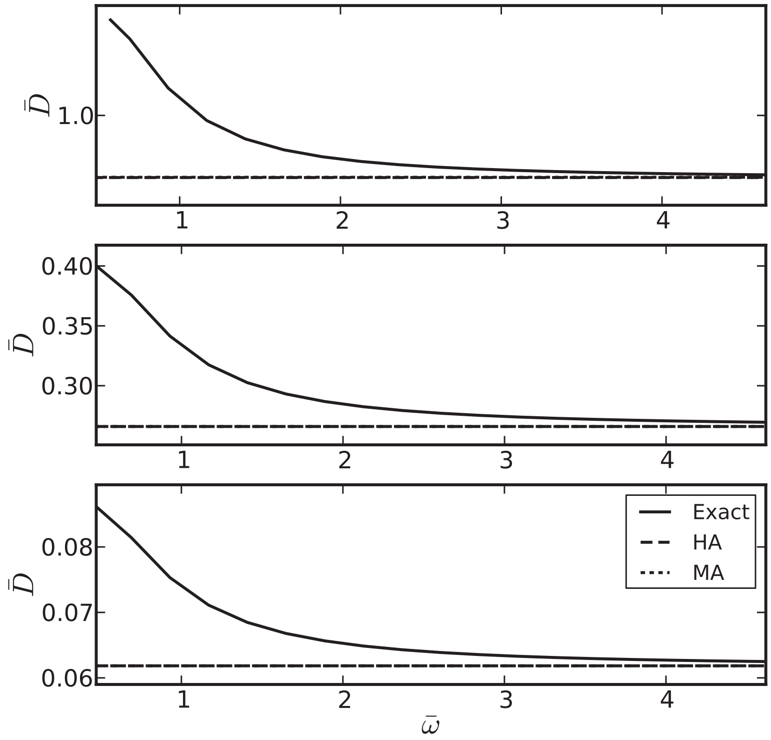

Figure 3.3: Same as Fig. 3.1, but for a commensurate dimer length $\bar{\ell} = 2\pi$. In all three panels, the MA and HA curves are indistinguishable.

### 3.2.2 Markov Approximation

From Figs. 3.1, 3.2, and 3.3 it can be seen that the MA provides a reasonable approximation to the solution of the generalized Langevin equation (3.11) for all cases tested. The accuracy is best when both the friction $\bar{\gamma}$ and frequency $\bar{\omega}$ become large. This can be understood by looking at the expression (3.13) for the memory function that appears in the generalized Langevin equation. In the high frequency limit $\bar{\omega} \to \infty$ the vibrational part of the memory function $\Gamma_{\text{vib}}$ becomes negligible, since the functions $a(t)$ and $\dot{a}(t)$ are inversely proportional to $\bar{\omega}$, and $\ddot{a}(t)$ becomes proportional to $1/\omega$ upon integration. In this limit, the vibrational motion of the molecule has no effect on the center of mass motion, and the molecule can simply be treated as a rigid body.

When $\bar{\gamma}$ (and therefore $\bar{\eta}$) becomes large, the exponential term in $a(t)$ quickly decays to zero (see Eq. (3.15)), and the MA is accurate. However, when $\bar{\gamma}$ becomes large compared to $\bar{\omega}$ (i.e. the overdamped case), the effective frequency $\bar{\Omega} = \sqrt{(\bar{\eta}/2)^2 - \bar{\omega}^2}$

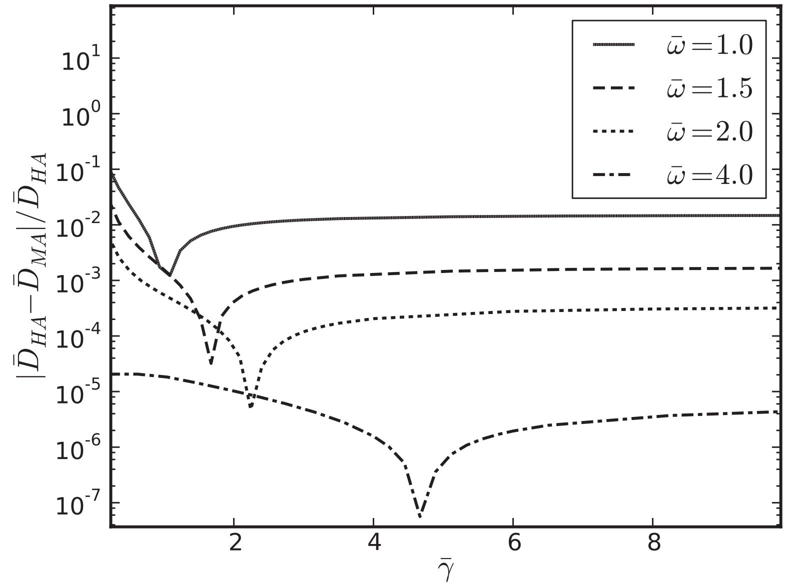

Figure 3.4: Relative error in the MA (compared to the HA), for a dimer of length $\bar{\ell} = 1.6\pi$ at temperature $kT/V_b$=1.0.

becomes imaginary. In this case, the sin and cos terms in $a(t)$ are replaced by hyperbolic functions and $\bar{\Omega}$ is replaced by $\bar{\Omega}' = \sqrt{(\bar{\eta}/2)^2 - \bar{\omega}^2}$. The memory function will then contain a slowly decaying term proportional to $e^{-((\bar{\eta}/2)^2 - \bar{\Omega}'^2)t} \approx e^{-\bar{\omega}^2/\bar{\eta}t}$. We therefore expect the MA to be accurate in the regime

$$\bar{\omega}_0 \ll \bar{\gamma} \lesssim \bar{\omega}. \tag{3.38}$$

This trend can be seen in Fig. 3.4, where the relative error in the MA is shown (note the cusp seen in each plot where the error in the MA goes to zero as it changes sign).

The worst error in the MA seen in Figs. 3.1 and 3.2 is in the low friction regime, for small vibration frequency. In this regime, the MA seems to consistently overestimate the diffusion coefficient. The diffusion coefficient is also slightly underestimated in the high friction regime at low frequency. This can be understood qualitatively in the following way. The Grote-Hynes formula gives an approximation to the escape rate over a potential barrier in a system described by a generalized Langevin equation of the type (3.11) [27]. The escape rate depends on the Laplace transform of the memory function $\hat{\Gamma}(z)$ at a frequency of the order of the vibration frequency $\bar{\omega}_0$ in the barrier region, determined by solving the equation $z^2 + z\hat{\Gamma}(z) = \bar{\omega}_0^2$. In contrast,

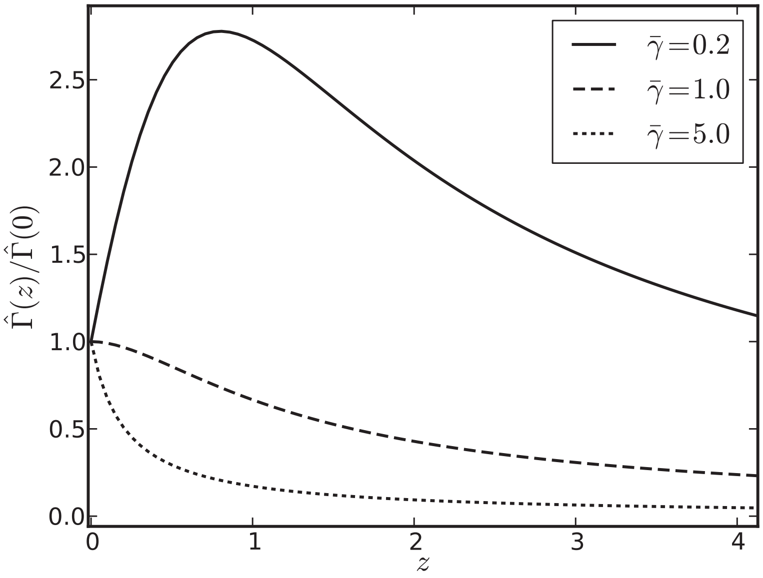

Figure 3.5: Ratio of the Laplace transform of the memory function, as shown in Eq. (3.39), to its zero-frequency value for $\bar{\omega} = 1.0$.

the MA uses the zero-frequency (time integrated) value $\hat{\Gamma}(0)$.

The Laplace transform of the memory function (3.13) can be calculated approximately by holding the coordinate $r$ constant,

$$\begin{aligned}\hat{\Gamma}_{\text{vib}}(z) &= \int_0^\infty dt e^{-zt}\Gamma_{\text{vib}}(r,t) \\ &= \frac{1}{(z+\eta/2)^2+\Omega^2} \\ &\times \left(\frac{\phi'(r)^2}{\mu\omega^2}(z+\eta) - 2\frac{\gamma_{rs}}{\eta}\frac{\phi'(r)}{\mu\Omega} - \frac{\gamma_{rs}^2}{\mu}z\right)\end{aligned} \tag{3.39}$$

The Laplace transform evaluated at $\bar{\omega} = 1$ is plotted in Fig. 3.5 for the same values of the friction used in Figs. 3.1, 3.2, and 3.3. It is clear that at small $\bar{\gamma}$, $\hat{\Gamma}_{\text{vib}}(z)$ quickly increases from its $z = 0$ value, resulting in an underestimation of the effective friction in the MA and therefore an overestimation of the diffusion coefficient. On the other hand, at large $\bar{\gamma}$, $\hat{\Gamma}_{\text{vib}}(z)$ decreases from its $z = 0$ value, resulting in an overestimation of the effective friction and an underestimation of the diffusion coefficient. For a given $\bar{\omega}$, the MA will be most accurate when the friction $\bar{\gamma}$ is close to $\bar{\omega}$, i.e. when the vibrations are close to being critically damped. When the vibrations are underdamped or overdamped, the MA will overestimate or underestimate the diffusion coefficient, respectively. Note, however, that for vibration frequencies $\bar{\omega} \gtrsim 1$, the error in $\bar{D}$ is at worst around 10%. It therefore seems that the friction coefficient $\bar{\gamma}$ would need to be either very large or very small for the error in the MA to be significant, so long as the molecular vibrations occur on a time scale approximately the same as, or faster than the center of mass motion.

### 3.2.3 Energy Barrier and Prefactor

An example of an Arrhenius plot is shown in Fig. 3.6. It can be seen that at low temperatures, the plot approaches the straight line expected for the Arrhenius form shown in Eq. (3.37). The energy barrier and prefactor are calculated by differentiation of $\ln(\bar{D})$ with respect to the (scaled) inverse temperature $\beta = V_b/kT$, and thus become temperature dependent, i.e.

$$\Delta\bar{E}(T) = -\frac{d\ln(\bar{D})}{d\beta}, \qquad \bar{D}_0(T) = \bar{D}e^{\beta\Delta\bar{E}}. \tag{3.40}$$

In the regime $\Delta\bar{E} \gg 1/\beta$ where thermally activated diffusion is observed, the prefactor and barrier should approach constant values. Fig. 3.7 shows the differential prefactor and barrier for the system shown in Fig. 3.6. It can be seen that the prefactor and barrier both approach their constant low temperature limit at around $V_b/kT \gtrsim 10$. Note also the pronounced compensation effect seen in many thermally activated processes [32]. It is this low-temperature limit that we are interested in, as surface diffusion experiments typically have energy barriers in the range $V_b/kT = 20 \sim 30$ [5,6,33]. We now consider in detail the energy barrier and prefactor for the cases of a dimer whose length is incommensurate with the lattice constant of the surface, and one whose length is commensurate.

#### Incommensurate Dimer

Fig. 3.8 shows the energy barrier and prefactor for the incommensurate dimer with $\bar{\ell} = \pi$. Both the HA and MA provide a good approximation to the prefactor and barrier down to frequencies of $\omega \approx 1$. Interestingly, the HA gives an accurate calculation of the prefactor even down to low frequencies of $\omega \approx 0.2$, where it would not necessarily be expected to be accurate. At very low frequencies, there is a turnover and subsequent decrease of the prefactor in the MA calculation.

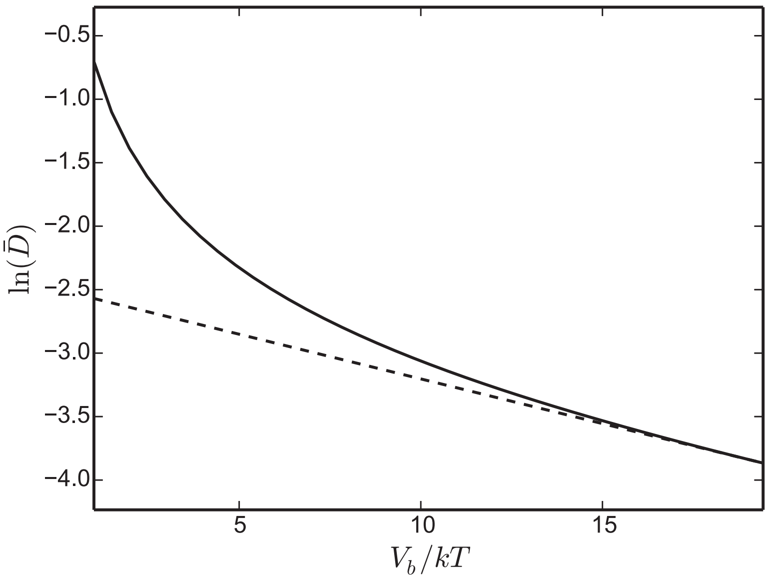

Figure 3.6: Arrhenius plot for the MA solution with $\bar{\omega} = 2.0$, $\bar{\ell} = \pi$, $\bar{\gamma} = 1.0$. The dashed line shows the Arrhenius fit $\bar{D} = \bar{D}_0 e^{-\beta \Delta \bar{E}}$ in the low temperature limit, with $\Delta \bar{E} = 0.70$ and $\bar{D}_0 = 0.82$.

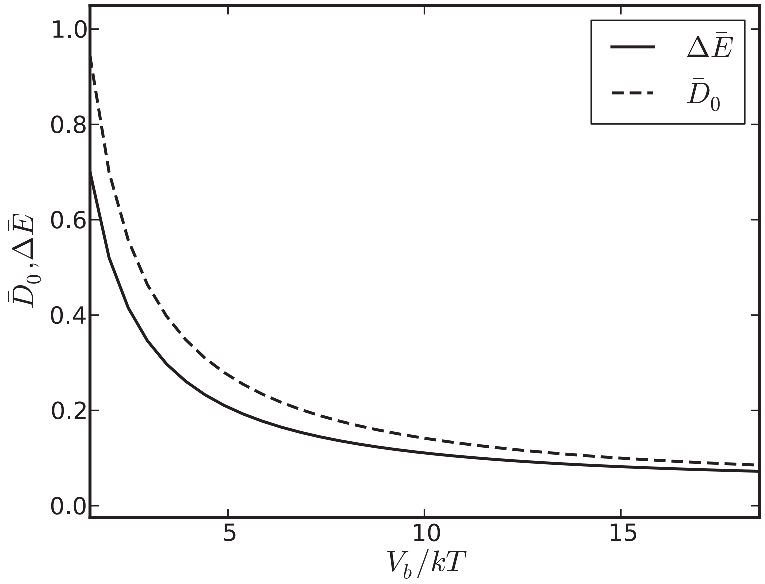

Figure 3.7: Differential prefactor and barrier calculated from the data shown in Fig. 3.6.

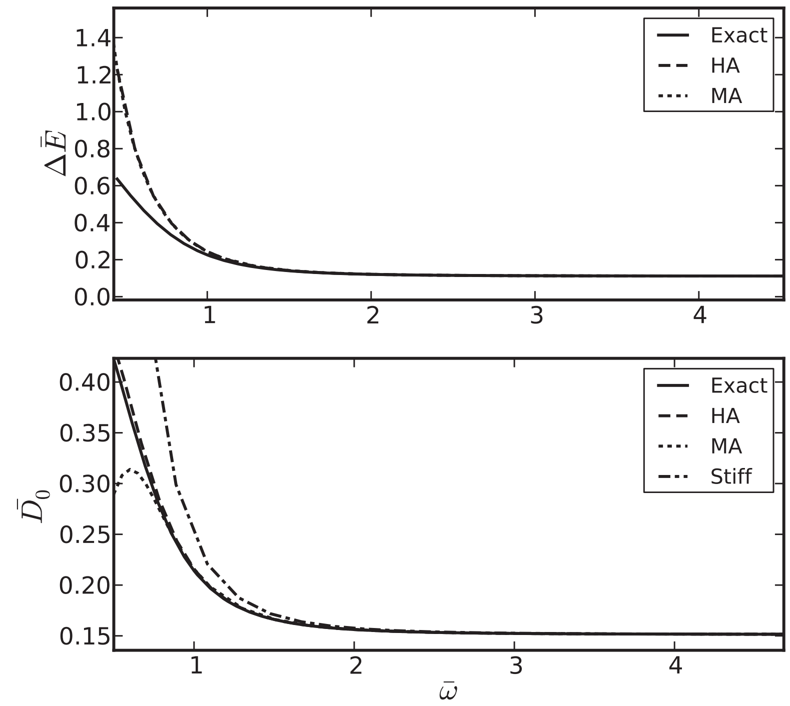

Figure 3.8: Energy barrier and prefactor for an incommensurate dimer ($\bar{\ell} = \pi$) as a function of dimer vibration frequency $\bar{\omega}$, for a friction coefficient of $\bar{\gamma} = 1.0$ and temperature $V_b/kT = 9.0$. In the upper panel, the HA and MA curves lie on top of one another.

To understand the behavior of the HA and MA calculations of the prefactor, consider the expression for the effective friction, Eq. (3.21). The additional friction term due to the internal vibrations depends on the function $\phi(r)$, defined through the expansion of the potential,

$$V(r,s) = V_0(r) + \phi(r)s + \frac{1}{2}\mu\omega^2 s^2 = U(r) + \frac{1}{2}\mu\omega^2 \left(s + \frac{\phi(r)}{\mu\omega^2}\right)^2. \tag{3.41}$$

In the present calculation with $\gamma_{rs} = 0$, the effective friction can therefore be written as

$$\gamma = \gamma_{rr} + \gamma_{ss} \left(\frac{ds_0}{dr}\right)^2, \tag{3.42}$$

where $s_0(r) = -\phi(r)/(\mu\omega^2)$ is the value of the internal coordinate $s$ along the minimum energy path. The effect of the internal vibrations of the dimer on the center of mass motion is to increase the friction, and Eq. (3.42) makes it clear that the increase in the friction is due to the dimer following a curved path through the coordinate space as it crosses the energy barrier.

Intuitively it makes sense that a curved path would lead to a higher effective friction for motion in the center of mass coordinate. As the dimer approaches the transition state, energy will be dissipated as it moves in the center of mass coordinate, due to the friction force. If it must also move in the relative coordinate there will be additional energy dissipated since there is also friction in this coordinate, so that the amount of energy dissipated for a given amount of motion in the center of mass coordinate is higher, resulting in a higher effective friction coefficient. Stated more simply, the effective distance the dimer needs to travel to cross the barrier is longer for a curved path, and so more energy will be dissipated along the path, which is equivalent to a higher friction coefficient.

Fig. 3.8 also shows, for comparison, the diffusion prefactor calculated without the additional friction term shown in (3.42). In this stiff dimer approximation, the effects of the vibrations on the center of mass motion are ignored, and the dimer is treated as a rigid body. It can be seen that the effect of the higher friction is to lower the prefactor, as expected (the barrier is unaffected). This lowering of the diffusion coefficient for systems that follow curved paths has been observed before [34], where it was attributed to the suppression of long jumps at low friction. Here the suppression of long jumps, and subsequent lowering of the diffusion prefactor, is described in a straightforward way by an increase in the effective friction coefficient according to the simple formula (3.42). In this case the lowering of the diffusion prefactor also occurs in the moderate and high friction regimes, where long jumps do not occur. We also note that the term proportional to $\gamma_{rs}$ in Eq. (3.21) can be negative, which can result in a lower effective friction for systems with off-diagonal friction components.

As seen in Fig. 3.8, in the regime where the MA is accurate, the correction to the prefactor provided by the additional friction term is relatively modest, becoming large only in the small $\bar{\omega}$ region, where the MA begins to diverge from the exact solution. The reason for this deviation as small $\bar{\omega}$ can be seen in Eq. (3.42). The additional friction term becomes significant only when the minimum energy path has a reasonably large curvature (i.e. the dimer length changes significantly as it moves across the surface). However, the harmonic approximation for the potential energy requires that the dimer only make small deviations from its equilibrium length.

A more significant correction to the prefactor would be seen for a molecule with several vibrational modes. For a molecule with $N$ vibrational modes, the effective friction is given by Eq. (3.28). Assuming, for simplicity, that $\omega_i$, $\gamma_{ii}$ and $\phi_i$ are the same for all modes, the effective friction for a molecule diffusing in one dimension becomes

$$\gamma_{\text{eff}} = \gamma_{rr} + N\gamma_{ss}\left(\frac{ds_o}{dr}\right)^2. \tag{3.43}$$

The more vibrational modes the molecule has, the higher the effective friction, and the greater the effect on the prefactor.

To show the effect of this increase in effective friction we calculate the prefactor with an increasing number of modes, while keeping the effective potential $U(r)$ the same. In Fig. 3.9 we show the ratio of the prefactor calculated for $N$ vibrational modes, $\bar{D}_0^{(N)}$ to the prefactor calculated in the stiff dimer approximation, $\bar{D}_0^{(0)}$. It can be seen that the lowering of the prefactor due to the higher effective friction becomes more significant as the number of vibrational modes increases. For example, with 10 vibrational modes, there is an order of magnitude change in the prefactor when $\bar{\omega} \approx 0.65$.

The effective friction term in Eq. (3.42) could also provide a significant correction to the prefactor in any system that follows a significantly curved path as diffusion proceeds. Some examples are diffusion of an atom on the bcc(110) surface studied in Ref. [34], or a molecule that rotates as it diffuses, as seen for dithioanthrancene adsorbed on a copper surface [5].

### Commensurate Dimer

Fig. 3.10 shows the energy barrier and prefactor for a commensurate dimer with $\bar{\ell} = \bar{a} = 2\pi$. The most distinctive feature in the graph of the prefactor is the peak that occurs around $\bar{\omega} = 0.7$, which both the HA and MA fail to reproduce. This peak is related to a flattening of the potential energy surface in the direction of the $s$-coordinate around the transition state as the frequency $\bar{\omega}$ decreases. To see this, consider the potential energy, given by

$$\bar{V}(\bar{r}, \bar{s}) = \cos(\bar{r})\cos(\bar{s}/2) + \frac{1}{4}\bar{\omega}^2\bar{s}^2. \tag{3.44}$$

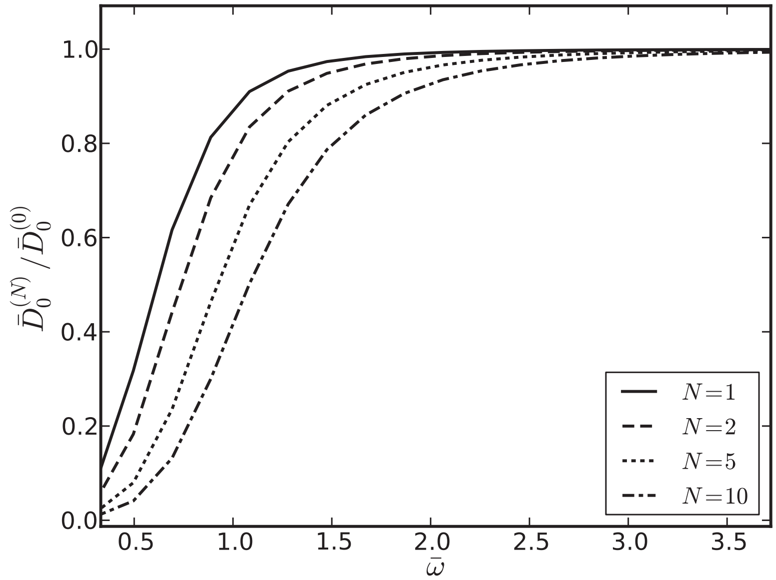

Figure 3.9: Ratio of prefactor calculated for $N$ vibrational modes, $\bar{D}_0^{(N)}$, to prefactor calculated in the stiff dimer approximation, $\bar{D}_0^{(0)}$, for a friction coefficient of $\bar{\gamma} = 1.0$ and temperature $V_b/kT = 9.0$.

At large $\bar{\omega}$, the transition state occurs at $\bar{r} = 0, \bar{s} = 0$, and the frequency in the $\bar{s}$ coordinate is

$$\bar{\omega}_t^2 = 2\frac{\partial^2 \bar{V}}{\partial \bar{s}^2} = \bar{\omega}^2 - \frac{1}{2}. \tag{3.45}$$

When $\bar{\omega}^2 \to 1/2$, the frequency goes to zero and then becomes imaginary, as the transition state at $\bar{r} = 0, \bar{s} = 0$ becomes a local maximum. When $\bar{\omega}^2 \approx 1/2$, the potential surface around the transition state is then very flat in the $s$-direction, which makes it easier for the dimer to cross the barrier, and therefore raises the prefactor. In the transition state theory (TST) this is seen as an entropy effect. The escape rate in TST is given by

$$\nu_{\text{TST}} = \frac{kT}{h}\frac{Z_{\text{vib}}^{(b)}}{Z_{\text{vib}}^{(m)}} e^{-\Delta V/kT} = \frac{kT}{h} e^{\Delta S/k} e^{-\Delta V/kT}, \tag{3.46}$$

where $\Delta S$ is the change in entropy between the minimum and transition state. In the harmonic approximation, this becomes for a dimer

$$\nu_{\text{TST}} = \frac{\omega_m^{(1)}\omega_m^{(2)}}{2\pi\omega_t} e^{-\Delta V/kT}, \tag{3.47}$$

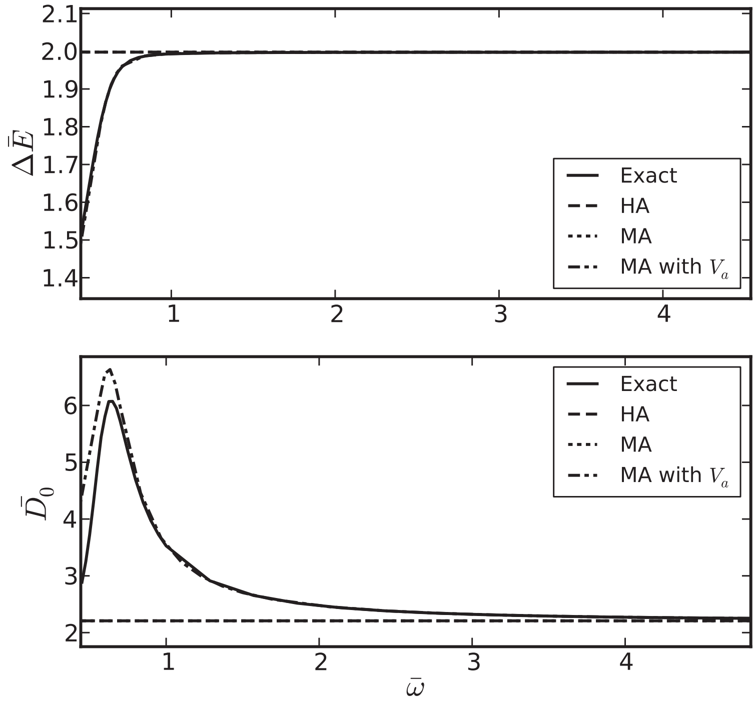

Figure 3.10: Energy barrier and prefactor for a commensurate dimer ($\bar{\ell} = 2\pi$) as a function of dimer vibration frequency $\bar{\omega}$, for a friction coefficient of $\bar{\gamma} = 1.0$ and temperature $V_b/kT = 9.0$. In the upper panel the HA and MA curves lie on top of one another, as do the Exact and MA with $V_a$ curves. In the lower panel the HA and MA curves lie on top of one another.

where $\omega_m^{(1)}$, $\omega_m^{(2)}$ are the normal mode frequencies at the minimum and $\omega_t$ is the non-imaginary frequency at the transition state. It can be seen that when the frequency at the barrier, $\omega_t$ becomes small, the entropy factor becomes large. This explains the peak in the prefactor around $\bar{\omega} = 1$. The HA and MA both make the assumption that the frequency in the $s$-coordinate stays constant at $\bar{\omega}$ at all points on the potential surface, and so they cannot capture this entropy effect.

We can take the change in curvature into account in the MA by replacing the effective potential $U(r)$ by the adiabatic potential $V_a(r)$, defined (in scaled units) by

$$\exp(-\beta \bar{V}_a(\bar{r})) = \int d\bar{s} \exp(-\beta \bar{V}(\bar{r}, \bar{s})). \tag{3.48}$$

Note that the effective potential $U(r)$, given in Eq. (3.12), is simply the adiabatic potential evaluated in the harmonic approximation with constant frequency $\bar{\omega}$, Eq. (3.6).

We can instead evaluate $V_a(r)$ using the full potential $V(r, s)$, which will take into account the change in entropy between the minimum and transition state.

The prefactor and barrier resulting from the MA using $V_a(r)$ calculated in this way are shown in Fig. 3.10. It is seen that calculation of the prefactor is much more accurate using this approach, and the peak around $\bar{\omega} = 1.2$ is reproduced. The barrier is also quite accurate (it is indistinguishable from the exact calculation in Fig. 3.10).

For a dimer with a vibration frequency $\bar{\omega} \approx 1/\sqrt{2}$, the diffusion prefactor for the dimer can increase above the value for the monomer of $\bar{D}_0^{(M)} \approx 2.1$ (which can be found by repeating the Arrhenius analysis for a single atom adsorbed in the cosine potential). This effect was observed experimentally for the diffusion of porphyrin monomers and dimers on a copper surface [6]. The present analysis shows that this enhancement of the prefactor for dimers can be understood as the result of an entropy difference between the minimum and transition state that occurs when there is a particular matching between the strength of the forces holding the dimer together and the forces between the dimer and the surface. When the frequency is large, $\bar{\omega} \gg 1/\sqrt{2}$, the dimer makes jumps from site to site as a unit, while for small frequencies $\bar{\omega} \ll 1/\sqrt{2}$, the diffusion proceeds by one atom jumping to the neighboring site first, followed by the other. When the forces are matched such that both types of diffusion are equally likely to occur, there is a large entropy difference and resultant increase of the diffusion prefactor. The fact that the increase in the prefactor seen here is much smaller than the two orders of magnitude seen in Ref. [6] can be rationalized by the fact that the simple model system studied here only has one vibrational degree of freedom, whereas the porphyrin monomers and dimers have many. The combined effect of changes in all of the vibration frequencies near the barrier will increase the entropy difference.

The effects of such entropy barriers have been seen before, e.g. in stochastic models for diffusion [35], as well as a reaction rate model where the width of a bottleneck region fluctuates according to a Langevin equation [36].

### Intermediate Dimer Length

For a dimer of intermediate length, both the effects of the entropy difference and the higher effective friction due to a curved diffusion path can be seen. Fig. 3.11 shows the prefactor for a dimer of length $\bar{\ell} = 1.6\pi$. Note that the decrease of the prefactor at low $\bar{\omega}$, due to the increasingly curved diffusion path, is properly described by the HA and MA, but they again fail to reproduce the increase in the prefactor resulting from the entropy difference.

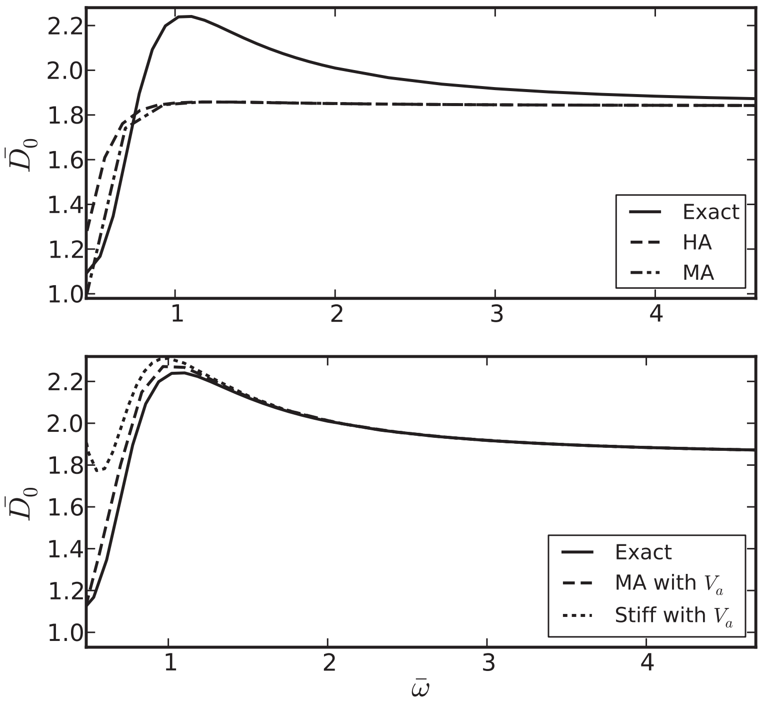

Figure 3.11: Prefactor for a dimer of intermediate length ($\bar{\ell} = 1.6\pi$) as a function of dimer vibration frequency $\bar{\omega}$,for a friction coefficient of $\bar{\gamma} = 1.0$ and temperature $V_b/kT = 9.0$.

Fig. 3.11 also shows the prefactor calculated using the adiabatic potential, Eq. (3.48), and again it is seen that the increase in the prefactor due to the entropy difference is accurately reproduced. To show the influence of the effective friction term at small $\bar{\omega}$, the prefactor calculated in the stiff dimer approximation using the adiabatic potential is also shown. It can be seen that while the MA remains accurate even at small $\bar{\omega}$, the stiff dimer approximation diverges from the exact calculation. This demonstrates that by combining the formula (3.42) for the effective friction coefficient with an accurate calculation of the adiabatic potential, our stochastic model can account for both entropy effects and the effect of the curvature of the diffusion path.

## 3.3 Conclusions

We can summarize the differences between the diffusion of a monomer and a dimer as being of three types:

1. The energy barrier for the dimer will be different from that of the monomer, and will depend mainly on the mismatch between the dimer length and the lattice constant of the surface. A dimer with a length that is commensurate with the surface will have a larger energy barrier than a monomer, and an incommensurate dimer will have a smaller barrier.

2. The diffusion prefactor for the dimer can be affected by the presence of an entropy difference between the minimum and transition state. This occurs when the potential becomes flatter or more steep at the transition state in the vibrational coordinate.

3. The diffusion prefactor can also be affected when the lowest energy path across the potential surface is significantly curved. In the system studied here, this has the effect of lowering the prefactor for incommensurate dimers. In general, when the direction of easy crossing at the transition state does not lie on a straight line between the minima the prefactor will be affected.

Effective 1D models for dimer diffusion have been described before [37, 38], and these models can capture the effects 1 and 2. The advantage of the present approach is that it can also account for 3, the lowering of the prefactor due to a curved diffusion path. In the MA, the effect on the prefactor is captured in an effective friction term that is given by the simple formula (3.42) involving the slope of the lowest energy path across the potential surface.

The above results show that the approach outlined in Section 3.1 is applicable as long as the molecular vibration frequencies are approximately the same order of magnitude or larger than the vibration frequencies associated with the molecule-surface interaction. This is typically true for, e.g., organic molecules adsorbed on metal surfaces, where the molecule-surface interactions are weak compared to the intramolecular forces.

It was also seen that when this requirement is satisfied, the system is usually well described by the Markov approximation. When there is a large mismatch between the friction and the vibration frequencies (i.e. the molecular vibrations are either strongly overdamped or underdamped), the non-Markovian nature of the memory function can become important.

Although we have here studied dimer diffusion, the same approach can be applied to any system that undergoes diffusive motion in one or more coordinates and vibrational motion in other coordinates. In the remainder of this thesis we will apply this model to the diffusion of dithioanthrancene on the Cu(111) surface, a system which shows unidirectional diffusion and is therefore amenable to the approach used in this chapter.

# Chapter 4

# Density Functional Theory Calculations

In order to apply the stochastic model of surface diffusion outlined in the previous chapters to physical systems of interest, it is necessary to calculate the energetics of the systems. To this end, we perform ab initio calculations of the energy and vibration frequencies for 9,10-dithioanthracene (DTA) adsorbed on a Cu(111) surface. The surface diffusion of organic molecules adsorbed on metal substrates, such as DTA on Cu(111) can be observed by scanning tunnelling microscopy (STM) [5]. After the molecules are deposited on the metal surface, a series of STM images with molecular resolution can be used to observe the formation of supra-molecular structures, as well as follow the diffusion of individual molecules at low coverage. An example of such STM images for DTA on Cu(111) is shown in Fig. 4.1

DTA undergoes unidirectional surface diffusion on the Cu(111) surface, and is therefore amenable to the one dimensional diffusion model studied in the previous chapter. Interestingly, the direction of fast diffusion for DTA on Cu(111) is determined by the details of the molecule-surface interaction, rather than asymmetry of the surface (e.g. diffusion along a step edge). The DTA molecules can diffuse along any of the three equivalent close-packed directions on the Cu(111) surface, depending on which orientation they land on the surface with. The quasi-one dimensional diffusion, and availability of experimental measurements of the energy barrier and diffusion coefficient make DTA an ideal test case for our stochastic model of surface diffusion.

In this chapter, we will outline the model used for the ab inito calculations, and detail the results for DTA on Cu(111).

## 4.1 Model

To calculate energies and forces for use in a classical model of adatom dynamics, the quantum mechanical system is treated in the Born-Oppenheimer approximation. In

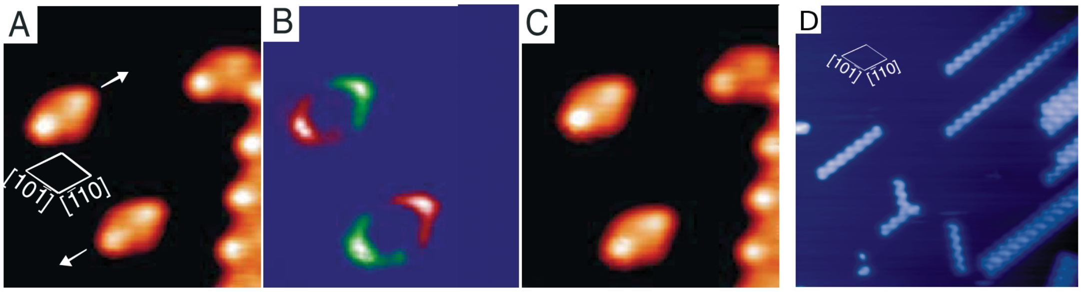

Figure 4.1: STM images for DTA on Cu(111), taken from Ref. [5]. Images A and C show two DTA molecules before and after a jump at high resolution (48 × 48Å area). The direction of the jumps, as well as the underlying Cu rows (not visible at this resolution) are indicated in image A. Image B is the difference between A and C, showing that the two molecules have jumped in opposite directions. Image D is a lower resolution image (23 × 23nm area), showing the formation of ordered rows of DTA.

this approximation, the nuclei of the atoms are treated as classical charged particles, defining an external potential for the electrons in the system. The Schroedinger equation for the electrons in this potential can then be solved to give an energy that depends on the positions $\vec{R}_i$ of the nuclei, thus defining a potential energy for the classical motion of the nuclei.

### 4.1.1 Born-Oppenheimer Approximation

Denoting the set of nuclear coordinates $\vec{R}_i$ by $\vec{R}$, and the electronic coordinates $\vec{r}_i$ by $\vec{r}$, the Schroedinger equation for the system reads

$$H\psi(\vec{R},\vec{r}) = E\psi(\vec{R},\vec{r}). \tag{4.1}$$

The Hamiltonian $H$ is given by

$$\begin{aligned} H = & -\sum_i \frac{\hbar^2}{2M_i}\nabla^2_{R_i} - \sum_i \frac{\hbar^2}{2m_e}\nabla^2_{r_i} + \sum_{i<j} \frac{Z_i Z_j e^2}{4\pi\epsilon_0|\vec{R}_i - \vec{R}_j|} + \sum_{i<j} \frac{e^2}{4\pi\epsilon_0|\vec{r}_i - \vec{r}_j|} \\ & - \sum_{i,j} \frac{Z_i e^2}{4\pi\epsilon_0|\vec{R}_i - \vec{r}_j|} \\ = & \; T_{\text{nucl}} + T_{\text{elec}} + V(\vec{R},\vec{r}), \end{aligned} \tag{4.2}$$

where $M_i$ and $m_e$ are the masses of the nuclei and electrons, $Z_i$ are the atomic numbers of the nuclei, and $e$ is the electronic charge. The Hamiltonian consists of the nuclear kinetic energy $T_{\text{nucl}}$, the electronic kinetic energy $T_{\text{elec}}$, and the potential energy $V(\vec{R}, \vec{r})$. The potential energy $V(\vec{R}, \vec{r}) = V_{\text{e-e}}(\vec{r}) + V_{\text{e-n}}(\vec{R}, \vec{r}) + V_{\text{n-n}}(\vec{R})$ is the sum of electron-electron repulsion, electron-nuclei attraction, and nuclei-nuclei repulsion terms.

Consider now the eigenstates of the Hamiltonian $H' = T_{\text{elec}} + V(\vec{R}, \vec{r})$,

$$H'\phi_n(\vec{R}; \vec{r}) = E'_n(\vec{R})\phi_n(\vec{R}; \vec{r}). \tag{4.3}$$

This can be thought of as the Schroedinger equation for the electrons at fixed nuclear coordinates $\vec{R}$. Due to the dependence of the potential energy on the nuclear coordinates, the eigenfunctions $\phi_n$ and eigenvalues $E_n$ will also depend on $\vec{R}$ in a parametric way. The full wave function $\psi$ can then be expanded in terms of the $\phi_n$'s,

$$\psi = \sum_n a_n(\vec{R})\phi_n(\vec{R}; \vec{r}), \tag{4.4}$$

giving rise to the following coupled equations for the $a_n(\vec{r})$ functions

$$\sum_n T_{\text{nucl}}^{(mn)} a_n + E'_m a_m = E a_m, \tag{4.5}$$

where the $T_{\text{nucl}}^{(mn)}$ are matrix elements of the nuclear kinetic energy operator, averaged over the electronic coordinates $\vec{r}$ only,

$$T_{\text{nucl}}^{(mn)} = \int d\vec{r} \phi_m(\vec{R}, \vec{r}) T_{\text{nucl}} \phi_n(\vec{R}, \vec{r}). \tag{4.6}$$

In the Born-Oppenheimer approximation, the off-diagonal elements of $T_{\text{nucl}}^{(mn)}$ are neglected, so that that the equations for the $a_n$'s decouple. In the adiabatic approximation, it is further assumed that the electrons occupy the instantaneous ground state for a fixed nuclear configuration, so that only the ground state electronic wave function $\phi_0(\vec{R}, \vec{r})$ is considered. The Schroedinger equation then becomes

$$T_{\text{nucl}} a_0 + E'_0 a_0 = E a_0. \tag{4.7}$$

In a classical model, this Schroedinger equation is replaced with the classical equations of motion for the nuclei in the potential $E'_0(\vec{R})$,

$$M_i \ddot{\vec{R}}_i = -\nabla_i E'_0(\vec{R}) \tag{4.8}$$

The force on the $i^{\text{th}}$ nucleus can be calculated by the Hellman-Feynman theorem

$$\vec{F_i} = -\nabla_{\vec{R}_i} E'_0(\vec{R}) = -\phi_0 \nabla_{\vec{R}_i} H' \phi_0. \tag{4.9}$$

The potential energy surface $E'_0(\vec{R})$ for the motion of the adsorbed molecule can therefore be obtained by calculating the electronic ground state for different configurations of the molecule along its diffusion path on the surface. From the potential energy surface, all properties of the system, including the friction and diffusion coefficients can be calculated. To calculate the electronic ground state, we employ density functional theory.

### 4.1.2 Kohn-Sham Density Functional Theory

To obtain the ground state energy of a system of $N$ electrons, the Schroedinger equation must be solved for the $N$-electron wave function $\psi(\vec{r}_1, \vec{r}_2, \dots)$. For systems of more than a few electrons, this is not feasible. For example, for a system of 100 electrons (still a relatively small system), calculating the wave function on a very course 10x10x10 spatial grid would require storing $1000^{100} = 10^{300}$ elements.

The problem of calculating the $N$-electron wave function is avoided in density functional theory (DFT) by making use of the Hohenburg-Kohn theorems [39], which allow one to calculate the ground state energy of an $N$-electron system from the one-electron density $n(\vec{r}) = N \int d\vec{r}_2 d\vec{r}_3 \dots |\psi(\vec{r}, \vec{r}_2, \vec{r}_3, \dots)|^2$. As mentioned in the previous section, the Hamiltonian for an $N$-electron system can be written as $H = T + V_{\text{e-e}} + V_{\text{ext}}$, where $T$ is the kinetic energy, $V_{\text{ee}}$ is the electron-electron interaction energy, and $V_{\text{ext}} = V_{\text{e-n}} + V_{\text{n-n}}$ is the external potential due to the interaction with the nuclei. The Hohenburg-Kohn theorems then state

1. There is a one-to-one correspondence between the external potential $V_{\text{ext}}$ and the ground state density $n_0(\vec{r})$. This implies that the external potential, and therefore all properties of the system are uniquely determined by the density. In particular, the energy can be written as a functional of the density, $E = E[n(\vec{r})] = T[n(\vec{r})] + V_{\text{e-e}}[n(\vec{r})] + \int d\vec{r} n(\vec{r}) V_{\text{ext}}(\vec{r})$.

2. The density $n(\vec{r})$ that minimizes the energy functional $E[n(\vec{r})]$ is the exact ground state density, and the energy obtained is the exact ground state energy. This allows for a variational calculation of the ground state energy.

The first part of the energy functional $F[n(\vec{r})] = T[n(\vec{r})] + V_{\text{e-e}}[n(\vec{r})]$ is universal in that it does not depend on the external potential, and is the same for any $N$-electron system. Unfortunately, the Hohenburg-Kohn theorems do not provide any means to determine the form of the energy functional, and there is no known scheme to systematically improve an approximation to $F[n(\vec{r})]$, or to even estimate the accuracy of a particular approximation *a priori*. There are, however, many approximations for the energy functional that have been shown to give good accuracy on a wide range of molecular and solid state systems. Issues related to the approximation of the energy functional for molecules adsorbed on surfaces will be discussed in more detail below.

Once a particular form has been chosen for the energy functional $F[n(\vec{r})]$, the ground state energy and density are found by minimizing the energy with respect to variations of the density. The most popular scheme for carrying out this variational calculation is the Kohn-Sham method [40].

In the Kohn-Sham formulation, the energy functional is re-written in the following way

$$F[n] = T[n] + V_{\text{e-e}}[n] = T_0[n] + E_H[n] + E_{\text{xc}}[n], \tag{4.10}$$

where $T_0[n]$ is the kinetic energy of a non-interacting $N$-electron system, the Hartree energy $E_H[n]$ is the classical electrostatic energy of a charge distribution $n(\vec{r})$, and the remaining term $E_{\text{xc}}[n]$ is called the exchange-correlation energy. The density is written in terms of single-particle orbitals $\phi_i(\vec{r})$ as $n(\vec{r}) = \sum_i |\phi_i(\vec{r})|^2$. The kinetic energy $T_0$ is then

$$T_0[n] = -\int d\vec{r} \sum_i \frac{\hbar^2}{2m} \phi_i(\vec{r}) \nabla^2 \phi_i(\vec{r}), \tag{4.11}$$

and the Hartree energy is

$$E_H[n] = \frac{1}{2} \int d\vec{r} \int d\vec{r}' \frac{e^2 n(\vec{r}) n(\vec{r}')}{4\pi\epsilon_0 |\vec{r} - \vec{r}'|} = \frac{1}{2} \int d\vec{r} V_H(\vec{r}) n(\vec{r}), \tag{4.12}$$

where the Hartree potential $V_H(\vec{r})$ has been defined. The exchange-correlation energy, can be written formally as $E_{\text{xc}}[n] = T[n] - T_0[n] + V_{\text{e-e}}[n] - E_H[n]$.

The orbitals $\phi_i$ are determined by minimizing the energy under the constraint of normalization,

$$\frac{\delta}{\delta \phi_i} \left[ E[n(\vec{r})] - \sum_i \epsilon_i (1 - [\phi_i, \phi_i]) \right] = 0, \tag{4.13}$$

leading to the Kohn-Sham equations for the orbitals

$$-\frac{\hbar^2}{2m}\nabla^2\phi_i + V_{\rm KS}(\vec{r})\phi_i = \epsilon_i\phi_i. \tag{4.14}$$

The Kohn-Sham potential is $V_{\rm KS} = V_{\rm ext} + V_H + V_{\rm xc}$, where the exchange correlation potential is

$$V_{\rm xc}(\vec{r}) = \frac{\delta E_{\rm xc}[n]}{\delta n}. \tag{4.15}$$

The Kohn-Sham equations have the form of single particle Schroedinger equations for the orbitals $\phi_i$, with a potential that however depends on the orbitals themselves, through the density. These equations can be solved self-consistently to obtain the density and ground state energy.

The form of the exchange-correlation energy functional $E_{\rm xc}[n]$ is not known, and it must be approximated. The most widely used approximation is the generalized gradient approximation (GGA), in which $E_{\rm xc}$ is written in terms of the local value of the density, as well as its gradient,

$$E_{\rm xc}^{\rm GGA}[n] = \int d\vec{r} v_{\rm xc}(n(\vec{r}), |\nabla n(\vec{r})|)n(\vec{r}). \tag{4.16}$$

The form of the $v_{\rm xc}$ function is generally chosen so that $E_{\rm xc}$ satisfies several known conditions, such as the sum rule for the exchange-correlation hole, and scaling properties. The functional of Perdew, Burke, and Ernzerhof (PBE) [41] is a widely used GGA functional constructed using this approach.

The GGA has been successful in describing many solid state and molecular systems, however it has some shortcomings. For the description of organic molecules adsorbed on surfaces, the most important shortcoming is the failure to describe van der Waals forces. When two atoms or molecules are well separated so that their electron clouds are non-overlapping, the energy in the GGA falls off exponentially. Due to dispersion forces between the atoms, the energy should rather fall off as $1/R^6$, where $R$ is the distance between the atoms.

This neglect of van der Waals forces causes GGA-type functionals to severely underestimate the binding energy in some systems, such as weakly bound dimers and layered solids such as graphite [42]. For organic molecules adsorbed on metal surfaces, van der Waals forces are critical for obtaining accurate adsorption energies. For benzene adsorbed on (111) surfaces of noble metals, the PBE functional underestimates the binding energy by about an order of magnitude [43–46]. Similar results for the adsorption energies are seen for azobenzene adsorbed on metals, with also significant changes in the adsorption geometry induced by the van der Waals forces [47–49].

Although it is now well understood that van der Waals forces are important for determining the adsorption energy of organic molecules on surfaces, there has been little work investigating the effect of these corrections on the energy profiles for migration of the adsorbed molecules. For DTA adsorbed on Cu(111), the molecule-surface interaction is the result of a balance between the van der Waals-dominated interaction between the carbon rings and the surface, and the stronger chemisorption-type S-Cu bonding (which should be well-described by the GGA). An accurate description of van der Waals forces may therefore be expected to be important in determining the relative stability of different adsorption geometries, and hence the shape of the potential energy curve for migration.

There are two basic approaches for including the van der Waals energy in DFT. In the first approach, pairwise energy terms proportional to $1/R^6$ are added to the DFT energy, with the coefficients for each term determined empirically or from more accurate first principles calculations. In this approach the total energy is therefore written as

$$E = E_{\mathrm{DFT}} - \sum_{ij} \frac{C_{ij}}{R_{ij}^6} f_d(R_{ij}, R_{ij}^{(0)}), \tag{4.17}$$

where $R_{ij} = |\vec{R}_i - \vec{R}_j|$, and $R_{ij}^{(0)}$ is an empirical cutoff radius. The function $f_d$ is a damping function which must be included to eliminate the divergence of the pairwise terms as the atoms approach each other. The form of this function, as well as the cutoff radii $R_{ij}^{(0)}$ are arbitrary, and must be fit empirically to experimental data or high accuracy quantum chemical calculations.

In the second approach, a non-local term is added to the exchange-correlation functional, so that $E_{xc}$ is written as

$$E_{\mathrm{xc}} = E_{\mathrm{xc}}^{\mathrm{loc}} + E_{\mathrm{c}}^{\mathrm{nl}}, \tag{4.18}$$

where the local part of the exchange-correlation $E_{\mathrm{xc}}^{\mathrm{loc}}$ is treated in the GGA, and the non-local correlation energy part is written in terms of the density as

$$E_{\mathrm{c}}^{\mathrm{nl}} = \frac{1}{2} \int d\vec{r} \int d\vec{r}' \phi(\vec{r}, \vec{r}') n(\vec{r}) n(\vec{r}'). \tag{4.19}$$

The kernel $\phi(\vec{r}, \vec{r}')$ is chosen to produce the correct asymptotic behavior for well separated fragments.

Although the latest semi-empirical, and vdW-functional methods are approaching quantitative accuracy for some systems, there is still a fairly large spread in the predicted binding energies and equilibrium geometries in many cases. We will therefore test and compare several methods for van der Waals corrections in our calculations for DTA on Cu(111).

### 4.1.3 Periodic Calculations

Extended systems, such as bulk solids or surfaces, can be represented by employing periodic boundary conditions. The positions of the nuclei are periodically repeated, resulting in a periodic external potential for the electrons. The Kohn-Sham orbitals can then be written according to Bloch's theorem

$$\phi_{n\vec{k}}(\vec{r}) = e^{i\vec{k}\cdot\vec{r}} u_{n\vec{k}}(\vec{r}), \tag{4.20}$$

where the wave vector $\vec{k}$ ranges over the Brillouin zone, and the $u_{n\vec{k}}$ are periodic functions. A convenient basis set for the periodic functions is the set of plane waves $e^{i\vec{g}_l \cdot r}$, where $\vec{g}_l$ is a reciprocal lattice vector. The orbitals are then written as

$$\phi_{n\vec{k}}(\vec{r}) = \sum_l c_{nl} e^{i(\vec{k}+\vec{g}_l)\cdot\vec{r}}. \tag{4.21}$$

The size of the basis set is determined by the maximum wave vector $\vec{g}_l$ used, usually specified as an energy cutoff $E_{\text{max}} = \frac{\hbar^2}{2m}|\vec{g}_{\text{max}}|^2$, and the sampling of $\vec{k}$-points from the Brillouin zone.

To obtain the total energy, in principle the energy eigenvalues $E_{n\vec{k}}$ must be integrated over the Brillouin zone. In practice, the integral is replaced by a sum over some discrete set of $\vec{k}$-points,

$$E = \sum_{n,\vec{k}_m} E_{n\vec{k}_m} f_{n\vec{k}_m}, \tag{4.22}$$

where $f_{n\vec{k}_m}$ are the occupancies of each state $\phi_{n\vec{k}_m}$, and are 0 or 1 for an occupied or unoccupied state, i.e. $f_{n\vec{k}_m} = \Theta(E_f - E_{n\vec{k}_m})$, where $E_f$ is the Fermi energy of the system. In metals, the continuum of states at the Fermi level causes this sum to converge very slowly with respect to the number of $\vec{k}$-points sampled. To speed convergence, smearing methods are typically used, in which the step function in the occupancies $f_{n\vec{k}_m}$ is replaced by a function that decays smoothly from 1 to 0, allowing for partial occupancy of states near the Fermi level.

## 4.2 Results

In this section the results of calculations for DTA on the Cu(111) surface are shown. Energy barriers for diffusion of DTA are calculated using several methods of accounting for van der Waals (vdW) interactions, and compared with experimental results. Due to the small size of the energy barriers in this system, an important part of these calculations is a careful test of the convergence of the results with respect to the basis set and the size of the unit cell, and these tests are detailed at the end of this chapter.

Calculations shown in this section were performed with the VASP software package. The Cu(111) surface was represented by a supercell consisting of 5x4 primitive surface unit cells and 3 layers, with a vacuum gap of 10Å between periodically repeated slabs. A single DTA molecule was placed on one side of the slab, with the supercell employed leaving a separation of approximately 3-4Å between periodically repeated DTA molecules. Tests with larger supercells showed that this is sufficient to give the low coverage limit of energy barriers to within 10meV. Tests with up to 7 layers also showed that energy barriers are sufficiently converged at 3 layers. A plane wave kinetic energy cutoff of 800eV and a $5 \times 6$ grid of k-points were used. Relaxations were performed until the forces on all atoms were less than 0.01eV/Å. Convergence tests showed that this gives energies converged to an accuracy of better than 10meV.

### 4.2.1 Bulk Calculations

The first step in a surface calculation is determining the bulk lattice constant of the solid. This is done by calculating the energy of the bulk system for several values of the lattice constant $a$ near the equilibrium value (for cubic crystals such as fcc Cu, only one lattice constant needs to be adjusted). The resulting energies are then fit to an equation of state to determine the ideal lattice constant. Here, the Birch-Murnaghan

Table 4.1: Equilibrium lattice constants $a_0$ (in Å) and bulk moduli $B_0$ (in GPa) for Cu, obtained by fitting to Eq. (4.23) for various van der Waals correction schemes. Experimental values [50] are also shown for comparison.

| | PBE | optPBE | optb86b | optb88 | vdw-DF2 | DFT-D2 | TS0 | TSS | Expt. |
|---|---|---|---|---|---|---|---|---|---|
| $a_0$ | 3.635 | 3.651 | 3.601 | 3.629 | 3.750 | 3.571 | 3.547 | 3.607 | 3.595 |
| $B_0$ | 137 | 130 | 149 | 139 | 103 | 148 | 171 | 213 | 142 |

equation of state is employed,

$$E(V) = E_0 + \frac{9}{16} V_0 B_0 \left( B_1 \left[ \frac{1}{3} \left( \frac{V_0}{V} \right)^2 - 1 \right]^3 + \left[ \frac{1}{3} \left( \frac{V_0}{V} \right)^2 - 1 \right]^2 \left[ 6 - \frac{4}{3} \left( \frac{V_0}{V} \right)^2 \right] \right), \tag{4.23}$$

where $V = a^3$ is the volume, $V_0$ is the equilibrium volume, $B_0$ is the bulk modulus and $B_1$ is the derivative of $B_0$ with respect to pressure. The calculated values of the energy $E$ as a function of unit cell volume are fit to the above equation using a least-squares procedure, giving a value for the equilibrium lattice constant $a_o = V_0^{1/3}$, as well as the bulk modulus $B_0$. Fig. 4.2 shows the resulting equation of state curves for fcc Cu for a few of the vdW correction methods employed. The resulting lattice constants and bulk moduli are shown in Table 4.1. Strictly speaking, this method gives an estimate for the lattice constant at zero temperature, while real metals undergo thermal expansion at finite temperatures. Copper has a linear thermal expansion coefficient of approximately $10^{-5}\mathrm{K}^{-1}$, resulting in an expected increase in the lattice constant of less than 1%. This does not significantly effect the energy of the adsorbed DTA molecule (see Fig. 4.8), and so this effect is ignored in the present calculations.

The different vdW correction methods shown in Table 4.1 consist of both semi-empirical correction methods and non-local correlation functionals. The non-local functionals are all based on the van der Waals density functional (vdW-DF) of Dion et. al [51]. The vdW-DF2 functional is an alternate version of vdW-DF employing the PW86 functional for the exchange, introduced when it was found that vdW-DF tends to overestimate binding separations and underestimate the strength of hydrogen bonding [52]. Both vdW-DF and vdW-DF2 tend to overestimate separation distances for systems bound by vdW forces, and this trend is also observed in an overestimation of the Cu lattice constant.

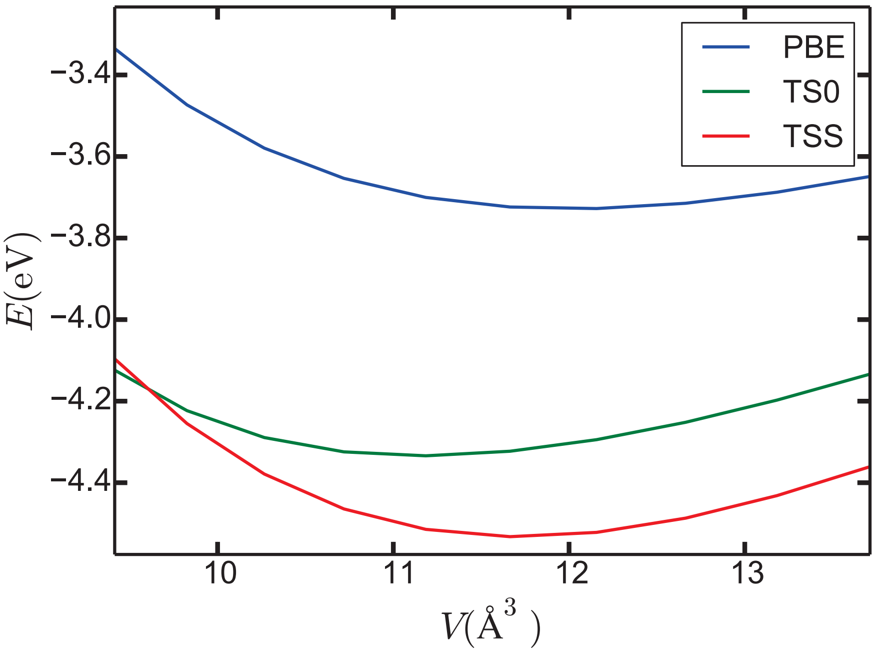

Figure 4.2: Energy versus volume curves for fcc Cu, for PBE without vdW corrections, as well as the TS and TS-surf vdW corrections. Calculations were performed using a 400eV energy cutoff and a 21x21x21 k-point grid.

The optPBE, optb88 and optb86b functionals consist of the non-local correlation part of vdW-DF, with exchange functionals that have been optimized for use with the vdW-DF correlation. The optPBE and optb88 functionals [53] have been optimized by fitting to the S22 set of accurate quantum chemical calculations of binding energies for a set of weakly interacting dimers [54]. Both functionals slightly overestimate the lattice constant of Cu, and underestimate the bulk modulus. These functionals were found to have an accuracy similar to PBE for a range of solids [55]. The optb86b functional was found to give improved accuracy over PBE for the description of solids [55], including Cu. It has similar accuracy to optb88 for the s22 set.

Two semi-empirical vdW correction methods were tested. In the DFT-D2 method of Grimme et. al [56], pairwise $1/R^6$ terms are added to the energy as in equation (4.17), where the $C_6$ coefficients for each atom type are calculated from the empirical formula $C_6 = 0.05 N I_p \alpha$ in terms of the ionization potential $I_p$ and polarizability $\alpha$ ($N$ takes the values 2,10,18,36,54 for the first 5 rows of the periodic table).

The Fermi function is used for damping of the terms at short distances,

$$f_d(R_{ij}, R_{ij}^{(0)}) = \frac{s_D}{\exp\left[-d\left(\frac{R_{ij}}{s_R R_{ij}^{(0)}} - 1\right)\right] + 1}. \tag{4.24}$$

In the DFT-D2 method, the scaling parameter $s_R$ is set to unity, while $s_D$ is fit to a set of reference data from accurate quantum chemical calculations. The parameter $d$ sets the sharpness of the cutoff at $R_{ij} \lesssim s_R R_{ij}^{(0)}$, and is set to $d = 20$ in the DFT-D2 method.

In the method of Tkatchenko and Scheffler (TS0) [57], the same pairwise form and damping function are used, but the effect of polarization on the vdW interactions is accounted for by introducing a dependence of the $C_6$ coefficients and cutoff radii $R_{ij}^{(0)}$ on the local electron density around each atom. The basic idea of the TS method is to define an effective volume for each atom according to the Hirshfeld partitioning,

$$\frac{V_i^{\text{eff}}}{V_i^{\text{free}}} = \frac{\int d\vec{r} r^3 w_i(\vec{r}) n(\vec{r})}{\int d\vec{r} r^3 n_i^{\text{free}}(\vec{r})} \qquad w_i(\vec{r}) = \frac{n_i^{\text{free}}(\vec{r})}{\sum_j n_j^{\text{free}}(\vec{r})}, \tag{4.25}$$

where the “free” superscripts refer to the isolated atoms in vacuum. This effective volume is then related to the effective polarizability $\alpha_i^{\text{eff}}$ of each atom through $V_i^{\text{eff}} = \kappa_i^{\text{eff}} \alpha_i^{\text{eff}}$, where $\kappa_i^{\text{eff}}$ is a proportionality constant. The $C_6$ coefficients and cutoff radii are rescaled according to $C_{6i}^{\text{eff}} = \left(\frac{V^{\text{eff}}}{V^{\text{free}}}\right)^2 C_{6i}^{\text{free}}$, and $R_{i,\text{eff}}^{(0)} = \left(\frac{V^{\text{eff}}}{V^{\text{free}}}\right)^{1/3} R_{i,\text{free}}^{(0)}$, an expression derived from the Casimir-Polder integral for the $C_6$ coefficients. In the TS method, the scaling parameter for the $C_6$ coefficients $s_D$ is taken to be unity, and the scaling for the cutoff radii $s_R$ is taken as an empirical parameter, fit for each exchange-correlation functional.

In a revised version of the method designed to treat organic molecules adsorbed on surfaces (TSS) [58], the $C_6$ coefficients for the substrate atoms are re-calculated to reproduce screening effects. The vdW interaction energy for an atom or molecule above a surface falls off as $C_3/z^3$, where $z$ is the height above the surface. In the TSS method, the pairwise $C_6/R^6$ terms between the atoms of the adsorbed molecule and those of the surface are chosen to reproduce this effective $C_3/z^3$ force, the relationship between the coefficients being $C_3^{ij} = n_s \frac{\pi}{6} C_6^{ij}$, where $n_s$ is the number of substrate atoms per unit volume. The $C_3$ coefficients are calculated using Lifshitz-Zaremba-Kohn theory, which can account for many-body screening effects in the solid, and these coefficients are then used to calculate effective $C_6$ coefficients for the atoms in the solid.

From Table 4.1 it can be seen that both the DFT-D2 and TS0 methods underestimate the Cu lattice constant. The TSS method brings the lattice constant in line with the experimental value, but significantly worsens the over-estimation of the bulk modulus.

Although the main influence of vdW interaction in surface adsorption is an overall attractive force that pulls the adsorbed molecule closer to the surface, an accurate description of the substrate is still important in determining the energy landscape seen by a diffusing molecule. This is particularly true in the case of DTA adsorbed on Cu(111), where the energy barrier for diffusion depends sensitively on the fit between the molecular geometry and substrate lattice constant, as will be discussed in detail below.

### 4.2.2 DTA on Cu

DTA consists of an anthracene backbone with two S atoms attached to C atoms in the central ring, shown in Fig. 4.3. Experimentally, DTA has been observed to adsorb on the Cu(111) surface with its molecular plane parallel to the surface, and the long axis of the anthracene backbone parallel to the close-packed [110] direction (as in the T1 and T2 sites in Fig 4.3) [5]. At low temperatures a second stable configuration was found, with the molecular axis rotated with respect to the Cu rows.

In DFT calculations at the PBE level, these rotated configurations, sites M1 and M2 in Fig. 4.3, were found to be the stable minimum energy configurations for the adsorbed DTA molecule. Configurations with the anthracene backbone aligned with the Cu rows (T1 and T2 in Fig. 4.3) were found to be saddle points on the minimum energy path between these two sites.

At the M1 and M2 sites, the S atoms lie near bridge sites, with one S atom between a bridge site and an fcc-hollow site, and the other between a bridge site and an hcp-hollow site. A similar arrangement was seen in DFT calculations for thiophenol adsorbed on a Cu(111) substrate [59], and is also in agreement with the preference for HS to adsorb at bridge sites on Cu(111) [60]. The M1 and M2 sites are equivalent due to the symmetries of the surface and molecule (one can be obtained from the other by reflection about a plane in the perpendicular to the surface with its normal along the [110] direction). Small differences ($\lesssim$ 10meV) in the energies for these two sites in calculations come from both the inherent numerical noise in the calculations as well as interactions between periodically repeated images of the DTA molecules, which breaks the equivalence of the two sites.

At the T1 and T2 sites, one of the S atoms lies near an on-top site. The higher energy of this configuration at the PBE level is in line with the instability of the on-top site for HS adsorbed on the Cu(111) surface [60]. At the T1 site, the centers of the carbon rings of DTA sit above fcc-hollow sites, while at the T2 site the rings sit above hcp-hollow sites. Although there is little difference in the energies of the T1 and T2 sites at the PBE level, there is still a slight preference for the T2 site, in agreement with the preference for benzene to adsorb at hcp-hollow sites on Cu(111) [43]. Anthracene was observed to adsorb parallel to the close-packed directions on the Cu(111) surface under solution [61], suggesting a preference of the anthracene backbone of DTA for the T1 and T2 sites, while the S atoms have a preference for the M1 and M2 sites.

Experimentally, it is observed that the preference of the anthracene backbone to be aligned with the Cu rows wins out, and a T1/T2 like site is the stable adsorption configuration. However, due to a severe underestimation of dispersion interactions in standard GGA functionals such as PBE, neither of these sites is stable at the PBE level. The need for an accurate description of vdW forces for adsorbed organic molecules has been seen, e.g., in calculations of the adsorption energy of benzene on noble metal surfaces, where PBE underestimates the adsorption energy by an order of magnitude compared to experimental measurements, while including vdW corrections brought the adsorption energies into close agreement with experiments [44].

### Effect of van der Waals Corrections

When vdW corrections are introduced, the increased attraction between the carbon rings and Cu surface results in an altered adsorption geometry, with DTA being pulled significantly closer to the surface, as shown in Fig. 4.4. The average DTA-Cu distances calculated for each vdW correction method are given in Table 4.2. The bend about the central carbon ring is also significantly reduced, resulting in a more

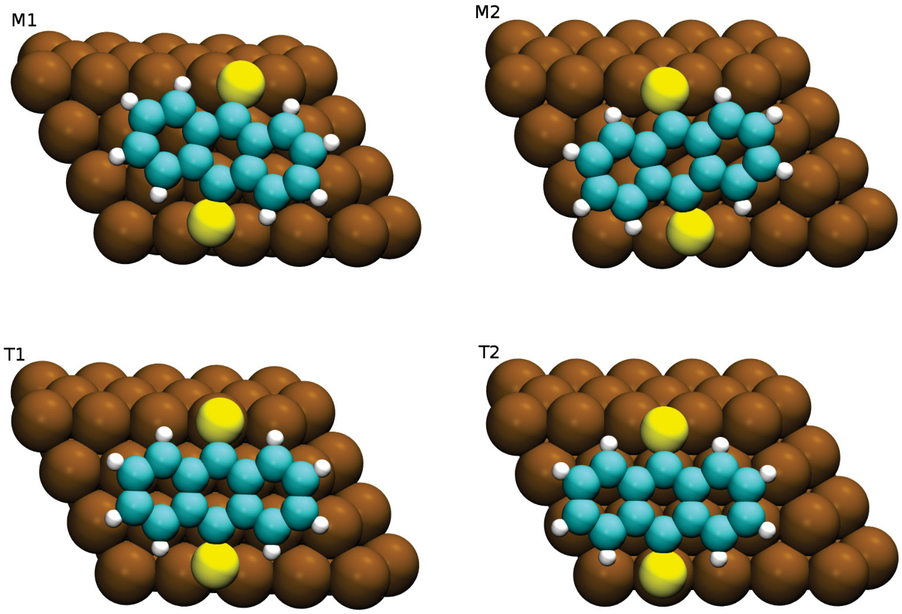

Figure 4.3: The two (symmetry equivalent) minimum energy sites, labelled M1 and M2, and the two transition states, labelled T1 and T2, for DTA adsorbed on Cu(111).

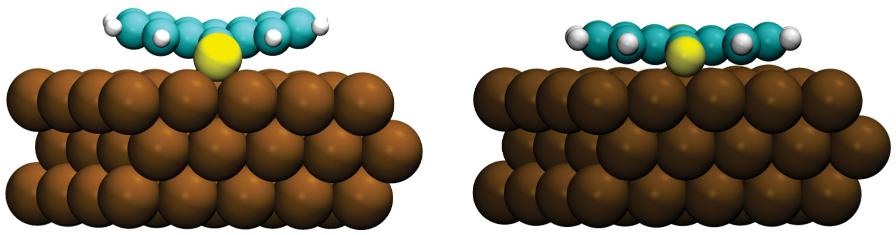

Figure 4.4: Optimized geometry for the T1 site calculated with PBE (left) and D2 (right).

Table 4.2: Energy differences between the T1,T2, and M1 sites (in meV), and average molecule-surface height (in Å) calculated with various vdW correction methods. The experimental energy barrier for diffusion is 130meV. [5]

| | PBE | vdW-DF2 | optPBE | optb88 | optb86b | DFT-D2 | TSS |
|---|---|---|---|---|---|---|---|
| $V_{\mathrm{T1}} - V_{\mathrm{M1}}$ | 197 | 46 | 149 | 171 | 179 | 187 | 151 |
| $V_{\mathrm{T2}} - V_{\mathrm{M1}}$ | 187 | 45 | 142 | 154 | 86 | 92 | 72 |
| $V_{\mathrm{T1}} - V_{\mathrm{T2}}$ | 10 | 1 | 7 | 17 | 93 | 95 | 79 |
| $\langle d_{\text{DTA-Cu}} \rangle$ | 2.99 | 3.22 | 2.84 | 2.71 | 2.41 | 2.35 | 2.44 |

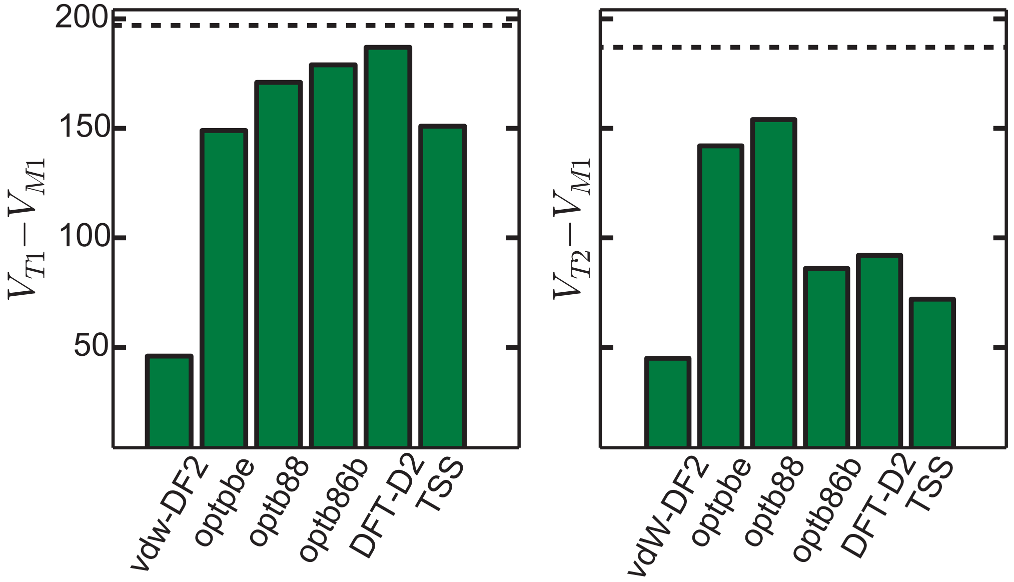

Figure 4.5: Energy of T1 and T2 sites relative to M1 for the various vdW correction methods employed. The dashed lines show the uncorrected PBE results.

planar geometry. This was true for all tested vdW correction methods other than vdW-DF and vdW-DF2, for which there was little change from the PBE geometries. Going from optPBE to optb88 to optb86b, the height of DTA above the surface is reduced. Both semi-empirical methods gave similar geometries to optb86b.

The energies of the T1 and T2 sites relative to M1 are shown in Fig. 4.5 (and Table 4.2) for the different vdW correction methods. Two trends can be observed in the relative energies of the T1, T2, and M1 sites upon introducing vdW corrections. Firstly, all methods decrease the energy of the T1 and T2 sites relative to M1, consistent with the prediction that the vdW forces should increase the strength of the interaction between anthracene and the Cu surface, tending to align DTA with the

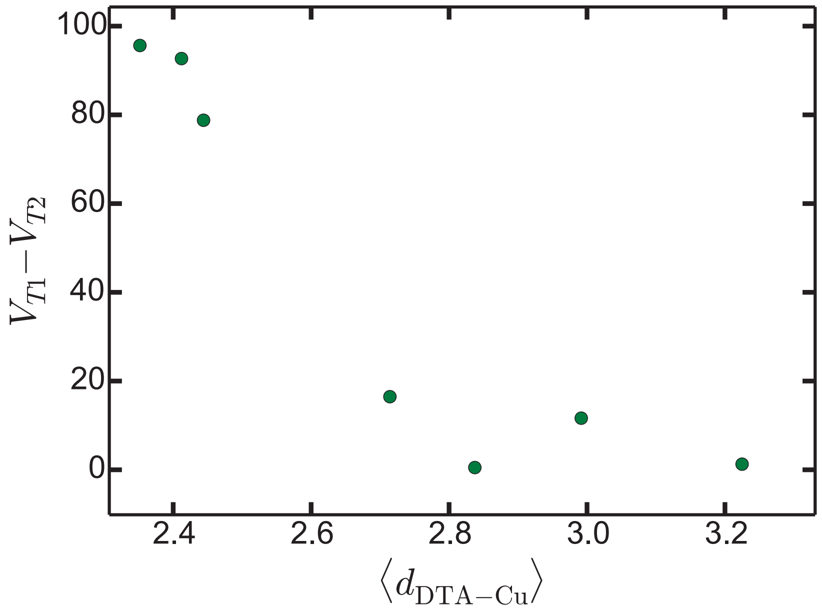

Figure 4.6: Energy difference between the T1 and T2 sites as a function of the average height of DTA above the Cu(111) surface, for the various vdW correction methods employed. From left to right, the points are for DFT-D2, optb86b, TSS, optb88, optPBE, PBE, vdW-DF2.

Cu rows. Secondly, the methods that give a geometry with DTA closer to the surface predict a lowering of the energy of the T2 site compared to T1. This can be seen more clearly in Fig. 4.6, which shows the T1-T2 energy difference as a function of the average height of DTA above the surface. The closer the C-rings of DTA get to the surface, the larger the energy difference predicted between the T1 and T2 sites. The lower energy of T2 compared to T1 is consistent with calculations for benzene adsorbed on Cu(111), where the energy for benzene adsorbed above hcp-hollow sites is slightly lower than above fcc-hollow sites. The lower energy of T2 is also consistent with the experimental observation that the DTA molecule migrates via jumps that span the full Cu-Cu distance, while T1 and T2 are separated by only half this distance, implying that only one of these sites should be stable.

Although the vdW correction methods give the correct qualitative trend for the energies of the T1 and T2 sites, all methods still predict M1 to be the lowest energy site, in disagreement with experimental observations. The equilibrium distance between the C-rings of DTA and the surface is determined by the balance between vdW attraction and Pauli repulsion as DTA approaches the surface. The trends observed in Figs. 4.5 and 4.6 suggest that the energy of the T2 site depends sensitively on the height of DTA above the surface, and is therefore strongly affected by the behavior of the vdW forces at short distances.

In the semi-empirical vdW methods, this behavior can be adjusted in a simple way by adjusting the cutoff radii for the pairwise terms in Eq. (4.17). There is no way to determine the cutoff radii or the form of the damping function a-priori, so they must be fit to accurate quantum chemical calculations or experiment. In the TS0/TSS methods, this is accomplished by a uniform scaling of the cutoff radii for each atom type (which are determined from the equilibrium separation of noble gas dimers) by a single scaling parameter $s_R$. In the original specification of the TS0 method, this parameter was determined by fitting to the binding energies of the s22 data set [54], which consists of weakly bound dimers of organic molecules. Although very accurate values for the binding energies in this set were obtained with a value of $s_R = 0.94$, the transferability of this value to a molecule adsorbed on a metal surface is not obvious.

We therefore investigate the effect of decreasing the cutoff radii by lowering the

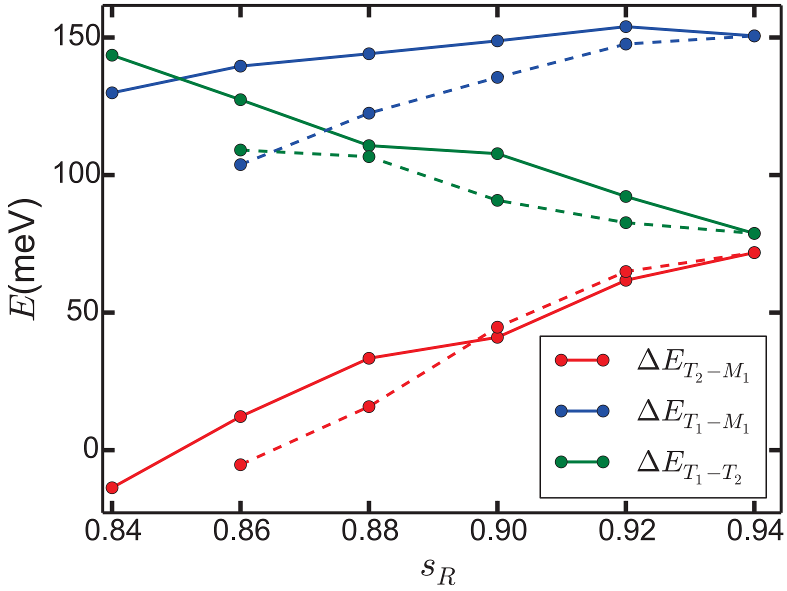

Figure 4.7: Energy of the T1 and T2 sites relative to M1, as a function of the cutoff scaling parameter $s_R$ in the TSS method. The solid lines show barriers calculated with a Cu lattice constant of $a = 3.607\AA$, while the dashed lines show the barriers calculated at the equilibrium lattice constant for each value of $s_R$.

Table 4.3: Lattice constant $a$ (in $\AA$) and bulk modulus $B$ (in GPa) for Cu as a function of the cutoff scaling parameter $s_R$ in the TSS method.

| $s_R$ | 0.84 | 0.86 | 0.88 | 0.90 | 0.92 | 0.94 |
|---|---|---|---|---|---|---|
| $a$ | 3.464 | 3.490 | 3.518 | 3.548 | 3.578 | 3.607 |
| $B$ | 264 | 266 | 260 | 247 | 230 | 213 |

scaling parameter $s_R$. Fig. 4.7 shows the energy of the T1 and T2 sites relative to M1 as a function of $s_R$. As $s_R$ decreases, the vdW attraction persists to shorter C-Cu distances, resulting in DTA being pulled closer to the surface. There is a corresponding lowering of the energy at the T1 and T2 sites relative to M1, with T2 eventually becoming lower in energy than M1 for $s_R \lesssim 0.84$. The energy at the T2 site is also lowered with respect to the T1 site by lowering $s_R$, and for $s_R \approx 0.86$ the energy difference between the T2 and T1 sites closely matches the experimental energy barrier of 130meV.

While a lower value for $s_R$ seems to better reproduce the experimental energy barrier and adsorption geometry for DTA, it also affects the description of the substrate,

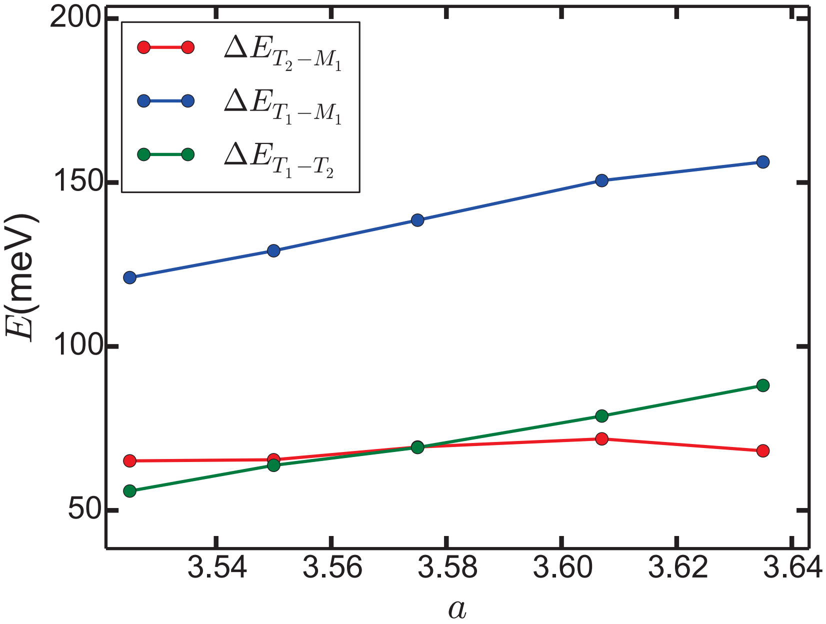

Figure 4.8: Energy of the T1 and T2 sites relative to M1, as a function of the Cu lattice constant for the TSS method.

due to Cu-Cu vdW interactions. Table 4.3 shows the predicted lattice constant and bulk modulus for Cu as a function of $s_R$. It can be seen that the lattice constant for Cu becomes smaller as $s_R$ is decreased, becoming as much as 3.6% smaller than the experimental value for $s_R = 0.84$. The overestimation of the bulk modulus by the TSS method also becomes worse as $s_R$ is decreased. Although a less accurate description of the substrate is not a significant problem for the description of diffusion of the adsorbed molecule, it can indirectly affect the calculated energy barriers by introducing a mismatch between the spacing of the Cu atoms and the geometry of the adsorbed molecule.

Experimentally, the spacing between neighboring hollow sites along the [110] direction on Cu(111) is 2.54Å, while the spacing between the centers of the C-rings of anthracene is 2.44Å. This extremely close match between the geometry of the substrate and molecule suggests that the energy barriers may be sensitive to the Cu lattice constant. To investigate this effect, we plot in Fig. 4.7 the energies for both a fixed lattice constant of $a = 3.607$Å, and a lattice constant that is adjusted to the equilibrium value at each $s_R$. It can be seen that allowing the lattice constant to change as $s_R$ is varied lowers the energy of both T1 and T2 relative to M1, with T1 being affected more strongly. This is also shown in Fig. 4.8, where the energies are plotted as a function of Cu lattice constant, with a fixed $s_R = 0.94$. The energy at T1 is seen to be strongly affected by the lattice constant, changing by more than 20% for a change of only 0.1Å in the lattice constant. For calculations of diffusion of DTA on Cu(111), we will therefore employ the TSS method with the cutoff parameter $s_R$ adjusted to 0.84, and the lattice constant held constant at the value 3.607Å . Although such an ad-hoc adjustment of the fitting parameter $s_R$ should not be expected to be transferable to other systems, for DTA on Cu(111) it gives an energy curve that agrees well with all available experimental information, including the energy barrier for diffusion, the adsorption geometry (including the precence of a meta-stable configuration), and the jump length for surface migration.

### Adiabatic Potential

The adiabatic potential $V_a(x)$ as a function of DTA center of mass position $x$ along the [110] direction is shown in Fig. 4.9. $V_a(x)$ was calculated by minimizing the energy at fixed $x$ while allowing the DTA molecule and the positions of the top two layers of the Cu(111) slab to relax.

From Fig. 4.9 it can be seen that introducing vdW corrections to the DFT energy lowers the energy of the T2 site substantially (and also shifts the site slightly to the left in the center of mass coordinate). Lowering the empirical cutoff scaling parameter $s_R$ causes the vdW forces to persist to shorter DTA-Cu distances, and further lowers the energy of the T2 site, so that it becomes the global energy minimum. Although this gives an energy curve that is agrees quite well with experiment, it is also possible that the curve calculated by the unmodified TSS method is consistent with experimental measurements.

The TSS method predicts that the T2 site is a transition state between sites M1 and M2, with a lower energy barrier than that at T1 (see Fig. 4.5). This lower barrier implies that jumps between M1 and M2 via the T2 site will occur on a timescale much faster than jumps via the T1 site. Using the experimental value of $4 \times 10^9$Hz for the jump rate prefactor, and the predicted barrier of 72meV, the jump rate over the T2 site would be on the order of 500-5000 Hz at the experimental temperature

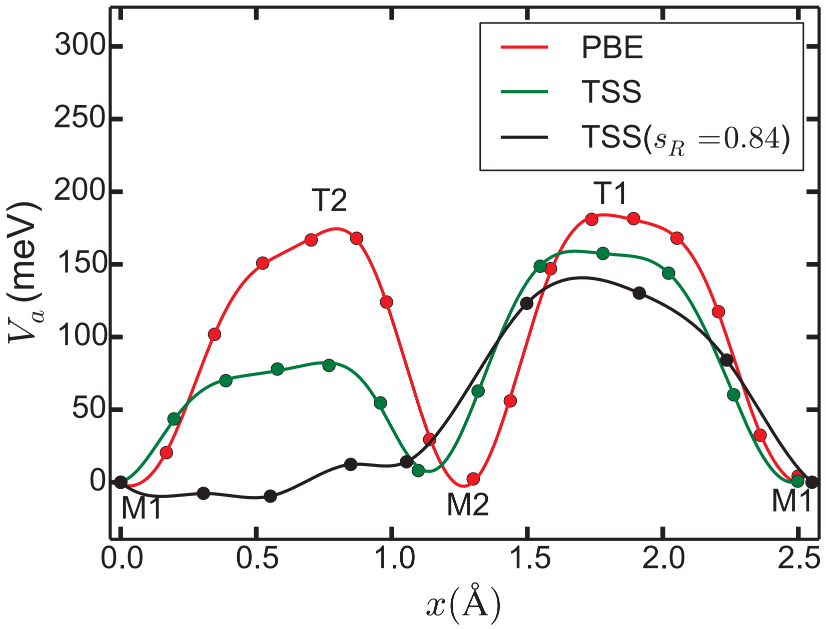

Figure 4.9: Adiabatic potential $V_a$ as a function of center of mass position of the DTA molecule along the [110] direction of the Cu(111) surface. The curves shown were calculated using PBE without vdW corrections, PBE with TS-surf semi-empirical corrections, and TS-surf with the cutoff scaling parameter $s_R$ decreased from 0.94 to 0.84.

range of 53-62K. Since this rate is fast compared to the scanning rate of the STM used to image the DTA molecules, the image obtained would be an average over the M1 and M2 sites. The STM images would therefore not appear to be tilted with respect to the Cu rows, although they should appear to be elongated on one side, as one the S atoms would span approximately one lattice constant on either side of the on-top site. The resolution of the STM images from Ref. [5] makes it difficult to discern whether this expected asymmetric appearance of the DTA molecules can be observed. There is also the experimental observation of a second configuration at low temperatures that is tilted with respect to the Cu rows. It is possible that the two minima observed at low temperatures are in fact the M1 and M2 sites of Fig. 4.3 (it is not specified in Ref. [5] whether two or three distinct configurations were observed).

### 4.2.3 Convergence Tests

The two parameters that control the size of the basis set in plane wave calculations are the plane wave cutoff, and the sampling of the Brillouin zone. The basis set consists of plane waves $e^{i(\vec{g}_l+\vec{k})\cdot\vec{r}}$ with reciprocal lattice vectors $\vec{g}_l$ satisfying $|\vec{g}_l+\vec{k}|^2 < \frac{2m}{\hbar^2}E_{\mathrm{cut}}$ for some energy cutoff $E_{\mathrm{cut}}$. For sampling of the surface Brillouin zone, we use uniformly spaced $M \times N$ grids of k-points, given in terms of the reciprocal lattice vectors $\vec{b}_1$ and $\vec{b}_2$ by

$$\vec{k}_{mn} = \frac{m}{M}\vec{b}_1 + \frac{n}{N}\vec{b}_2, \tag{4.26}$$

where $m$ ranges from 0 to $M-1$ and $n$ from 0 to $N-1$.

Since the energy differences between different relevant configurations of DTA on Cu are on the order of only a few tens of meV's, the basis must be chosen so that the energy is converged to within less than this threshold. During geometry optimizations, it was found that the energy at a local minimum was converged to within approximately 1meV when all forces were less than 0.01meV/Å. The forces must therefore be converged with respect to the basis set to within less than this threshold. Accurate forces are also important for the calculation of vibration frequencies. In the following we systematically test the convergence of the energy and forces with respect to both the energy cutoff and the number of k-points sampled. We also make tests for larger supercells to ensure that the energy is converged with respect to the coverage of DTA and the number of layers.

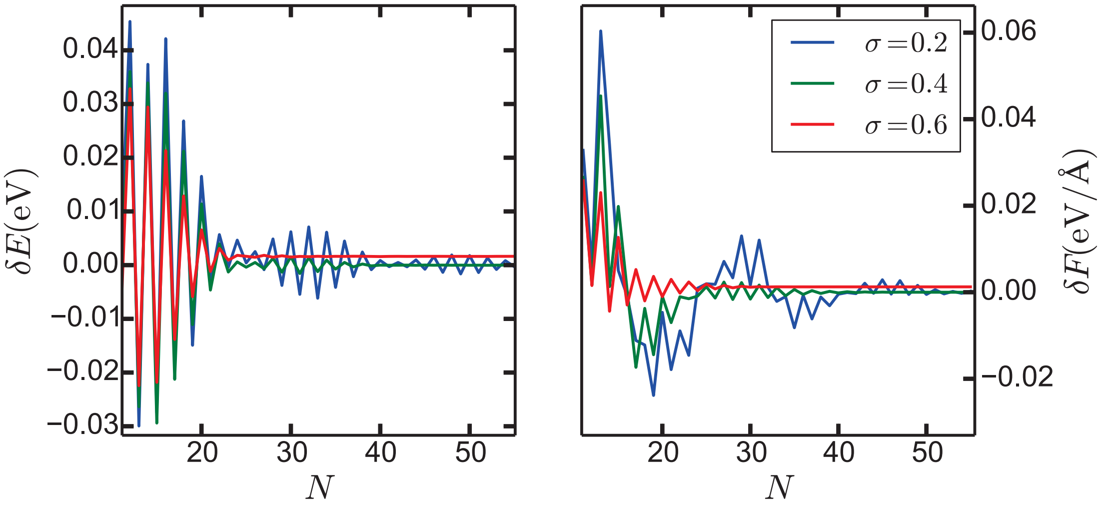

Figure 4.10: Error in energy and forces vs. number of k-points, for several values of the smearing parameter $\sigma$ (in eV). The k-points were chosen from $N \times N$ grids defined according to Eq. (4.26); $N$ is shown on the horizontal axis. The force plotted is the z-component of the force on the atom in the top layer of the slab, with the atoms at their bulk configuration. Plotted is the difference between the energy or force at a given number of k-points, and the energy or force at the most dense k-point grid, $55 \times 55$. These calculations employed an energy cutoff of 400eV.

### K-point Grid

We first consider convergence of the energy and forces with respect to the number of k-points for the primitive Cu(111) surface unit cell. These calculations were done with the PBE functional without vdW corrections, but the conclusions should hold for any of the vdW correction methods used, since it has been found that the inclusion of these corrections has little effect on the electronic structure [62]. Fig. 4.10 shows the energy as a function of the number of k-points for a 3 layer slab. The Brillouin zone integration is performed using the Methfessel-Paxton method [63], for several different smearing widths. A larger smearing width speeds convergence with respect to the number of k-points, but too large a value will give incorrect energies and forces. We find that for a smearing width of 0.4eV, the energy is converged to within 1meV and forces to 5meV/Åfor a 25x25 grid of k-points.

The convergence with respect to the k-point sampling for DTA adsorbed on Cu should behave similarly to pure Cu, since the orbitals associated with the DTA

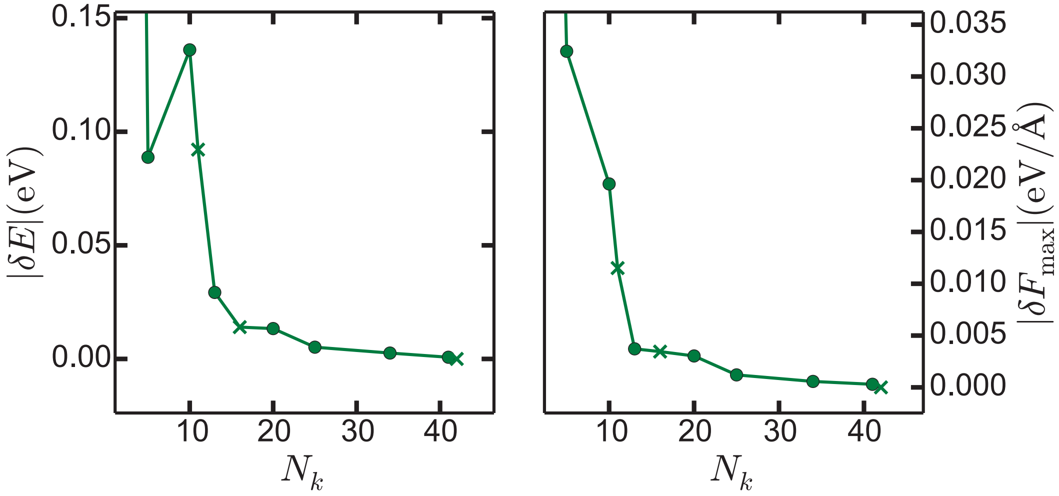

Figure 4.11: Error in energy and forces vs. number of k-points in irreducible Brillouin zone, $N_k$, for the T2 configuration of Fig. 4.3. Circles are for $N \times N$ grids with $N$ from 2 to 9, crosses are for $4\times5$, $5\times6$, and $8\times10$ grids, defined according to Eq. (4.26). The energy error is the difference between the energy at a given number of k-points and the largest number of k-points tested, the $8 \times 10$ grid. The force error is the largest difference in the Cartesian components of the force. These calculations employed an energy cutoff of 400eV and a smearing width of $\sigma = 0.4$eV.

molecule are expected to be well localized around the molecule and not show significant dispersion. The energies and forces for the $5 \times 4$ supercell employed in the previous sections may therefore be expected to be converged for a $5 \times 6$ grid of k-points, corresponding to a $25 \times 24$ grid in the primitive unit cell. From Fig. 4.11, where the error in the energy and force is plotted for the T2 configuration of DTA on Cu(111), it can be seen that this is indeed the case. For a $5 \times 6$ grid of k-points, the energy is converged to within 15meV, and the forces to within 5mev/Å. Since energy differences between different configurations converge faster than the absolute value of the energy, this level of accuracy is sufficient to resolve the small energy differences of interest for the diffusion of DTA, which are on the order of 10meV. It should be noted that this level of accuracy is well below the expected intrinsic error of DFT with respect to experimental values, but is nonetheless required for a self-consistent calculation of the energy barriers.

### Plane Wave Cutoff

For the "standard" cutoff of 400eV for which the pseudopotentials in VASP were designed, the errors in the forces are approximately 0.04eV/Å. To achieve an accuracy better than 0.005meV/Å, an higher energy cutoff of 800eV is required. Calculations at the lower cutoff of 400eV can be used to obtain results that are qualitatively correct, but the noise in the forces means that barriers calculated at this cutoff will not be accurate to within more than approximately 10 $\sim$ 20meV (estimated from the typical change in energy when relaxing a structure from maximum forces of 0.05eV/Å to 0.01eV/Å with an 800eV cutoff). A 400eV cutoff was used to obtain the results in Fig. 4.5 and Table 4.4.

### Size of Supercell

In Table 4.4 we show the results of calculations for larger supercells, in order to ensure that the low-coverage limit has been attained for a $5 \times 4$ supercell. The positions of DTA and the upper two layers of the Cu slab were fully relaxed for the larger supercells so that the maximum force was less than 0.01eV/Å. When going from a $5 \times 4$ cell up to a $7 \times 6$ cell, the energy barriers at the T1 and T2 sites change by less than 10meV (with the exception of the $6 \times 4$ cell, which changes by $\sim$ 20meV). This is less than the expected noise in the energies due to the smaller energy cutoff used, confirming that the $5 \times 4$ supercell is sufficiently large to simulate the low-coverage limit.

Table 4.4 also shows the results of calculations for a larger number of layers. For these calculations the geometry was kept fixed, adding new layers of Cu atoms at their ideal bulk positions. The energies of the T1 and T2 sites are raised slightly when adding more layers, being fully converged by 5 layers. The underestimation of the energies at T1 and T2 for the 3-layer slab, approximately 20 $\sim$ 30meV, is quite small, and only slightly larger than the expected noise in the energies due to the smaller energy cutoff used. For the calculation of the potential energy curve for diffusion, as well as vibration frequencies, we therefore find that it is sufficient to use a $5 \times 4 \times 3$ supercell with a $5 \times 6$ k-point grid and 800eV energy cutoff.

Table 4.4: Energies of the T1 and T2 sites (in meV) relative to M1 using the TS-surf method, for different sized supercells and number of layers. The first two numbers in the "Size of supercell" column give the number of primitive surface unit cells of Cu(111) included in the supercell (with the first number running parallel to the long axis of DTA), and the third number giving the number of layers in the Cu slab. The energy cutoff (in eV) and size of the k-point grid used are also shown.

| Size of supercell | Basis set | $E_{\mathrm{T1}} - E_{\mathrm{M1}}$ | $E_{\mathrm{T2}} - E_{\mathrm{M1}}$ |
|---|---|---|---|
| $5 \times 4 \times 3$ | 400 / $5 \times 6$ | 151 | 72 |
| $5 \times 5 \times 3$ | 400 / $5 \times 5$ | 144 | 61 |
| $6 \times 4 \times 3$ | 400 / $4 \times 6$ | 129 | 56 |
| $6 \times 5 \times 3$ | 400 / $4 \times 5$ | 146 | 63 |
| $7 \times 6 \times 3$ | 400 / $4 \times 4$ | 144 | 69 |
| $5 \times 5 \times 4$ | 400 / $5 \times 5$ | 196 | 91 |
| $5 \times 5 \times 5$ | 400 / $5 \times 5$ | 185 | 87 |
| $5 \times 5 \times 6$ | 400 / $5 \times 5$ | 186 | 86 |
| $5 \times 5 \times 7$ | 400 / $5 \times 5$ | 187 | 87 |

## 4.3 Conclusions

We have seen that, as expected from previous DFT studies of adsorbed organic molecules, including vdW interactions significantly alters the energy profile for diffusion of DTA on Cu(111). The attractive vdW forces between the Cu surface and DTA molecule alter the adsorption geometry, pulling DTA closer to the surface. The extent to which the geometry is affected was seen to vary significantly between the different vdW correction methods tested. The vdW-DF and vdW-DF2 methods gave adsorption geometries with DTA significantly further from the surface than other methods, consistent with the already established overestimation of binding distances observed for these functionals. Three versions of the non-local vdW functional with optimized exchange were also tested, and gave smaller DTA-Cu distances going from optPBE to optb88 to optb86b. The lattice constant for bulk Cu showed the same trend, becoming smaller for optPBE to optb88 to optb86b. The two semi-empirical methods tested gave geometries similar to optb86b.

In general, methods that gave adsorption geometries with smaller DTA-Cu distances also gave a larger energy barrier between the T1 and T2 sites. This is in better agreement with the experimental observation that DTA migrates via jumps spanning the full surface lattice constant, inconsistent with, e.g., the PBE curve of Fig. 4.9, which would predict jumps of half a lattice constant. All methods still, however, predicted the M1/M2 sites to be the global minimum, contradicting the experimental observation that DTA adsorbs parallel the the Cu rows (although another possible explanation for this was suggested via a different interpretation of the STM images). It was found that shortening the empirical cutoff radii for the vdW forces in one of the semi-empirical methods resulted in a slightly smaller DTA-Cu distance, and lowered the energy of the T2 site below M1/M2. This brings the energy curve into excellent agreement with experimental measurements.

The sensitivity of the energy profile for diffusion to the cutoff radii (in the semi-empirical methods) and exchange functional (in the vdW correlation functional methods) highlights the difficulty of obtaining accurate DFT calculations for systems dominated by vdW interactions. DTA on Cu(111) presents a particularly difficult challenge for DFT, since not only are the vdW interactions a significant part of the molecule-surface interactions, but the correct balance between these forces, the Pauli repulsion between the carbon rings and the surface, and the chemical bonding between the S atoms and the surface is crucial in obtaining accurate geometries and energy barriers. Although $C_6$ coefficients for vdW interactions at large separations can be calculated accurately from first principles, an accurate description of the crossover to the short-ranged regime (well described by the GGA) remains a challenge. The barriers were also seen to be quite sensitive to the Cu lattice constant, highlighting the need for an accurate description of solids within any vdW correction scheme that is to be used to study adsorption and surface diffusion.

# Chapter 5

# Diffusion of DTA

In this chapter we make use of the stochastic model derived in Chapter 3 and the DFT calculations performed in Chapter 4 to calculate the diffusion coefficient of DTA on Cu(111).

The starting point for our stochastic model is the set of Langevin equations for the $N$ atoms making up the diffusing molecule. Since the DTA molecule shows unidirectional diffusion along the [110] direction of the surface [5], its position can be specified by a single Cartesian coordinate $x$ giving the centre of mass displacement along this direction. The equations of motion for the molecule are then, as shown in Eq. (3.24),

$$M\ddot{x} = -\frac{\partial V}{\partial x} - \gamma_{xx}\dot{x} - \sum_n \gamma_{xn}\dot{q}_n + f_x(t) \tag{5.1}$$

$$\ddot{q}_n = -\frac{\partial V}{\partial q_n} - \sum_m \gamma_{nm}\dot{q}_m - \gamma_{xn}\dot{x} + f_n(t), \tag{5.2}$$

where $q_n$ are a set of normal mode vibrational coordinates. In Chapter 3 we showed that this set of equations is equivalent to the generalized Langevin equation

$$M\ddot{x} = -\frac{\partial V_a}{\partial x} - \int_0^t dt'\Gamma[x(t), x(t'), t-t']\dot{x}(t') + F(t), \tag{5.3}$$

with the memory function $\Gamma$ as defined in Eq. (B.13).

The adiabatic potential $V_a(x)$ can be calculated in a simple way using DFT, by minimizing the energy at fixed $x$ while allowing all other degrees of freedom to relax. The memory function depends on the vibration frequencies of the molecule as well as a set of coupling constants for each mode, both of which are determined from the second derivatives of the DFT energy.

The memory function also depends on the friction coefficients $\gamma_{nm}$. The friction forces originate from phonon-mediated energy exchange between the solid and adsorbed molecule, and a determination of $\gamma_{nm}$ therefore requires a model for the phonon dynamics of the solid. For this we use the Debye model, and in section 5.2 we show how to to combine this model with DFT calculations to calculate the friction coefficients from first principles. In principle, the phonon frequency spectrum of the solid could also be calculated using DFT, but such a detailed description of phonon dynamics is not necessary for our purposes. The Debye model also gives an accurate description of the low frequency phonons, which are most important in determining the friction coefficient, as will be seen below. In section 5.3 we show the results of calculations of the diffusion coefficient, and compare with experimental results, as well as standard transition state theory.

## 5.1 Adiabatic Potential and Vibration Frequencies

The adiabatic potential is defined by a thermal average over the vibrational degrees of freedom,

$$e^{-V_a(x)/kT} = \int d^n\vec{q} e^{-V(x,\vec{q})/kT}/Z, \tag{5.4}$$

where the vibrational coordinates $\vec{q}$ include both molecular vibrations and surface phonons. In the harmonic approximation, $V_a$ is simply the potential energy evaluated at the equilibrium values of the vibrational coordinates $\vec{q}$ at fixed $x$. We calculate $V_a$ in this approximation, minimizing the energy of the adsorbed DTA molecule at fixed centre of mass $x$ while relaxing all other degrees of freedom for DTA, as well as the first two layers of the three layer slab of Cu(111). The resulting energy curve, shown in Chapter 4 is reproduced in Fig. 5.1. For numerical calculations, the potential $V_a(x)$ (as well as the effective friction $\gamma_{\text{eff}}(x)$) must be interpolated between the calculated points. A cubic spline interpolation [64] was employed for this purpose for the curves shown in Figs. 5.1 and 5.3. This interpolation is not unique, and introduces additional uncertainty into the calculation. However, testing of alternative interpolation methods (including monotonic piecewise cubic polynomials [65] and cubic splines obtained by least square fitting with allowance for error in the data points [64]) found that this uncertainty is small compared to the inherent numerical noise in the DFT calculations, and so cubic spline fits were used throughout for their simplicity.

Both the vibration frequencies $\omega_n$ and $\phi'_n$ are calculated from the second derivatives of the potential energy using DFT. We first calculate the Hessian matrix in

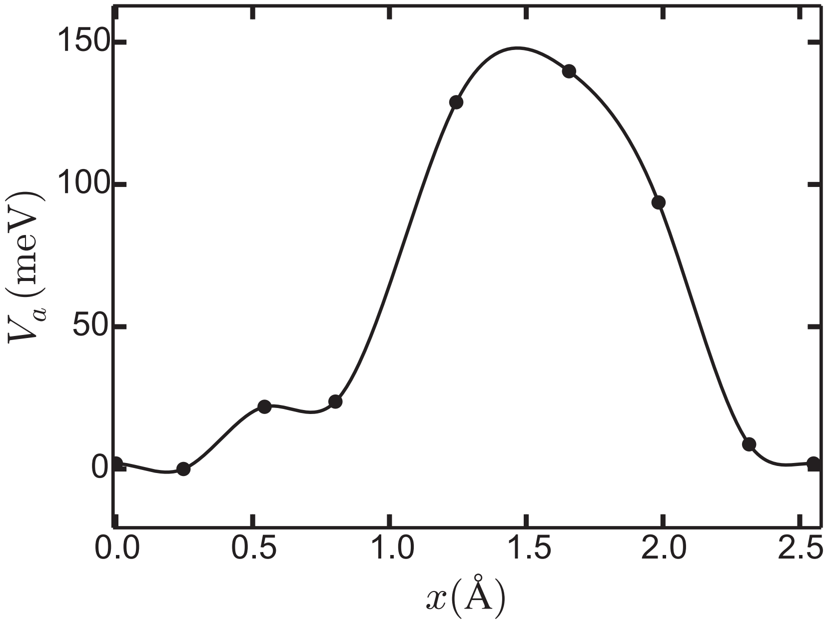

Figure 5.1: Adiabatic potential $V_a$ as a function of centre of mass position of the DTA molecule along the [110] direction of the Cu(111) surface.

Cartesian coordinates $\vec{r}_n$ using a finite difference method. For the TST calculations (discussed below in section 5.3), the vibration frequencies are calculated by diagonalizing this Hessian matrix. To obtain the vibration frequencies at constant center of mass $x$ required for the stochastic model, we make use of the center of mass frame coordinates $\vec{s}_n = \vec{r}_n - \vec{r}_{\text{cm}}$. The Hessian matrix is transformed to a new set of coordinates consisting of the center of mass vector $\vec{r}_{\text{cm}}$ and the collection of $\vec{s}_n$, with one of the $\vec{s}_n$'s being eliminated using $\sum_n m_n \vec{s}_n = 0$. The normal mode eigenvectors and frequencies are then calculated by diagonalizing the sub-matrix of the Hessian excluding the rows and columns containing $x$-derivatives. The constants $\phi'_n = \partial^2 V/\partial x \partial q_n$ are then calculated by projecting these columns onto the normal mode eigenvectors. This method leads to position-dependent $\omega_n(x)$ and $\phi'_n(x)$, which can be calculated at any value of the center of mass $x$; in the following calculations, we will consider the minimum energy configuration and the transition state (sites T1 and T2 of Fig. 4.3).

The frequencies obtained for DTA in its minimum energy configuration using this method are shown in Fig. 5.2. The eight high frequency modes are radial vibrations of the hydrogen atoms, while the lowest frequency modes are frustrated rotations and

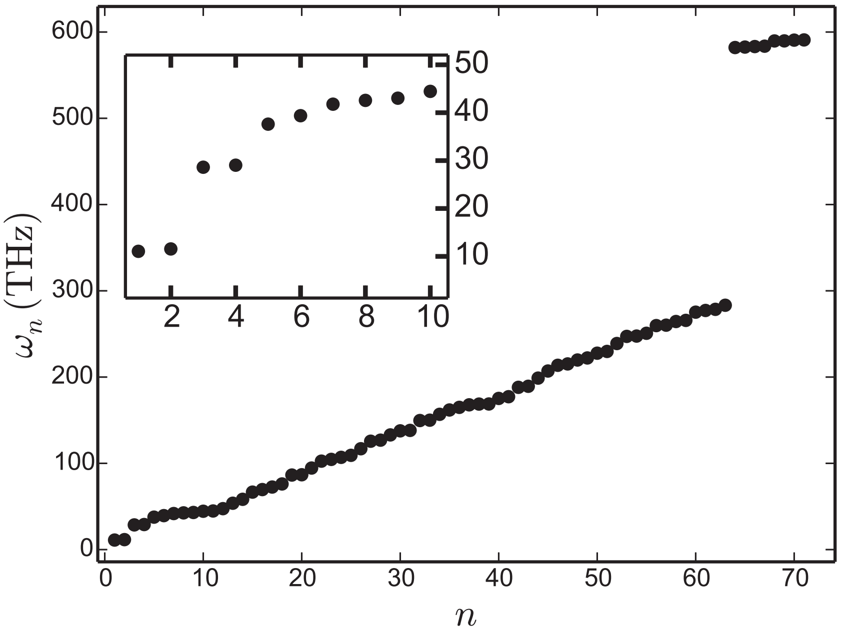

Figure 5.2: Angular vibration frequencies $\omega_n$ for DTA on Cu(111). The inset gives a closer view of the low-frequency modes, which contribute most to the effective friction.

translations. It is these low-frequency modes that give the dominant contribution to the effective friction.

## 5.2 Calculation of Friction

The memory function appearing in the generalized Langevin equation (5.3) depends on the matrix of friction coefficients $\gamma_{mn}$ for the frictional forces between the surface and each atom making up the adsorbed molecule. The memory function has the form $\Gamma = \Gamma_{\mathrm{cm}} + \Gamma_{\mathrm{vib}}$, with the centre-of-mass contribution coming from the corresponding component of the friction matrix,

$$\Gamma_{\mathrm{cm}} = 2\gamma_{xx}\delta(t - t') \tag{5.5}$$

and $\Gamma_{\mathrm{vib}}$ depending on the $\gamma_{xm}$ and $\gamma_{mn}$ components for each vibrational mode.

The matrix of friction coefficients $\gamma_{mn}$ originates from energy exchange between the adsorbed atoms and surface. Below we consider in detail the calculation of the contribution to $\gamma_{mn}$ from surface phonons. For a single adsorbed atom, the phononic friction coefficient takes a simple form that depends only on the adiabatic potential and the Debye frequency of the solid [15, 16]. We will show below that this form underestimates the friction for a large molecule, by comparison with a calculation of $\gamma_{mn}$ from a full consideration of the molecule-surface forces.

We also note that for diffusion at metal surfaces, excitation of electron-hole pairs can also be an important source of energy exchange. Such effects can be included in the present approach by a semi-classical scheme [66, 67] in which the electron-hole pairs give rise to a second contribution to the friction coefficient. In a DFT framework, this results in the expression [68]

$$\gamma_{\mathrm{elec}} = 2\pi\hbar \sum_{\vec{k},n} \sum_{\vec{k}',n'} \left| \left\langle \psi_{\vec{k},n} \right| \frac{\partial V_{\mathrm{KS}}}{\partial x} \left| \psi_{\vec{k}',n'} \right\rangle \right|^2 \delta(\epsilon_f - \epsilon_{\vec{k},n}) \delta(\epsilon_f - \epsilon_{\vec{k}',n'}), \tag{5.6}$$

where $V_{\mathrm{KS}}$ is the Kohn-Sham potential, and $\psi_{\vec{k},n}$ and $\epsilon_{\vec{k},n}$ are the corresponding Kohn-Sham orbitals and eigenvalues at the Fermi level $\epsilon_f$. Previous studies employing this approach have found $\gamma/M \approx 1\mathrm{THz}$ for both hydrogen [68] and carbon monoxide [69] above copper surfaces. Since this is an order of magnitude lower than the phonon-mediated friction coefficients calculated below, we ignore the effect of electronic friction in diffusion calculations. Qualitatively, the effect would be a small increase in the friction, and a corresponding small decrease in the diffusion coefficient.

If the matrix of friction coefficients $\gamma_{mn}$ contains off-diagonal elements, it represents a generalized friction force that is not antiparallel to the velocity vector. Although coupling to phonons generally leads to non-zero off-diagonal elements in $\gamma_{mn}$, these are usually assumed to be zero in practice. In fact, it is typically assumed that $\gamma_{mn}$ is proportional to the identity matrix, i.e. that the friction force is given by $\vec{F}_{\mathrm{fric}} = -\gamma\vec{v}$, where $\gamma$ is a single constant. We therefore also investigate the effect of off-diagonal elements in $\gamma_{mn}$ on the effective friction coefficient for center of mass diffusion.

We finally consider some issues related to the vibrational part of the memory function, including which particular modes give the largest contribution, and the importance of memory effects for the description of diffusion.

### 5.2.1 Phonon-Mediated Friction Coefficients

In general, the equations of motion for the molecule (5.1) will contain a non-Markovian friction term (as in Eq. (2.13)), with a corresponding memory function with components $\Gamma_{mn}(t)$. When the vibrations in the solid are treated in the harmonic approximation, the components of $\Gamma_{mn}$ are given by [15, 21]

$$\Gamma_{mn} = \sum_{ij} \frac{\partial \vec{F}_i^{(s)}}{\partial q_m} \cdot C(R_{ij}, t) \cdot \frac{\partial \vec{F}_j^{(s)}}{\partial q_n}, \tag{5.7}$$

where $C(R_{ij}, t)$ is the correlation function for the displacements $\vec{u}_i$ of the substrate atoms at lattice positions $\vec{R}_i$ and $\vec{R}_j$,

$$C(R_{ij}, t) = \frac{1}{kT} \left\langle \vec{u}_i(t)\vec{u}_j(0) \right\rangle . \tag{5.8}$$

In the Markov approximation, $\Gamma_{mn}$ is replaced with its time integrated value

$$\begin{aligned} \gamma_{mn} &= \int_0^\infty dt \Gamma_{mn}(t) = \sum_{ij} \frac{\partial \vec{F}_i^{(s)}}{\partial q_m} \cdot \bar{C}(R_{ij}) \cdot \frac{\partial \vec{F}_j^{(s)}}{\partial q_n}, \\ \bar{C}(R_{ij}) &\equiv \int_0^\infty dt C(R_{ij}, t) \end{aligned} \tag{5.9}$$

and the Langevin equations (5.1) are recovered. In the harmonic approximation employed in Eq. (5.9), the integrated correlation functions $\bar{C}(R_{ij})$ are independent of the separation of the two atoms $R_{ij}$. This can be seen by expanding $C(R_{ij}, t)$ in terms of phonon modes, in which the displacements $\vec{u}_i$ are given by [70]

$$\vec{u}_i(t) = \sum_{\vec{k},j} Q_{\vec{k},j} \hat{v}_{\vec{k},j} e^{-i\vec{k}\cdot(\vec{R}_i - \omega_{\vec{k},j} t)}, \tag{5.10}$$

where $\hat{v}_{\vec{k},j}$ is the polarization vector for the $j$th vibrational mode at wave vector $\vec{k}$ with frequency $\omega_{\vec{k},j}$, and $Q_{\vec{k},j}$ are the normal mode amplitudes. Using the fact that $\left\langle Q_{\vec{k},j} Q_{\vec{k}',j'} \right\rangle = \frac{kT}{\omega^2_{\vec{k},j}} \delta_{j,j'} \delta_{\vec{k},-\vec{k}'}$ [70], the correlation functions become

$$C(R_{ij}, t) = \sum_{\vec{k},j} \frac{\cos(\omega_{\vec{k},j} t)}{m_s \omega^2_{\vec{k},j}} e^{i\vec{k}\cdot(\vec{R}_i - \vec{R}_j)} \hat{v}_{\vec{k},j} \hat{v}^*_{\vec{k},j}. \tag{5.11}$$

When integrating over time, the cosine term becomes

$$\int_0^\infty dt \cos(\omega_{\vec{k},j} t) = \lim_{t\to\infty} \frac{\sin(\omega_{\vec{k},j} t)}{\omega_{\vec{k},j}} = \pi\delta(\omega_{\vec{k},j}), \tag{5.12}$$

leading to the $R_{ij}$-independent value

$$\bar{C}(R_{ij}) = \lim_{\omega \to 0} \sum_j \frac{\pi g_j(\omega)}{2m_s\omega^2} \hat{v}_{0,j}\hat{v}^*_{0,j} \equiv \bar{C}_0, \tag{5.13}$$

in terms of the vibrational density of states $g_j(\omega)$ for each mode. Note that $\bar{C}(R_{ij})$, and therefore the friction coefficients $\gamma_{mn}$, depend only on the zero-frequency limit of the phonon frequency spectrum. This is a justification for using the Debye model for the phonon dynamics of the solid, since it accurately represents the low-frequency part of the vibrational density of states, only becoming inaccurate near the edge of the Brillouin zone where the dispersion deviates from the linear relationship $\omega_{\vec{k},j} = c|\vec{k}|$. In the bulk Debye model, $\bar{C}_0$ takes the value [15]

$$\bar{C}_0 = \frac{3\pi}{2m_s\omega_D^3} I, \tag{5.14}$$

where $m_s$ is the mass of the substrate atoms, $\omega_D$ is the Debye frequency of the substrate, and $I$ is the identity matrix. It has been found that accounting for the modified vibrational density of states near a surface by employing a surface Debye model leads to a value for $\bar{C}_0$ that is larger than the bulk value by approximately a factor of two [71, 72]. For simplicity, we therefore use Eq. (5.14) multiplied by this factor in calculations of $\gamma_{mn}$.

With $\bar{C}(R_{ij}) = \bar{C}_0$, the sums over $i$ and $j$ in Eq. (5.9) can be performed, giving $\sum_i \vec{F}_i^{(s)} = -\sum_i \vec{F}_i^{(a)} = -\vec{F}_{\text{cm}}$, where $\vec{F}_i^{(a)}$ is the force on the $i$th atom of the molecule, and we have defined $\vec{F}_{\text{cm}}$ to be the total force on the molecule. For a single atom in one dimension, this results in the simple expression

$$\gamma = \bar{C}_0 \left( \frac{\partial^2 V}{\partial x^2} \right)^2 . \tag{5.15}$$

This expression is convenient in that it only depends on the potential energy of the diffusing atom $V(x)$, the influence of the substrate being completely contained in the constant factor $\bar{C}_0$, which for a simple solid can easily be estimated from bulk properties according to Eq. (5.14).

For a molecule it is tempting to generalize Eq. (5.15) to a corresponding expression for the effective friction, by replacing $V$ with the adiabatic potential $V_a(x)$. The center of mass contribution is in fact given by a similar expression,

$$\gamma_{xx} = \bar{C}_0 \left| \frac{\partial \vec{F}_{\text{cm}}}{\partial x} \right|^2_{\vec{q}=\vec{q}_0} . \tag{5.16}$$

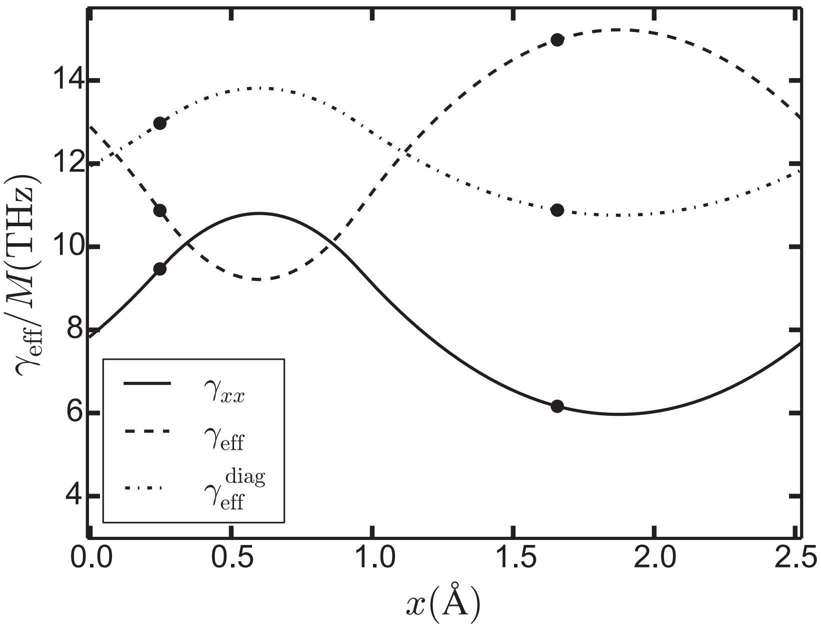

Figure 5.3: Effective friction coefficient $\gamma_{\mathrm{eff}}$ for DTA on Cu(111) in the Markov approximation. The center of mass contribution $\gamma_{xx}$ is shown separately, as well as the effective friction calculated using only the diagonal elements of $\gamma_{mn}$.

Although this contains the forces on the molecule in all three Cartesian directions, it might be assumed that they are approximately equal in magnitude, and using the form Eq. (5.15) will be a reasonable approximation. However, contributions from the vibrational degrees of freedom will raise the effective friction coefficient, and may also introduce memory effects. We therefore calculate $\gamma_{mn}$ from the full expression Eq. (5.9), using the forces on substrate atoms $\vec{F}_i$ calculated from DFT. We will now consider the influence of the molecular vibrations on the effective friction.

### 5.2.2 Influence of Molecular Vibrations

To see the effect of the molecular vibrations on the effective friction, we first consider the Markov approximation, in which $\gamma_{\mathrm{eff}} = \gamma_{xx} + \gamma_{\mathrm{vib}}$. As shown in Chapter 3, the vibrational contribution $\gamma_{\mathrm{vib}}$ is given by

$$\gamma_{\mathrm{vib}} = \sum_{m,n} \gamma_{mn} \frac{\phi'_m}{\omega_m^2} \frac{\phi'_n}{\omega_n^2} - 2 \sum_m \gamma_{rm} \frac{\phi'_m}{\omega_m^2}, \tag{5.17}$$

with the friction coefficients $\gamma_{mn}$ calculated from Eq. (5.9). Second derivatives of the energy, calculated here using DFT, determine the $\partial\vec{F}_i/\partial q_n$ appearing in Eq. (5.9), as well as the vibration frequencies $\omega_m$ and the $\phi'_m = \partial^2 V/\partial x \partial q_m$. A specification of the vibrational properties of the solid, through Eq. (5.14) then completes the description of phonon-mediated friction.

Fig. 5.3 shows the friction coefficient calculated using this method for DTA on Cu(111), using the configurations at the minimum and transition state of the potential energy curve shown in Fig. 5.1 (the T1 and T2 sites shown in Fig. 4.3). Since the derivation of the effective friction coefficient in Chapter 3 assumes constant friction coefficients $\gamma_{mn}$ for the vibrational degrees of freedom, but using Eq.(5.9) results in position-dependent $\gamma_{mn}$, we therefore take the average value of the $\gamma_{mn}$'s calculated at the T1 and T2 configurations. For comparison, both the total effective friction $\gamma_{\text{eff}}$, and the center of mass contribution $\gamma_{xx}$ alone are shown in Fig. 5.3. Note that the inclusion of the vibrational contribution $\gamma_{\text{vib}}$ raises the effective friction coefficient by approximately 50% on average. Calculating $\gamma_{\text{eff}}$ from the single-atom expression (5.15) will therefore lead to an underestimation of the friction.

To investigate the importance of the off-diagonal components of $\gamma_{mn}$, we also plot in Fig. 5.3 the effective friction calculated setting $\gamma_{mn} = 0$ for $m \neq n$. Note that, although the position-dependence of $\gamma_{\text{eff}}$ is affected by ignoring the off-diagonal components, the average value is nearly the same, changing by less than 10%. For this system, the off-diagonal components will therefore have little effect on the diffusive motion of the molecule, and we ignore them in further calculations (the possible impact of off-diagonal components for larger molecules is discussed further below). This is especially useful when considering memory effects, since $\Gamma_{\text{vib}}$ can then be calculated using the simpler expression Eq. (3.27), rather than the more general Eq. (B.13).

Another important consideration is the accuracy of the classical treatment of the vibrational motion. At the low temperatures for which the STM observations of DTA diffusion on Cu(111) were performed, the high frequency molecular vibrations seen in Fig. 5.2 will be confined to the ground state, since $kT \ll \hbar\omega$. To see the influence of these degrees of freedom on the effective friction, Fig. 5.4 shows the quantity $\phi'_n/\omega_n^2$, which determines the contribution of each mode to $\gamma_{\text{vib}}$. It can be seen that only

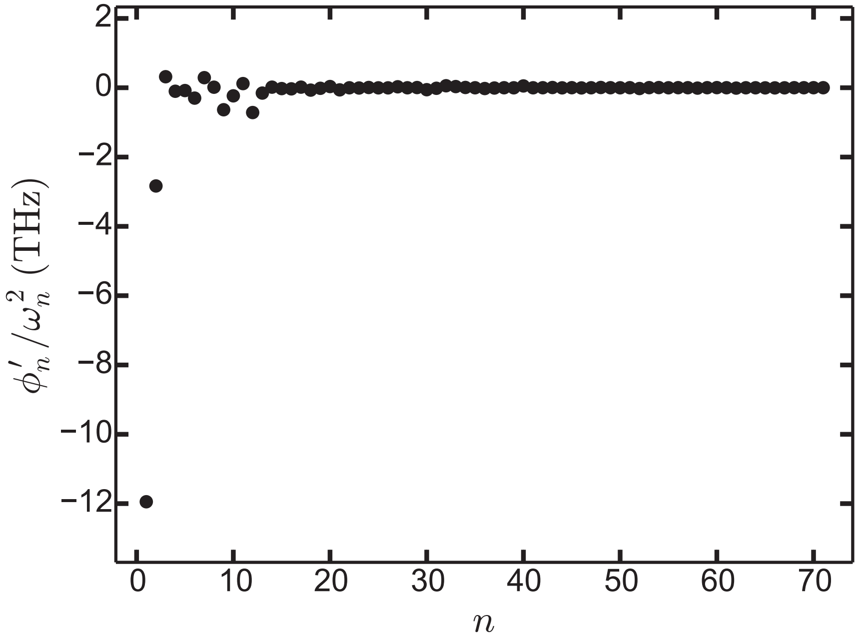

Figure 5.4: Coupling constants $\phi'_n/\omega_n^2$ contributing to the effective friction through Eq. (5.17).

the two lowest frequency modes give any significant contribution to $\gamma_{\text{vib}}$, confirming that there is no unphysical energy transfer to the high-frequency vibrational modes at low temperatures. The lowest frequency mode is a rotation of DTA in the plane of the surface, while the second lowest frequency mode is overall translation along the surface, perpendicular to the [110] rows. Both of these modes have $\hbar\omega \approx kT$ for the experimental temperature range of $T = 55\text{K} \sim 65\text{K}$.

### 5.2.3 Memory Effects

The influence of memory effects in $\Gamma_{\text{vib}}$ can be estimated from the Grote-Hynes approximation, in which the escape rate of the molecule from the potential well is determined by the Laplace transform of the memory function $\hat{\Gamma}(\lambda)$ at a frequency determined by the equation

$$\lambda = \frac{\omega_b^2}{\lambda + \hat{\Gamma}(\lambda)/M}, \tag{5.18}$$

with $\omega_b$ being the unstable (imaginary) frequency at the top of the barrier between two sites.

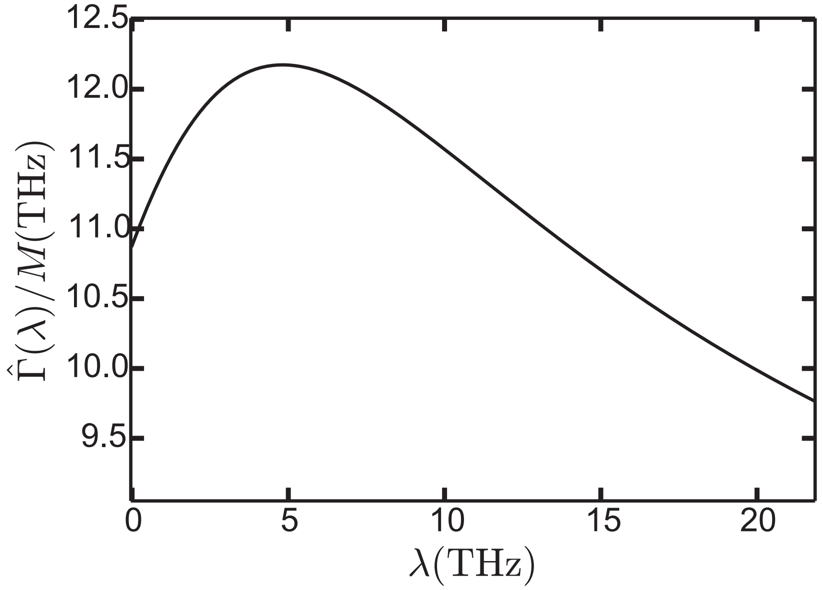

Figure 5.5: Laplace transform of vibrational contribution to the memory function $\Gamma_{\text{vib}}$.

Fig. 5.5 shows $\hat{\Gamma}(\lambda)$ for DTA on Cu(111), calculated from Eq. (3.27). The escape rate (and consequently the diffusion coefficient) is determined by $\hat{\Gamma}(\lambda)$ at $\lambda \lesssim \omega_b$. Due to the flat shape of the adiabatic potential in the barrier region (see Fig. 5.1), the barrier frequency is quite small, $\omega_b \approx 2$THz. It can be seen from Fig. 5.5 that $\hat{\Gamma}(\lambda)$ is already very close to its zero-frequency limit for $\lambda \lesssim \omega_b$, and so memory effects will not have a significant effect on the diffusion coefficient.

### 5.2.4 Off-Diagonal Friction Components

For a large molecule, off diagonal terms in $\gamma_{mn}$ coupling together different modes that are well separated spatially seems physically unreasonable. However, since $\bar{C}(R_{ij})$ does not decrease with the distance between two substrate atoms, Eq. (5.9) predicts that there will be no decrease in magnitude for the $\gamma_{mn}$ components between two well-separated modes. This is in fact an artifact of the Markov approximation.

Although the time-integrated correlation function has the same value $\bar{C}(R_{ij}) = \bar{C}_0$ regardless of the separation $R_{ij}$, the time required for $\bar{C}(R_{ij})$ to approach this value increases as the separation of the atoms increases, taking on the order of $R_{ij}/c$, where $c$ is the sound speed in the solid. The Markov approximation is then only reasonable if this time is short compared to the timescale for motion of the adsorbate. The largest separations $R_{ij}$ that must be considered are approximately the size of the adsorbed molecule, in which case $R_{ij}/c$ is simply the time required for a lattice vibration to travel across the area of the molecule. In other words, if the time required for a phonon to traverse the adsorbed molecule is not short compared to the time scale of interest, then the Markov approximation cannot be used to describe phonon-mediated friction. For DTA on Cu(111), DFT predicts a vibration period for center of mass motion of $\tau_{\text{vib}} \approx 1\text{ps}$, while $R_{ij}/c \approx 0.2\text{ps}$. DTA is therefore small enough for the Markov approximation to be reasonable for calculating the elements of $\gamma_{mn}$.

For a larger molecule, memory effects can be taken into account by the Grote-Hynes formula, Eq. (5.18). The effective friction is then determined from Eq. (5.9), with the zero-frequency value $\bar{C}(R_{ij}) = \hat{C}(R_{ij}, \lambda)|_{\lambda=0}$ replaced by $\hat{C}(R_{ij}, \lambda)$, with $\lambda$ on the order of a typical vibration frequency for the molecule. Fig. 5.6 shows the Laplace transform of $C(R_{ij}, t)$ evaluated in the Debye model, for several values of $R_{ij}$. It can be seen that although $\hat{C}(R_{ij}, \lambda)$ has the same zero-frequency limit for any $R_{ij}$, it quickly tends to zero for finite $\lambda$ when the separation $R_{ij}$ becomes large. For a large molecule, this will have the effect of decreasing the off-diagonal elements of $\gamma_{mn}$ for well-separated modes, as expected.

## 5.3 Diffusion Coefficient

Making use of the calculations of the adiabatic potential $V_a(x)$ and effective friction coefficient $\gamma_{\text{eff}}$ shown in the previous sections, the Langevin equation (5.3) can now be solved to calculate the diffusion coefficient of DTA on Cu(111), using the method detailed in Chapter 2. In order to compare with experimental measurements, we consider the site-to-site jump rate $\kappa$, related to the tracer diffusion coefficient by $D_t = \frac{1}{2}\kappa \langle l^2 \rangle$. Since long jumps are not significant in this system, the mean square jump length $\langle l^2 \rangle$ is simply the surface lattice constant $a^2$.

Fig. 5.7 shows the jump rate as a function of inverse temperature, in the low temperature regime of experimental interest, with experimental data shown for comparison. At low temperatures, the rate obeys the Arrhenius law $\kappa = \kappa_0 e^{-\Delta V/kT}$, where $\Delta V$ is the energy barrier between sites. The rate only deviates from this behavior when $kT \gtrsim \Delta V$, which for this system corresponds to $T \gtrsim 1500\text{K}$. At the

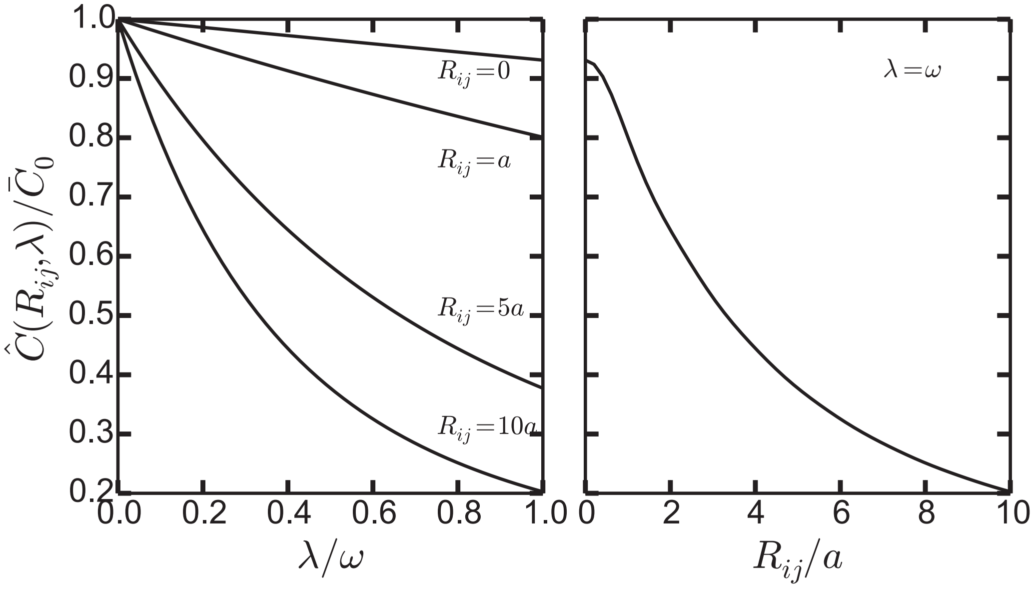

Figure 5.6: The left panel shows the Laplace transform of the correlation function $C(R_{ij},t)$, evaluated for separations $R_{ij}$ of 0,1,5, and 10 lattice constants. $\hat{C}$ was calculated in the bulk Debye model, and the x-axis is scaled by a typical vibration frequency for DTA on Cu(111), $\omega \approx \omega_D/10$. The right panel shows $\hat{C}$ evaluated at $\lambda = \omega$, as a function of separation $R_{ij}$

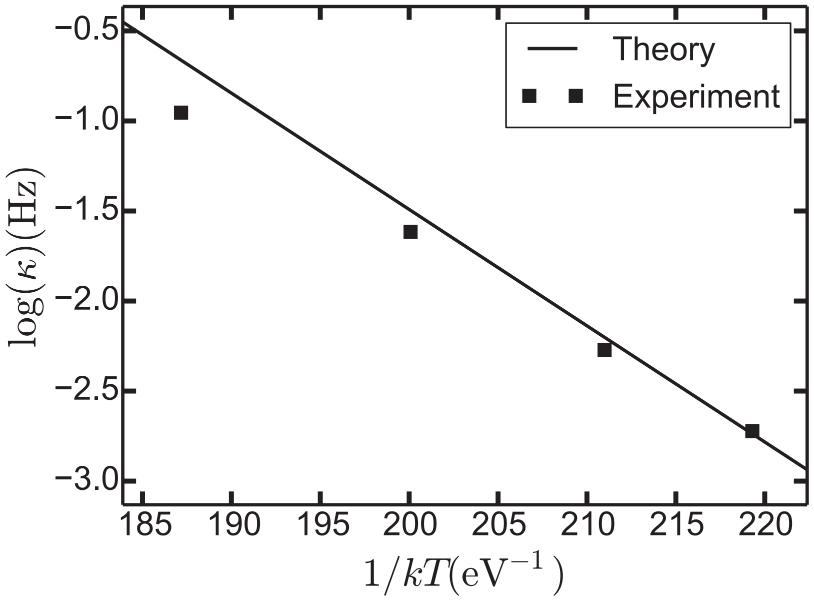

Figure 5.7: Arrhenius plot of the jump rate calculated in the stochastic model, compared with experimental data from Ref. [5].

experimental temperatures of 55 $\sim$ 65K, the rate is therefore predicted be very well described by an Arrhenius law.

The rate prefactor $\kappa_0$ and barrier $\Delta V$ can be calculated by Arrhenius fits as discussed in Chapter 3. The barrier calculated in this way is equal to the static energy barrier calculated from DFT, $\Delta V = 145$meV, very close to the measured barrier of $\Delta V = 130$meV. Calculating an accurate prefactor is much more challenging, and its value is strongly affected by the strength of the frictional damping, in contrast to the barrier. We find a prefactor of $\kappa_0 = 0.27$THz, with consideration of memory effects leading to a reduction of less than 5%.

For comparison, we also consider a calculation of the prefactor by transition state theory (TST),

$$\kappa_{0,\mathrm{TST}} = 2\frac{kT}{h}\frac{Z_b}{Z_m} \approx \frac{1}{\pi}\frac{\prod_i \omega_{m,i}}{\prod_i \omega_{b,i}}, \tag{5.19}$$

where $Z_b$ and $Z_m$ are the vibrational partition functions at the barrier and minimum energy configurations. The right hand side gives the approximation in terms of the harmonic vibration frequencies $\omega_{b,i}$ and $\omega_{m,i}$ at the barrier and minimum (a factor of 2 is included in $\kappa_{0,\mathrm{TST}}$ to account for the two possible jump directions). Due to its simplicity, the harmonic approximation to TST is widely employed in rate calculations. For the present system, it gives a prefactor of $\kappa_{0,\mathrm{TST}} = 3.4\mathrm{THz}$.

The measured value of the rate prefactor was $\kappa_0 = 0.004\mathrm{THz}$. Although the prefactors calculated within our stochastic model are still larger than the experimental value, they are nevertheless an order of magnitude closer than the TST estimate. The overall jump rate $\kappa$ also compares quite well with measured values, as seen in Fig. 5.7. Barring a large difference in vibrational entropy between the minimum and transition state, TST gives a prefactor that is on the order of a typical vibrational frequency for the center of mass motion of the molecule, while the experimental prefactor is much lower. Our stochastic model shows the correct trend of a prefactor that is lowered compared to the molecular vibration frequencies, although the reduction is not as dramatic as what is observed experimentally.

There are several factors that can affect the quantitative accuracy of the rate calculation, including inaccuracies in the DFT calculations, anharmonic effects in the molecular vibrations and phonons, and quantum effects. The most important factor is the accuracy of the DFT calculations in determining the adiabatic potential. In the low temperature limit, the rate in the stochastic theory can be written as $\kappa_0 = k_\gamma \nu_{\mathrm{eff}}$, where $\nu_{\mathrm{eff}}$ is a TST-type effective vibration frequency in the well of the adiabatic potential, and $k_\gamma$ is a factor that depends on the friction [73]. The shape of the adiabatic potential near the minimum strongly affects $\nu_{\mathrm{eff}}$, and can cause significant changes in the prefactor.

In the harmonic approximation, $\nu_{\mathrm{eff}}$ is equal to the harmonic vibration frequency at the bottom of the potential well; more generally, it is related to the vibrational partition function, $\nu_{\mathrm{eff}} = 2\frac{kT}{h}\frac{1}{Z}$. The difference between this factor and the TST prefactor in Eq. (5.19) is that the partition function can be calculated using the full $V_a(x)$ curve, and therefore include anharmonic effects in the center of mass motion (while other molecular degrees of freedom are treated in the harmonic approximation). In the present system, this has the effect of lowering the effective vibration frequency $\nu_{\mathrm{eff}}$, due to the flat shape of the potential well. An estimate of a lower bound on $\nu_{\mathrm{eff}}$ can be obtained by assuming a completely flat potential well, leading to $\nu_{\mathrm{eff}} = \sqrt{\frac{kT}{2\pi M a^2}} \approx 0.16\mathrm{THz}$, while the present calculations give $\nu_{\mathrm{eff}} \approx 0.80\mathrm{THz}$. An adiabatic potential with a flatter potential well might therefore lower the prefactor by a factor of 5.

The factor $k_\gamma$ causes a reduction in the rate, accounting for the effects of recrossing at the barrier, and our model gives $k_\gamma \approx 0.3$ for the present system. With a flat potential, our model would then predict a prefactor of $\kappa_0 \approx 0.025$THz, quite close to the experimental value. A higher friction coefficient from coupling to electronic excitations would further lower the prefactor.

## 5.4 Conclusions

We have shown that our stochastic model of diffusion gives a fundamentally improved description of the jump rate for DTA diffusing on Cu(111) compared to TST, bringing it into near quantitative agreement with experiment. The rate prefactor in this system is unexpectedly low, being several orders of magnitude smaller than the lowest molecular vibration frequencies. In our approach, this lowering of the prefactor is seen to result from the anharmonicity of the flat-bottomed potential well, as well as frictional damping. This damping alters the dynamics of the diffusing molecule near the barrier region, making recrossings significant, and lowers the prefactor in this case by a factor of $k_\gamma \approx 0.3$.

Our approach includes the influence of the internal molecular degrees of freedom on the frictional damping of center of mass motion. For the system considered here, this leads to a increase of approximately 50% in the friction coefficient, with a corresponding decrease in the prefactor. This increase in the effective friction will be significant whenever there is significant coupling between the center of mass motion of a molecule and one or more of its internal degrees of freedom. As discussed in Chapter 3, in the Markov approximation this leads to an increase in the effective friction whenever the lowest energy path across the surface is significantly curved through the coordinate space. In other words, when there is concerted motion of the center of mass and other degrees of freedom as the molecule crosses the barrier. For DTA, there is concerted motion of the center of mass and rotational motion as the molecule pivots across the transition state, with one of its S atoms fixed near a bridge site.

When there is such coupling to an internal mode with a vibrational frequency that is slow compared to center of mass motion, memory effects will be significant.

This results in a renormalization of the friction to the Laplace-transformed memory function $\hat{\Gamma}(\lambda)$ at an appropriate frequency, which can result in a friction considerably different from the zero-frequency Markov approximation. Such a situation could conceivably arise for, e.g., a long molecule anchored to a substrate at one end, with the other end extending freely from the surface. In that case one would expect low frequency modes associated with rocking motion of the free end, which may be slow compared to motion at the anchored end.

This calculation also highlights the inherent difficulty in calculating quantitatively accurate rate prefactors. As pointed out above, the prefactor is highly sensitive to the shape of the potential energy curve. Calculating such an energy curve from first principles with sufficient accuracy is challenging, particularly for organic molecules adsorbed at surfaces, where the inclusion of van der Waals forces in a DFT framework is problematic. Nevertheless, we find that the consideration of energy exchange processes between the surface and adsorbed molecule leads to a qualitative improvement over TST, and overall reasonable agreement with experiment.

# Chapter 6

# Conclusions

In this thesis we have presented a theoretical framework for the study of surface diffusion of organic molecules. Our approach is based on the generalized Langevin equation, in which the equations of motion for the $N$-body system consisting of the molecule and substrate are simplified by singling out the centre of mass coordinate of the diffusing molecule for explicit consideration. The influences of the remaining degrees of freedom becomes a fluctuating force and dissipative force term acting on the centre of mass. We have shown how to properly apply this formalism to a molecule of arbitrary size with internal vibrational and rotational degrees of freedom.

For molecules, the stochastic and dissipative forces entering the Langevin equation must account for energy exchange not only with surface phonons, but also between the centre of mass motion of the molecule and its internal degrees of freedom. We have seen that the nature of this energy exchange can be qualitatively different from the phonon-mediated frictional forces usually employed in the Langevin approach for molecules with "soft" vibrational modes. If some modes have frequencies on the same order as, or smaller than those associated with centre of mass displacement, the Markov approximation appropriate for phonon-mediated forces can become inaccurate.

We first applied this approach to a simple model system consisting of a dimer in a one-dimensional periodic potential. The benefit of studying a model such as this is twofold: first of all, the simplicity allows for a systematic investigation of how centre of mass transport of a molecule can be affected by its internal degrees of freedom. For the dimer, the most important feature is the vibration frequency of its internal mode. We showed in Chapter 3 that when this is on the same order as or smaller than the frequency for centre of mass motion, the diffusion coefficient can be significantly altered, and that this effect is stronger for molecules with more vibrational modes, see Fig. 3.9. This suggests that for large planar molecules, which will always have "soft" vibration modes associated with long-range bending and twisting motion, accounting for the effect of molecular vibrations on the centre of mass dynamics is important.

The second benefit of studying the one-dimensional dimer is that for a low dimension system such as this, the dynamics can be solved exactly in the full configuration space of the molecule. This allows us to test the accuracy of the stochastic approach (already well established for phonon-mediated diffusion) for the treatment of coupling to internal molecular degrees of freedom. Good agreement between the stochastic model and exact results was found.

In the second part of the thesis we applied the formalism developed in Chapters 3 and 2 to calculate the diffusion coefficient in a system of experimental interest. We chose dithioanthracene adsorbed on Cu(111) as a test case for our model due to the availability of experimental data for the diffusion rate, as well as the relatively small size of the molecule. The modest size made it feasible to calculate the necessary input parameters for the stochastic model (potential energy curve and vibration frequencies) from first principles using density functional theory.

It was found that the qualitative predictions from the one dimensional dimer calculations were borne out in these detailed calculations for a real system. The diffusion coefficient was seen to be lowered as a result of contributions to the effective friction from coupling of the centre of mass motion to frustrated rotational and translational modes. Memory effects were found to not be significant in this system, but it was also pointed out how they could be important for a larger molecule.

During the course of the density functional theory calculations, we also investigated some issues related to the accuracy of various methods designed to add van der Waals type interactions to DFT. It has been noticed before that standard GGA functionals fail to adequately describe interactions between organic molecules and metal surfaces, and we observed the same trend in our calculations. At the GGA level, DFT incorrectly predicted the stable adsorption geometry, and in fact predicted a negligible energy difference between the experimental minimum energy configuration and the transition state. Including van der Waals corrections by several different methods produced generally better agreement with experiment, but still predicted the experimental minimum energy configuration to be unstable (although a possible alternative way to reconcile these calculations with experiment through a re-interpretation of the

STM images was noted).

We found that by adjusting the empirical cutoff radius scaling factor in one of the van der Waals correction methods, better agreement of both the adsorption geometry and energy barrier with experiment could be obtained. The sensitive dependence of the relative stability of different adsorption sites on the cutoff of the van der Waals forces at short interatomic distances was interpreted as being a result of competition between van der Waals type and chemical bonding type forces. This sensitivity of an experimentally observable quantity (namely the adsorption geometry) to the short range crossover from van der Waals attraction to Pauli repulsion, as well as the anomalously low diffusion prefactor makes dithioanthracene on Cu(111) a particularly interesting system, as it appears to provide a stringent test of both van der Waals correction methods in DFT, as well as statistical mechanics methods for calculating rate prefactors.

Overall, good agreement was found between the predictions of our stochastic model and experimental measurements for the diffusion rate of DTA. Moreover, it was shown that this model is capable of capturing important physics relevant to the diffusion of large molecules that is missing in transition state theory as well as the usual Markovian Langevin equation based approaches.

## 6.1 Future Work

Due to the possible relevance of memory effects for large molecules, an important direction for future work on this approach is a more adequate method for the solution of the generalized Langevin equation with a non-Markovian friction kernel. In the present work, the effect of memory on the diffusion coefficient was estimated by the Grote-Hynes approximation. This approximation is, however not valid in the underdamped regime in which long jumps spanning multiple lattice sites can occur. Such long jumps have been observed before in the surface diffusion of large molecules [13], and so an application of our model to such systems demands a more general treatment of memory effects. The Grote-Hynes formula for the escape rate also relies on a harmonic approximation to the adiabatic potential in the barrier region, which could be a source of inaccuracy for systems with highly anharmonic potentials.

A full solution of the generalized Fokker-Planck equation shown in Eq. (2.36) is quite demanding due to its non-linear nature. Applying a method similar to the one described in Chapter 2 for the Markovian Fokker-Planck equation would require a self-consistent loop to treat the non-linear memory term. For one-dimensional diffusion this approach is however possible due to the efficiency of the matrix continued fraction method. A single calculation of the diffusion coefficient takes only a few seconds on a standard PC, and so a self consistent solution of Eq. (2.36) seems feasible. For surface diffusion in two dimensions, a different approach would likely be required.

Another weakness of the approach used here that can be easily addressed is the calculation of the adiabatic potential in the harmonic approximation. This approximation fails in systems with a significant difference in vibrational entropy between the minimum and transition state, as seen in Chapter 2. Although no such entropy difference was seen for DTA, it could be relevant in other systems. For example, this effect was used to explain large differences in the diffusion prefactors between monomers and dimers of porphyrin molecules on a copper surface [6]. Within a DFT framework, such anharmonic contributions to the adiabatic potential could be calculated using umbrella sampling [74], among other methods.

Extending the stochastic model of surface diffusion in these ways will allow for an accurate calculation of diffusion coefficients and jump rates in a very general class of systems. These jump rates can then be used as input for a lattice gas model, as outlined in Chapter 1. In this approach, the physics of adsorbed organic molecules can be modelled from first principles over the whole range of coverages from isolated molecules to thin films.

Modelling the surface physics of adsorbed organic molecules at finite coverage allows one to study the formation of the ordered structures often seen in STM experiments (for DTA on Cu(111), e.g., the formation of rows and islands of DTA molecules was observed [5]). In particular, the formation of nanostructured layers of organic molecules coordinated by adsorbed metal atoms is an attractive area of investigation. These systems show unique structural properties, such as formation of regular arrays of cavities with tunable geometry and cavity size [4, 75, 76]. The ability to model the formation of such structures from first principles is invaluable and should provide powerful insights into these fascinating systems.

# Bibliography

[1] Antczak, G & Ehrlich, G. (2005) The beginnings of surface diffusion studies. *Surface Science* **589**, 52–66.

[2] Forrest, S. R. (1997) Ultrathin Organic Films Grown by Organic Molecular Beam Deposition and Related Techniques. *Chemical Reviews* **97**, 1793–1896.

[3] Auwärter, W, Klappenberger, F, Weber-Bargioni, A, Schiffrin, A, Strunskus, T, Wöll, C, Pennec, Y, Riemann, A, & Barth, J. V. (2007) Conformational Adaptation and Selective Adatom Capturing of Tetrapyridyl-porphyrin Molecules on a Copper (111) Surface. *Journal of the American Chemical Society* **129**, 11279–11285.

[4] Stepanow, S, Lin, N, & Barth, J. V. (2008) Modular assembly of low-dimensional coordination architectures on metal surfaces. *Journal of Physics: Condensed Matter* **20**, 184002.

[5] Kwon, K. Y, Wong, K. L, Pawin, G, Bartels, L, Stolbov, S, & Rahman, T. S. (2005) Unidirectional Adsorbate Motion on a High-Symmetry Surface: "Walking" Molecules Can Stay the Course. *Physical Review Letters* **95**, 166101.

[6] Eichberger, M, Marschall, M, Reichert, J, Weber-Bargioni, A, Auwarter, W, Wang, R. L. C, Kreuzer, H. J, Pennec, Y, Schiffrin, A, & Barth, J. V. (2008) Dimerization Boosts One-Dimensional Mobility of Conformationally Adapted Porphyrins on a Hexagonal Surface Atomic Lattice. *Nano Letters* **8**, 4608–4613.

[7] Otero, R, Hummelink, F, Sato, F, Legoas, S. B, Thostrup, P, Laegsgaard, E, Stensgaard, I, Galvao, D. S, & Besenbacher, F. (2004) Lock-and-key effect in the surface diffusion of large organic molecules probed by STM. *Nature Materials* **3**, 779–782.

[8] Ala-Nissila, T, Ferrando, R, & Ying, S. C. (2002) Collective and single particle diffusion on surfaces. *Advances in Physics* **51**, 949–1078.

[9] Payne, S. H & Kreuzer, H. J. (2008) Collective diffusion in two-dimensional systems: Exact results to establish limitations of the Reed-Ehrlich factorization. *Physical Review B* **77**, 121403.

[10] Azzouz, M, Kreuzer, H. J, & Shegelski, M. R. A. (2002) Microscopic derivation of the master and Fokker-Planck equations for surface diffusion. *Physical Review B* **66**, 125403.

[11] Payne, S. H & Kreuzer, H. J. (2007) Diffusion in a one-dimensional system with nearest and next-nearest neighbor interactions: Exact analysis based on the kinetic lattice gas model. *Physical Review B* **75**, 115403.

[12] Hänggi, P, Talkner, P, & Borkovec, M. (1990) Reaction-rate theory: fifty years after Kramers. *Reviews of Modern Physics* **62**, 251–341.

[13] Schunack, M, Linderoth, T. R, Rosei, F, Laegsgaard, E, Stensgaard, I, & Besenbacher, F. (2002) Long Jumps in the Surface Diffusion of Large Molecules. *Physical Review Letters* **88**, 156102.

[14] Zwanzig, R. (1973) Nonlinear generalized Langevin equations. *Journal of Statistical Physics* **9**, 215–220.

[15] Tsekov, R & Ruckenstein, E. (1994) Stochastic dynamics of a subsystem interacting with a solid body with application to diffusive processes in solids. *The Journal of Chemical Physics* **100**, 1450–1455.

[16] Wahnström, G. (1985) Diffusion of an adsorbed particle: Theory and numerical results. *Surface Science* **159**, 311–332.

[17] Chen, L. Y & Ying, S. C. (1999) Solution of the Langevin equation for rare event rates using a path-integral formalism. *Physical Review B* **60**, 16965–16971.

[18] Braun, O. M, Ferrando, R, & Tommei, G. E. (2003) Stimulated diffusion of an adsorbed dimer. *Physical Review E* **68**, 051101.

[19] Caratti, G, Ferrando, R, Spadacini, R, & Tommei, G. E. (1996) Noise-activated diffusion in the egg-carton potential. *Physical Review E* **54**, 4708–4721.

[20] Ferrando, R, Spadacini, R, & Tommei, G. E. (1993) Kramers problem in periodic potentials: Jump rate and jump lengths. *Physical Review E* **48**, 2437–2451.

[21] Ala-Nissila, T & Ying, S. C. (1990) Microscopic theory of surface diffusion. *Physical Review B* **42**, 10264–10274.

[22] Chen, L. Y & Ying, S. C. (1994) Dynamics of adatoms on solid surfaces. *Physical Review B* **49**, 13838–13847.

[23] van Kampen, N. G. (2007) *Stochastic Processes in Physics and Chemistry.* (North Holland), 3 edition.

[24] Risken, H. (1989) *The Fokker-Planck Equation.* (Springer-Verlag).

[25] Gomer, R. (1990) Diffusion of adsorbates on metal surfaces. *Reports on Progress in Physics* **53**, 917–1002.

[26] Jacobs, K. (2010) *Stochastic Processes for Physicists.* (Cambridge University Press).

[27] Grote, R. F & Hynes, J. T. (1980) The stable states picture of chemical reactions. II. Rate constants for condensed and gas phase reaction models. *The Journal of Chemical Physics* **73**, 2715–2732.

[28] Mori, H. (1965) Transport, Collective Motion, and Brownian Motion. *Progress of Theoretical Physics* **33**, 423–455.

[29] Ala-Nissila, T & Ying, S. (1992) Theory of classical surface diffusion. *Progress in Surface Science* **39**, 227–323.

[30] Graham, W. R & Ehrlich, G. (1973) Surface Self-Diffusion of Atoms and Atom Pairs. *Physical Review Letters* **31**, 1407–1408.

[31] Stolt, K, Graham, W. R, & Ehrlich, G. (1976) Surface diffusion of individual atoms and dimers: Re on W(211). *The Journal of Chemical Physics* **65**, 3206–3222.

[32] Kreuzer, H. J & March, N. H. (1988) Origin and information content of the compensation effect. *Theoretica Chimica Acta* **74**, 339–348.

[33] Weckesser, J, Barth, J. V, & Kern, K. (1999) Direct observation of surface diffusion of large organic molecules at metal surfaces: PVBA on Pd(110). *The Journal of Chemical Physics* **110**, 5351–5354.

[34] Chen, L. Y, Baldan, M. R, & Ying, S. C. (1996) Surface diffusion in the low-friction limit: Occurrence of long jumps. *Physical Review B* **54**, 8856–8861.

[35] Braun, O. M. (2000) Role of entropy barriers for diffusion in the periodic potential. *Physical Review E* **63**, 011102.

[36] Zwanzig, R. (1992) Dynamical disorder: Passage through a fluctuating bottleneck. *The Journal of Chemical Physics* **97**, 3587.

[37] Ruckenstein, E & Tsekov, R. (1994) Diffusion of atoms and dimers on metal surfaces. *The Journal of Chemical Physics* **100**, 7696–7699.

[38] Shea, P & Kreuzer, H. J. (2011) Langevin equation for diffusion of an adsorbed molecule. *Surface Science* **605**, 296–305.

[39] Hohenberg, P & Kohn, W. (1964) Inhomogeneous Electron Gas. *Physical Review* **136**, B864–B871.

[40] Kohn, W & Sham, L. J. (1965) Self-Consistent Equations Including Exchange and Correlation Effects. *Physical Review* **140**, A1133–A1138.

[41] Perdew, J. P, Burke, K, & Ernzerhof, M. (1996) Generalized Gradient Approximation Made Simple. *Physical Review Letters* **77**, 3865–3868.

[42] Al-Saidi, W. A, Voora, V. K, & Jordan, K. D. (2012) An Assessment of the vdW-TS Method for Extended Systems. *Journal of Chemical Theory and Computation* **8**, 1503–1513.

[43] Liu, W, Ruiz, V. G, Zhang, G.-X, Santra, B, Ren, X, Scheffler, M, & Tkatchenko, A. (2013) Structure and energetics of benzene adsorbed on transition-metal surfaces: density-functional theory with van der Waals interactions including collective substrate response. *New Journal of Physics* **15**, 053046.

[44] Carrasco, J, Liu, W, Michaelides, A, & Tkatchenko, A. (2014) Insight into the description of van der Waals forces for benzene adsorption on transition metal (111) surfaces. *The Journal of chemical physics* **140**, 084704.

[45] Toyoda, K, Hamada, I, Yanagisawa, S, & Morikawa, Y. (2011) Adsorption of Benzene on Noble Metal Surfaces Studied by Density Functional Theory with Van der Waals Correction. *Journal of Nanoscience and Nanotechnology* pp. 2836–2843.

[46] Tonigold, K & Gross, A. (2010) Adsorption of small aromatic molecules on the (111) surfaces of noble metals: A density functional theory study with semiempirical corrections for dispersion effects. *The Journal of Chemical Physics* **132**.

[47] McNellis, E. R, Meyer, J, & Reuter, K. (2009) Azobenzene at coinage metal surfaces: Role of dispersive van der Waals interactions. *Physical Review B* **80**, 205414.

[48] Li, G, Tamblyn, I, Cooper, V. R, Gao, H.-J, & Neaton, J. B. (2012) Molecular adsorption on metal surfaces with van der Waals density functionals. *Physical Review B* **85**, 121409.

[49] Mercurio, G, McNellis, E. R, Martin, I, Hagen, S, Leyssner, F, Soubatch, S, Meyer, J, Wolf, M, Tegeder, P, Tautz, F. S, & Reuter, K. (2010) Structure and Energetics of Azobenzene on Ag(111): Benchmarking Semiempirical Dispersion Correction Approaches. *Physical Review Letters* **104**.

[50] Csonka, G, Perdew, J, Ruzsinszky, A, Philipsen, P, Lebègue, S, Paier, J, Vydrov, O, & Ángyán, J. (2009) Assessing the performance of recent density functionals for bulk solids. *Physical Review B* **79**, 155107.

[51] Dion, M, Rydberg, H, Schröder, E, Langreth, D. C, & Lundqvist, B. I. (2004) Van der Waals Density Functional for General Geometries. *Physical Review Letters* **92**, 246401.

[52] Lee, K, Murray, E. D, Kong, L, Lundqvist, B. I, & Langreth, D. C. (2010) Higher-accuracy van der Waals density functional. *Physical Review B* **82**, 081101.

[53] Klimeš, J, Bowler, D. R, & Michaelides, A. (2010) Chemical accuracy for the van der Waals density functional. *Journal of physics. Condensed matter : an Institute of Physics journal* **22**, 022201.

[54] Jurecka, P, Sponer, J, Cerný, J, & Hobza, P. (2006) Benchmark database of accurate (MP2 and CCSD(T) complete basis set limit) interaction energies of small model complexes, DNA base pairs, and amino acid pairs. *Physical chemistry chemical physics : PCCP* **8**, 1985–93.

[55] Klimeš, J, Bowler, D. R, & Michaelides, A. (2011) Van der Waals density functionals applied to solids. *Physical Review B* **83**, 195131.

[56] Grimme, S. (2006) Semiempirical GGA-type density functional constructed with a long-range dispersion correction. *Journal of computational chemistry* **27**, 1787–99.

[57] Tkatchenko, A & Scheffler, M. (2009) Accurate Molecular Van Der Waals Interactions from Ground-State Electron Density and Free-Atom Reference Data. *Physical Review Letters* **102**, 073005.

[58] Ruiz, V. G, Liu, W, Zojer, E, Scheffler, M, & Tkatchenko, A. (2012) Density-Functional Theory with Screened van der Waals Interactions for the Modeling of Hybrid Inorganic-Organic Systems. *Physical Review Letters* **108**, 146103.

[59] Wong, K. L, Lin, X, Kwon, K.-Y, Pawin, G, Rao, B. V, Liu, A, Bartels, L, Stolbov, S, & Rahman, T. S. (2004) Halogen-substituted thiophenol molecules on Cu(111). *Langmuir : the ACS journal of surfaces and colloids* **20**, 10928–34.

[60] Alfonso, D. R. (2008) First-principles studies of H2S adsorption and dissociation on metal surfaces. *Surface Science* **602**, 2758–2768.

[61] Wan, L.-J & Itaya, K. (1997) In Situ Scanning Tunneling Microscopy of Benzene, Naphthalene, and Anthracene Adsorbed on Cu(111) in Solution. *Langmuir* **13**, 7173–7179.

[62] Thonhauser, T, Cooper, V. R, Li, S, Puzder, A, Hyldgaard, P, & Langreth, D. C. (2007) Van der Waals density functional: Self-consistent potential and the nature of the van der Waals bond. *Physical Review B* **76**, 125112.

[63] Methfessel, M & Paxton, A. (1989) High-precision sampling for Brillouin-zone integration in metals. *Physical Review B* **40**, 3616–3621.

[64] Dierchx, P. (1995) *Curve and Surface Fitting with Splines.* (Oxford University Press).

[65] Fritsch, F. N & Carlson, R. E. (1980) Monotone Piecewise Cubic Interpolation. *SIAM Journal on Numerical Analysis* **17**, 238–246.

[66] Hellsing, B & Persson, M. (1984) Electronic Damping of Atomic and Molecular Vibrations at Metal Surfaces. *Physica Scripta* **29**, 360–371.

[67] Head-Gordon, M & Tully, J. C. (1995) Molecular dynamics with electronic frictions. *The Journal of Chemical Physics* **103**, 10137.

[68] Trail, J, Graham, M, & Bird, D. (2001) Electronic damping of molecular motion at metal surfaces. *Computer Physics Communications* **137**, 163–173.

[69] Kindt, J. T, Tully, J. C, Head-Gordon, M, & Gomez, M. A. (1998) Electron-hole pair contributions to scattering, sticking, and surface diffusion: CO on Cu(100). *The Journal of Chemical Physics* **109**, 3629.

[70] Dove, M. T. (2005) *Introduction to Lattice Dynamics.* (Cambridge University Press).

[71] Wahnström, G. (1985) Continuum elastic treatment of surface lattice dynamics. *Surface Science* **164**, 437–448.

[72] Kreuzer, H. J & Gortel, Z. W. (1986) *Physisorption Kinetics.* (Springer Verlag).

[73] Kramers, H. A. (1940) Brownian motion in a field of force and the diffusion model of chemical reactions. *Physica* **7**, 284–304.

[74] Kästner, J. (2011) Umbrella sampling. *Wiley Interdisciplinary Reviews: Computational Molecular Science* **1**, 932–942.

[75] Schlickum, U, Decker, R, Klappenberger, F, Zoppellaro, G, Klyatskaya, S, Ruben, M, Silanes, I, Arnau, A, Kern, K, Brune, H, & Barth, J. V. (2007) MetalOrganic Honeycomb Nanomeshes with Tunable Cavity Size. *Nano Letters* **7**, 3813–3817.

[76] Langner, A, Tait, S. L, Lin, N, Rajadurai, C, Ruben, M, & Kern, K. (2007) Self-recognition and self-selection in multicomponent supramolecular coordination networks on surfaces. *Proceedings of the National Academy of Sciences* **104**, 17927–17930.

[77] Gradshteyn, I. S & Ryzhik, I. M. (1994) *Table of Integrals, Series, and Products, Fifth Edition.* (Academic Press), 5th edition.

# Appendix A

# Matrix Elements of FP Operator for Dimer

In this appendix we give the matrix elements of the FP operator for a dimer in 1D, required for the MCF solution of the FPE used in Chapter 3. For the multidimensional FPE of the type Eq. (2.33) describing the dimer in 1D, we use scaled variables analogous to those introduced in section 2.3.1,

$$\bar{r}_i = \frac{2\pi}{a} r_i \quad \bar{t} = \frac{2\pi}{a}\sqrt{\frac{kT}{m_0}}t \quad \bar{v}_i = \sqrt{\frac{m_i}{kT}}v_i \quad \bar{\gamma}_{ij} = \frac{a}{2\pi}\sqrt{\frac{m_0}{m_i m_j kT}} \quad \bar{F}_i = \frac{a}{2\pi kT}F_i, \tag{A.1}$$

where $m_0$ is some reference mass. We also apply a transformation of the type shown in Eq. (2.58), resulting in the transformed FP operator

$$L' = -(b_i D_i + b_i^\dagger \hat{D}_i + b_i^\dagger \gamma_{ij} b_j), \tag{A.2}$$

where summation over the repeated indices is implied. The operators $b_i, b_i^\dagger$ are the creation and annihilation operators for the Hermite functions of each velocity variable $v_i$, satisfying the relationships shown in Eq. (2.61), and the operators $D_i, \hat{D}_i$ are

$$D_i = \frac{1}{\sqrt{m_i/m_0}}\left(\frac{\partial}{\partial r_i} + \frac{1}{2}F_i(\vec{r})\right) \qquad \hat{D}_i = \frac{1}{\sqrt{m_i/m_0}}\left(\frac{\partial}{\partial r_i} - \frac{1}{2}F_i(\vec{r})\right). \tag{A.3}$$

The matrix elements of the FP operator $L'$ have a form analogous to that shown in Eq. (2.65) for the 1D case. For the dimer in 1D described by the two coordintes $r$ and $s$, we have

$$[b_r D_r]_{\vec{m}\vec{\mu},\vec{n}\vec{\nu}} = \sqrt{\nu_r}\delta_{\mu_r,\nu_r-1}\delta_{\mu_s,\nu_s}D_{\vec{m}\vec{n}} \tag{A.4}$$

$$[b_r^\dagger \hat{D}_r]_{\vec{m}\vec{\mu},\vec{n}\vec{\nu}} = \sqrt{\nu_r+1}\delta_{\mu_r,\nu_r+1}\delta_{\mu_s,\nu_s}\hat{D}_{\vec{m}\vec{n}} \tag{A.5}$$

$$[\gamma b_r^\dagger b_r]_{\vec{m}\vec{\mu},\vec{n}\vec{\nu}} = \mu_r\delta_{\mu_r,\nu_r}\delta_{\mu_s,\nu_s}\gamma_{\vec{m},\vec{n}}, \tag{A.6}$$

with similar expressions for the $s$-terms. Expressions for the matrix elements of the $D_i$ and $\hat{D}_i$ operators are given below.

## A.1 Dimer in One Dimension

For the dimer studied in Chapter 3, consisting of two identical atoms of mass $m$ and of equilibrium length $\ell$, the potential energy is

$$V(r,s) = V_b\cos(r)\cos((s+\ell)/2) + \frac{1}{2}ks^2, \tag{A.7}$$

in terms of the centre of mass and relative coordinates $r$ and $s$, as defined in Chapter 3. The components of the corresponding force are

$$\begin{aligned} F_r(r,s) &= -\frac{\partial V}{\partial r} = V_b\sin(r)\cos((s+\ell)/2) \\ F_s(r,s) &= -\frac{\partial V}{\partial s} = V_b/2\cos(r)\sin((s+\ell)/2) - ks. \end{aligned} \tag{A.8}$$

For the basis functions we choose a Fourier series in the $r$ coordinate, and Hermite functions in the $s$ coordinate,

$$\phi_{m_s}(s) = \sqrt{\frac{\sqrt{k}n!}{2^n\sqrt{2\pi}}}H_{m_s}\left(\sqrt{\frac{k}{2}}s\right)e^{-ks^2/4}. \tag{A.9}$$

The creation and annihilation operators for the $\phi_{m_s}$ functions are then

$$c = \frac{1}{\sqrt{k}}\frac{\partial}{\partial s} + \frac{1}{2}\sqrt{k}s \qquad\qquad c^\dagger = -\frac{1}{\sqrt{k}}\frac{\partial}{\partial s} + \frac{1}{2}\sqrt{k}s, \tag{A.10}$$

which can be rearranged to obtain expressions for $s$ and $\partial/\partial s$,

$$s = (c+c^\dagger)/\sqrt{k} \qquad\qquad \frac{\partial}{\partial s} = (c-c^\dagger)\frac{\sqrt{k}}{2} \tag{A.11}$$

The matrices $D_r, D_s, \hat{D}_r, \hat{D}_s$ can then be evaluated, e.g.

$$[D_r]_{\vec{m},\vec{n}} = \frac{1}{2\pi}\int_0^{2\pi}dr\int_{-\infty}^{\infty}dse^{-im_r r}\phi_{m_s}(s)De^{in_r r}\phi_{n_s}(s). \tag{A.12}$$

Making use of Eq. (A.11), the elements of the derivatives are

$$[\frac{\partial}{\partial r}]_{\vec{m},\vec{n}} = in_r\delta_{m_r,n_r}\delta_{m_s,n_s} \tag{A.13}$$

$$[\frac{\partial}{\partial s}]_{\vec{m},\vec{n}} = \delta_{m_r,n_r}\frac{\sqrt{k}}{2}(\sqrt{n_s}\delta_{m_s,n_s-1} - \sqrt{n_s+1}\delta_{m_s,n_s+1}), \tag{A.14}$$

and the elements of the forces are

$$\begin{aligned}
[F_r]_{\vec{m},\vec{n}} &= -\frac{V_b}{2} f_{n_s-m_s}(\ell/2)\left(i\delta_{m_r,n_r+1}+\delta_{m_r,n_r-1}\right)e^{-1/(8k)}\sqrt{\frac{m_s!}{n_s!}}\left(\frac{i}{2\sqrt{k}}\right)^{n_s-m_s} L_{m_s}^{n_s-m_s}\left[\frac{1}{4k}\right] \\
[F_s]_{\vec{m},\vec{n}} &= -\frac{V_b}{4} f_{n_s-m_s+1}(\ell/2)\left(i\delta_{m_r,n_r+1}-\delta_{m_r,n_r-1}\right)e^{1/(8k)}\sqrt{\frac{m_s!}{n_s!}}\left(\frac{i}{2\sqrt{k}}\right)^{n_s-m_s} L_{m_s}^{n_s-m_s}\left[\frac{1}{4k}\right] \\
&\quad - \sqrt{k}\left(\sqrt{n_s}\delta_{m_s,n_s-1}+\sqrt{n_s+1}\delta_{m_s,n_s+1}\right)\delta_{m_r,n_r} \\
&\quad \text{for} \quad n_s > m_s, \quad [F_r]_{m_r m_s,n_r n_s} = [F_r]_{m_r n_s,n_r m_s}, \quad [F_s]_{m_r m_s,n_r n_s} = [F_s]_{m_r n_s,n_r m_s},
\end{aligned} \tag{A.15}$$

where the $L_n^{\alpha}(x)$ are the associated Laguerre polynomials [77], and

$$f_{n_s-m_s}(\ell/2) = \begin{cases} \cos(\ell/2) & n_s-m_s \quad \text{even} \\ i\sin(\ell/2) & n_s-m_s \quad \text{odd} \end{cases}. \tag{A.16}$$

For the coefficients of the factor $P = e^{-V(r,s)/2}$, one of the integrals can be evaluated analytically, giving

$$[P]_{\vec{m}} = \int_{-\infty}^{\infty} ds(-1)^{m_r} I_{m_r}\left(\frac{V_b}{2}\cos((s+\ell)/2)\right)e^{-ks^2/4}\phi_{m_s}(s), \tag{A.17}$$

where $I_m(x)$ is the modified Bessel function of the first kind [77].

## A.2 Dimer in One Dimension, Harmonic Approximation

In the harmonic approximation, the potential and forces become

$$\begin{aligned}
V(r,s) &= V_b\cos(r)\cos(\ell/2) - \frac{\phi^2(r)}{2k} + \frac{1}{2}k\left(s+\frac{\phi(r)}{k}\right)^2 \\
&= V_b\cos(r)\cos(\ell/2) - \frac{V_b^2}{16k}\cos(2r)\sin^2(\ell/2) + \frac{1}{2}k\left(s+\frac{\phi(r)}{k}\right)^2 - \frac{V_b^2}{16k}\sin^2(\ell/2), \\
\phi(r) &= -\frac{V_b}{2}\cos(r)\sin(\ell/2), \\
F_r &= V_b\sin(r)\cos(\ell/2) - \frac{V_b^2}{8k}\sin(2r)\sin^2(\ell/2) - \frac{V_b}{2}\sin(r)\sin(\ell/2)\left(s+\frac{\phi(r)}{k}\right) \\
F_s &= -k\left(s+\frac{\phi(r)}{k}\right)
\end{aligned} \tag{A.18}$$

For the basis functions we again take Fourier components for the $r$ coordinate, and Hermite functions for the $s$ coordinate, but now use the shifted Hermite functions

$\phi_{m_s}(s+\phi(r)/k)$. Similar relations to those shown in Eq. (A.11) are then satisfied, but with $s$ replaced by $s+\phi(r)/k$. Using this shifted version greatly improves the convergence at small $k$.

The components of the derivatives are

$$\begin{aligned}
[\frac{\partial}{\partial r}]_{\vec{m},\vec{n}} &= in_r\delta_{m_r,n_n}\delta_{m_s,n_s} + \frac{1}{2\sqrt{k}}[\phi']_{\vec{m}}(\sqrt{n_s}\delta_{m_s,n_s-1} - \sqrt{n_s+1}\delta_{m_s,n_s+1}) \\
[\frac{\partial}{\partial s}]_{\vec{m},\vec{n}} &= \frac{\sqrt{k}}{2}\delta_{m_r,n_r}(\sqrt{n_s}\delta_{m_s,n_s-1} - \sqrt{n_s+1}\delta_{m_s,n_s+1}) \\
[\phi']_{\vec{m}} &= \frac{V_b}{2}\sin(\ell/2)\left(\frac{\delta_{m_r,n_r+1}}{2i} - \frac{\delta_{m_r,n_r-1}}{2i}\right),
\end{aligned} \tag{A.19}$$

and the components of the force are

$$\begin{aligned}
[F_r]_{\vec{m},\vec{n}} = {} & \frac{V_b\cos(\ell/2)}{2i}(\delta_{m_r,n_r+1} - \delta_{m_r,n_r-1})\delta_{m_s,n_s} - \frac{V_b^2}{16ki}(\delta_{m_r,n_r+2} - \delta_{m_r,n_r-2})\delta_{m_s,n_s} \\
& - \frac{V_b}{4i}\sin(\ell/2)(\delta_{m_r,n_r+1} - \delta_{m_r,n_r-1})(\sqrt{\nu}\delta_{m_s,n_s-1} + \sqrt{n_s+1}\delta_{m_s,n_s+1})/\sqrt{k} \\
[F_s]_{\vec{m},\vec{n}} = {} & -\sqrt{k}\delta_{m_r,n_r}(\sqrt{n_s}\delta_{m_s,n_s-1} + \sqrt{n_s+1}\delta_{m_s,n_s+1}).
\end{aligned} \tag{A.20}$$

For the elements of $P$, the $s$-integral can be evaluated to give

$$\begin{aligned}
[P]_{\vec{m}} = \frac{1}{2\pi}\int_0^{2\pi} & dr \exp\left(-\frac{V_b}{2}\cos(r)\cos(\ell/2) + \frac{V_b^2}{32k}\cos(2r)\sin^2(\ell/2) + \frac{V_b^2}{32k}\sin^2(\ell/2)\right) \\
& \times e^{-m_r r}\left(\frac{2\pi}{k}\right)^{1/4}\delta_{m_s,0},
\end{aligned} \tag{A.21}$$

and similarly for the normalization factor $N$,

$$N = \int_0^{2\pi} dr \exp\left(-V_b\cos(r)\cos(\ell/2) + \frac{V_b^2}{16k}\cos(2r)\sin^2(\ell/2) + \frac{V_b^2}{16k}\sin^2(\ell/2)\right)\sqrt{\frac{2\pi}{k}}. \tag{A.22}$$

## A.3 Dimer in One Dimension, Markov Approximation

In the Markov approximation, the potential is that of the harmonic approximation evaluated with $s$ at it's minimum energy value, $s=-\phi(r)/k$,

$$V(r) = V_b\cos(r)\cos(\ell/2) - \frac{1}{2}\frac{\phi(r)^2}{k(r)} \tag{A.23}$$

The matrix elements for $D$ and $\hat{D}$ can then be evaluated from those in the previous section. In the Markov approximation, the Fourier components of the position-dependent friction $\gamma_{\text{eff}} = \gamma_{rr} + \gamma_{\text{vib}}(r)$ are also required. For the 1D dimer, the effective friction is

$$\gamma_{\text{eff}}(r) = \gamma_{rr} + \gamma_{ss}\phi^2(r)/k^2 = \gamma_{rr} + \frac{\gamma_{ss}V_b^2}{4k^2}\cos^2(r)\sin^2(\ell/2), \tag{A.24}$$

with Fourier components

$$[\gamma_{\text{eff}}]_{m,n} = \gamma_{rr}\delta_{m,n} + \frac{\gamma_{ss}V_b^2}{16k^2}\sin^2(\ell/2)(\delta_{m,n+2} + \delta_{m,n-2} + 2\delta_{m,n}). \tag{A.25}$$

# Appendix B

# Memory Function for General Damping

In this appendix we show how to derive the GLE found in section 3.1 for a molecule described by a center of mass coordinate $\vec{r}$ and $N$ internal coordinates. For simplicity of notation we consider here unidirectional diffusion, so that the center of mass coordinate is a scalar $r$; repeating the derivation for a molecule that diffuses in more than one dimension introduces no additional complications.

First the potential is expanded to quadratic order in the internal coordinates,

$$V(r,\vec{s}) = V_0(r) + \vec{\phi}(r)\cdot\vec{s} + \frac{1}{2}\vec{s}^T\cdot\mathbf{K}\cdot\vec{s}, \tag{B.1}$$

where $\vec{s}$ is a column vector of the $N$ internal coordinates (with corresponding row vector $\vec{s}^T$), and $\mathbf{K}$ is a matrix of force constants. The equations of motion for the internal coordinates can be written

$$\mathbf{M}\cdot\ddot{\vec{s}} + \boldsymbol{\gamma}\cdot\dot{\vec{s}} + \mathbf{K}\cdot\vec{s} = -\vec{\phi}(r) - \vec{\gamma}_{rs}\dot{r} + \vec{f}_s(t), \tag{B.2}$$

where $\mathbf{M}$, and $\boldsymbol{\gamma}$ are matrices of the masses and damping coefficients, respectively. The homogeneous solution is found by assuming the time dependence $\vec{s}(t) = \vec{x}e^{\lambda t}$, where $\vec{x}$ is a constant vector, resulting in the generalized eigenvalue problem

$$\lambda^2\mathbf{M}\cdot\vec{x} + \lambda\boldsymbol{\gamma}\cdot\vec{x} + \mathbf{K}\cdot\vec{x} = 0. \tag{B.3}$$

In the absence of damping forces, a set of eigenvectors $\vec{x}_n$ and eigenvalues $\omega_n^2$ can be found that diagonalize $\mathbf{M}$ and $\mathbf{K}$, and the equations of motion for the normal modes decouple. However the eigenvectors $\vec{x}_n$ will in general not diagonalize the matrix $\boldsymbol{\gamma}$ of damping coefficients, and the normal modes will be coupled as shown in Eq. (3.24).

To find normal mode solutions, one rewrites the equations of motion in terms of the $2N$-dimensional vector $\vec{z}^T = (\vec{s}^T, \dot{\vec{s}}^T)$,

$$\mathbf{M}_z\cdot\dot{\vec{z}} + \mathbf{K}_z\cdot\vec{z} = \vec{F}, \tag{B.4}$$

where the matrices $\mathbf{M}_z$ and $\mathbf{K}_z$ and the force vector $\vec{F}$ are defined as

$$\mathbf{M}_z = \begin{pmatrix} \boldsymbol{\gamma} & \mathbf{M} \\ \mathbf{M} & 0 \end{pmatrix} \qquad \mathbf{K}_z = \begin{pmatrix} \mathbf{K} & 0 \\ 0 & -\mathbf{M} \end{pmatrix} \qquad \vec{F} = \begin{pmatrix} -\vec{\phi} - \vec{\gamma}_{rs}\dot{r} + \vec{f}_s \\ 0 \end{pmatrix}. \tag{B.5}$$

The eigenvalue problem can then be written as

$$\lambda \mathbf{M}_z \cdot \vec{z} + \mathbf{K}_z \cdot \vec{z} = 0, \tag{B.6}$$

and the eigenvectors $\vec{z}_n$ and eigenvalues $\lambda_n$ can be found such that

$$\vec{z}_m^T \cdot \mathbf{M}_z \cdot \vec{z}_n = \delta_{mn} \qquad\qquad \vec{z}_m^T \cdot \mathbf{K}_z \cdot \vec{z}_n = -\lambda_m \delta_{mn}. \tag{B.7}$$

The eigenvectors must also have the form $\vec{z}_n^T = (\vec{x}_n^T, \lambda_n \vec{x}_n^T)$, where $\vec{x}_n$ are the length $N$ vectors that solve the eigenvalue problem (B.3). The solution is then written as $\vec{z}(t) = \sum_n q_n(t)\vec{z}_n$, and Eqs.(B.4) and (B.7) can be used to find the equations of motion for $q_n(t)$:

$$\dot{q}_n + \lambda_n q_n = -\Phi_n - \Gamma_n \dot{r} + f_n, \tag{B.8}$$

where $\Phi_n = \vec{z}_n^T \cdot \vec{\phi}$, $\Gamma_n = \vec{z}_n^T \cdot \vec{\gamma}_{rs}$ and $f_n = \vec{z}_n^T \cdot \vec{f}_s$. The solutions for $q_n(t)$ are then

$$q_n(t) = q_n(0)e^{\lambda_n t} + \int_0^t dt' e^{\lambda_n (t-t')}[-\Phi_n(r(t')) - \Gamma_n \dot{r}(t') + f_n(t')]. \tag{B.9}$$

The initial conditions $q_n(0)$ are related to the initial conditions for $\vec{s}, \dot{\vec{s}}$ by $q_n(0) = \vec{z}_n \cdot \mathbf{M}_z \cdot \vec{z}(0)$.

With the formal solution for the internal motion of the molecule $\vec{s}(t), \dot{\vec{s}}(t)$ in hand, the same procedure as in section 3.1 can be followed to obtain a GLE for the center of mass motion. The solution is substituted into the equation of motion for $r$,

$$\begin{aligned} M\ddot{r} &= -V_0' - \gamma_{rr}\dot{r} - \vec{\gamma}_{rs}^T \cdot \dot{\vec{s}} - \vec{\phi}'^T \cdot \vec{s} + f_r(t) && \text{(B.10)} \\ &= -V_0' - \gamma_{rr}\dot{r} - \sum_n (\Phi_n' + \lambda_n \Gamma_n) q_n(t) + f_r(t), && \text{(B.11)} \end{aligned}$$

resulting in a GLE of the form in Eq. (3.11), with

$$U(r) = V_0(r) - \frac{1}{2}\vec{\phi}^T(r) \cdot \mathbf{K}^{-1} \cdot \vec{\phi}(r) \tag{B.12}$$

$$\Gamma_{\text{vib}}[r(t), r(t'), t-t'] = \sum_n (\Phi'_n(r(t)) + \lambda_n \Gamma_n)(\Phi'_n(r(t')) + \lambda_n \Gamma_n) \frac{e^{\lambda_n (t-t')}}{-\lambda_n} \tag{B.13}$$

$$\begin{aligned} F_{\text{vib}}(t) = & -\sum_n (\Phi'_n(r(t)) + \lambda_n \Gamma_n) \left( q_n(0) - \frac{\Phi_n(0)}{\lambda_n} \right) e^{\lambda_n t} \\ & - \sum_n (\Phi'_n(r(t)) + \lambda_n \Gamma_n) \int_0^t dt' e^{\lambda_n (t-t')} F_n(t'), \end{aligned} \tag{B.14}$$

where the stochastic force $F(t)$ has the statistical properties shown in Eq. (3.18). The averages are calculated using the equilibrium probability distribution for the initial conditions $\vec{s}(0), \dot{\vec{s}}(0)$,

$$\rho(\vec{s}, \dot{\vec{s}}) = \frac{e^{-\frac{1}{2}\dot{\vec{s}}^T \cdot \mathbf{M} \cdot \dot{\vec{s}}/kT - \frac{1}{2}(\vec{s}^T + \vec{\phi}^T \cdot \mathbf{K}^{-1}) \cdot \mathbf{K} \cdot (\vec{s} + \mathbf{K}^{-1} \cdot \vec{\phi})/kT}}{2\pi \sqrt{|\mathbf{M}^{-1}||\mathbf{K}^{-1}|}}, \tag{B.15}$$

giving the averages

$$\begin{aligned} & \left\langle \vec{s}(0) + \mathbf{K}^{-1} \cdot \vec{\phi}(0) \right\rangle = \left\langle \dot{\vec{s}}(0) \right\rangle = 0 \\ & \left\langle (\vec{s}(0) + \mathbf{K}^{-1} \cdot \vec{\phi}(0))(\vec{s}^T + \vec{\phi}^T(0) \cdot \mathbf{K}^{-1}) \right\rangle = kT\mathbf{K}^{-1} \\ & \left\langle \dot{\vec{s}}(0) \dot{\vec{s}}^T(0) \right\rangle = kT\mathbf{M}^{-1}. \end{aligned} \tag{B.16}$$

The averages of the terms in $F(t)$ can be related to the above averages by making use of the following equality

$$q_n(0) - \frac{\Phi_n(0)}{\lambda_n} = \vec{z}_n^T \cdot \mathbf{M}_z \cdot \begin{pmatrix} \vec{s}(0) + \mathbf{K}^{-1} \cdot \vec{\phi}(0) \\ \dot{s}(0) \end{pmatrix}. \tag{B.17}$$

The completeness of the eigenvectors $\vec{z}_i$ is also useful when proving Eqs. (3.18). An arbitrary matrix $A$ can be expanded in the eigenvectors as $A = \sum_{m,n} a_{mn} \vec{z}_m \vec{z}_n^T$, where the elements are given by $a_{mn} = \vec{z}_m^T \cdot \mathbf{M}_z \cdot A \cdot \mathbf{M}_z \cdot \vec{z}_n$. This property can be used to show the following relations

$$\sum_n \vec{x}_n \vec{x}_n^T = 0 \qquad \sum_n \frac{\vec{x}_n \vec{x}_n^T}{\lambda_n} = -\mathbf{K}^{-1} \qquad \sum_n \frac{\vec{x}_n \vec{x}_n^T}{\lambda_n^2} = \mathbf{K}^{-1} \cdot \boldsymbol{\gamma} \cdot \mathbf{K}^{-1}. \tag{B.18}$$

By making use of (B.17) and (B.18), along with the orthogonality relations (B.7), Eqs. (3.18) can, with some effort, be shown to be satisfied by the memory function and stochastic force.

To find the effective friction in the MA, first rewrite the memory function as

$$\Gamma_{\text{vib}} = \left(\vec{\phi}'^T(r(t)), \quad \vec{\gamma}_{rs}^T\right) \cdot \left(\sum_n \vec{z}_n^T \vec{z}_n \frac{e^{\lambda_n(t-t')}}{-\lambda_n}\right) \cdot \begin{pmatrix} \vec{\phi}'(r(t')) \\ \vec{\gamma}_{rs} \end{pmatrix}. \tag{B.19}$$

In the MA, the memory function is replaced by its time-integrated value

$$\int_0^\infty dt' \Gamma_{\text{vib}}(r, t') = \left(\vec{\phi}'^T(r(t)), \quad \vec{\gamma}_{rs}^T\right) \cdot \mathbf{Q} \cdot \begin{pmatrix} \vec{\phi}'(r(t')) \\ \vec{\gamma}_{rs} \end{pmatrix}, \tag{B.20}$$

where $\mathbf{Q} = \sum_n \vec{z}_n \vec{z}_n^T / \lambda_n^2$. Making use of Eqs. (B.18), the matrix $\mathbf{Q}$ is found to be

$$\mathbf{Q} = \begin{pmatrix} \mathbf{K}^{-1} \cdot \boldsymbol{\gamma} \cdot \mathbf{K}^{-1} & -\mathbf{K}^{-1} \\ -\mathbf{K}^{-1} & 0 \end{pmatrix}. \tag{B.21}$$

The effective friction is then

$$\gamma_{\text{eff}} = \gamma_{rr} + \sum_n \vec{\phi}'^T \cdot \mathbf{K}^{-1} \cdot \boldsymbol{\gamma} \cdot \mathbf{K}^{-1} \cdot \vec{\phi}' - 2 \sum_n \vec{\gamma}_{rs} \cdot \mathbf{K}^{-1} \cdot \vec{\phi}' \tag{B.22}$$

$$= \gamma_{rr} + \sum_{m,n} \gamma_{mn} \frac{\phi'_m}{\omega_m^2} \frac{\phi'_n}{\omega_n^2} - 2 \sum_m \gamma_{rm} \frac{\phi'_m}{\omega_m^2}. \tag{B.23}$$

Note that the above expression depends only on the vibration frequencies $\omega_n$ in the undamped system, found by diagonalizing the matrix of force constants $\mathbf{K}$, so that in the MA one avoids the need to explicitly solve the damped normal modes problem.